CONTROL AND ELIMINATION OF CRACKING IN $Al_{0.20}Ga_{0.80}N$ USING $Al_xGa_{1-x}N$ INTERLAYERS AND APPLICATION TOWARD A NEAR ULTRAVIOLET VERTICAL CAVITY SURFACE EMITTING LASER

By

KAREN ELIZABETH WALDRIP

A DISSERTATION PRESENTED TO THE GRADUATE SCHOOL
OF THE UNIVERSITY OF FLORIDA IN PARTIAL FULFILLMENT
OF THE REQUIREMENTS FOR THE DEGREE OF
DOCTOR OF PHILOSOPHY

UNIVERSITY OF FLORIDA

2001

Copyright 2001

by

Karen Elizabeth Waldrip

ACKNOWLEDGMENTS

The author would like to acknowledge and thank the many people who helped make this dissertation possible. First of all, deep and heartfelt gratitude go to my parents, Barbara and Gordon Ball, and Lee and Linda Waldrip, and to my sisters Amy Wharton and Susan Waldrip, and to Wish Krishnamoorthy. As they well know, without their support throughout, things may have gone very differently. A special thank you to the chairman of my supervisory committee, Cammy Abernathy, without whose support this would have all been impossible, or at least much longer in the making and not at the University of Florida. I would also like to thank my committee members, Professors Stan Bates, Rajiv Singh, Steve Pearton, and Fan Ren. As for the group at Sandia National Laboratories, I am forever especially grateful to Jung Han, Steve Lee, Jerry Floro, and David Follstaedt for their guidance and patience. Allen West has been particularly helpful with the finish-line tasks required for putting together a dissertation. Special thanks also goes to Tom Kerley for interesting technical and non-technical discussions, and to Billie Kazmierczak for all of her help. I appreciate my manager Bob Biefeld, whose financial and moral support made my graduate life at Sandia much, much easier.

As the academic aspect of my graduate school experience was but a minor--yet pleasant--distraction from the process of completing a doctoral program at the University of Florida, this list would be glaringly incomplete were it not to include the people that gave me the courage to see it through. A citation in my acknowledgements section is clearly only a meager representation of my unspeakable gratitude, and it applies to those already mentioned as well. Mrs. Maggie Gerard is solidly in my heart forever, as are Jeanne Macdonald, Missy Norman, Brent Gila, Billie Abrams, Ludie Harmon, and I must give a double-mention to Wish Krishnamoorthy and Barbara Ball. It is my greatest aspiration that I might one day be half the angel to others that these people have all been to me.

TABLE OF CONTENTS

page

ACKNOWLEDGEMENTS iii

ABSTRACT vii

CHAPTERS

1 INTRODUCTION 1

Background and Motivation 1
Suitability of Nitrides for Light Emitters 4
Statement of Problem 5
Gallium Nitride Growth 7
Growth of Aluminum Gallium Nitride 9

2 EXPERIMENTAL PROCEDURE 20

Growth Technique: Metalorganic Chemical Vapor Deposition 20
In situ Stress Monitor: MOSS 22
High Resolution X-ray Diffraction Measurements 25
Atomic Force Microscopy 27
Transmission Electron Microscopy 27
Rutherford Backscattering Spectroscopy 27
Photoluminescence 28
Secondary Ion Mass Spectroscopy 28

3 ULTRA-RAPID CATASTROPHIC RELAXATION PROCESSES IN AlGaN/GaN HETEROSTRUCTURES 33

Introduction 33
Mechanics of the AlGaN/GaN Heterosystem 34
Other Investigations 34
Experimental Details 36
Results 37

4 CONTROL AND ELIMINATION OF CRACKING IN $Al_{0.20}Ga_{0.80}N$ USING $Al_xGa_{1-x}N$ INTERLAYERS 52

Introduction 52
Low-Temperature Deposited Ternary Alloy Interlayers 54
Investigation of the Effect of Growth Temperature of AlN Interlayers on the Defect Structure of $Al_{0.20}Ga_{0.80}N$ Overlayers 59
Investigation of AlN Interlayer Thickness on Defect Structure of $Al_{0.20}Ga_{0.80}N$ Overlayers 63
Investigation of AlN V/III Ratio Variation on $Al_{0.20}Ga_{0.80}N$ Overlayers 66
Discussion and Summary 68

5 INTERLAYER RELAXATION MECHANISMS 89

Morphology of LT-$Al_xGa_{1-x}N$ interlayers 90
In situ Observation of HT-AlN Strain State 91
Possible Relaxation Mechanisms and Experimental Approach 93
HRXRD Investigation of AlN Strain State and Incorporation of Gallium 95
Morphological Evolution of HT-AlN with Thickness 99
Effect of V/III Ratio on the Growth of AlN 101
Discussion 102
Summary 104

6 DEVICES USING AlN INTERLAYERS 132

Introduction 132
MOVPE Growth of Highly Reflective Near UV Distributed Bragg Reflectors 133
MOVPE Growth and Processing of a Room-Temperature, Optically Pumped Ultraviolet VCSEL 139
A Vertical Cavity Violet Light Emitting Diode Incorporating an AlGaN Distributed Bragg Mirror and a Tunnel Junction 143

7 SUMMARY AND FUTURE WORK 167

LIST OF REFERENCES 171

BIOGRAPHICAL SKETCH 175

Abstract of Dissertation Presented to the Graduate School
of the University of Florida in Partial Fulfillment of the
Requirements for the Degree of Doctor of Philosophy

CONTROL AND ELIMINATION OF CRACKING IN $Al_{0.20}Ga_{0.80}N$ USING $Al_xGa_{1-x}N$ INTERLAYERS AND APPLICATION TOWARD A NEAR ULTRAVIOLET VERTICAL CAVITY SURFACE EMITTING LASER

By

Karen Elizabeth Waldrip

December 2001

Chairman: Professor C. R. Abernathy
Major Department: Materials Science and Engineering

Thin film heterostructures based on aluminum gallium nitride and gallium nitride are of particular interest for applications such as ultraviolet light emitters and detectors. Due to the elastic mismatch strain between the materials, the AlGaN films tend to crack at thicknesses and aluminum compositions that are useful for device fabrication (e.g., 0.1 µm at 10% AlN mole fraction), and cracking has been shown to be deleterious to device performance. In this work, a method has been developed to control and eliminate cracking in 0.9-µm thick $Al_{0.20}Ga_{0.80}N$ films grown on GaN by inserting a thin layer of $Al_xGa_{1-x}N$ between the $Al_{0.20}Ga_{0.80}N$ and GaN films grown by metalorganic chemical vapor deposition. The strain state of the thin interlayers is determined through a combination of *in situ* and *ex situ* characterization techniques. It is shown that the interlayer partially relaxes through the nucleation and glide of misfit dislocations to the interlayer/GaN interface, and that although the edge dislocation content in AlGaN overlayers increases by a factor of 5-10, screw dislocations from GaN underlayers are filtered by the interlayer. The number of excess threading dislocations present in AlGaN overlayers can be manipulated by controlling the amount of relaxation of the AlGaN interlayers, which can in turn be controlled by the morphology of the interlayer. It has been found that the morphology of the interlayer is affected by a combination of the strain and the aluminum surface mobility during growth, which can be controlled by adjusting growth parameters such as interlayer composition, growth temperature, interlayer thickness, and V/III ratio. These parameters are explored and guidelines for choosing an interlayer composition, thickness, and morphology are outlined based on the chosen end application for the AlGaN overlayer. Finally, the interlayer technique is applied towards the development of the world's first (at time of announcement) room temperature, quasi-continuous wave optically pumped near ultraviolet vertical cavity surface emitting laser operating at 384 nm. This device employs a crack-free epitaxially grown mirror that consists of 120 pairs of $Al_{0.20}Ga_{0.80}N$/GaN and is over five microns thick.

CHAPTER 1
INTRODUCTION

Background and Motivation

More efficient sources of white lighting are desired to reduce the cost of illumination and for environmental considerations (Figure 1-1). The efficiency of white lighting technology has improved from its earliest state--the use of wood-burning fires--to candles and oil-burning lamps, and eventually to electrical sources, such as the incandescent light bulb (Figure 1-2a-g). The advent of the fluorescent tube represented nearly a sevenfold improvement in efficiency of white lighting over the light bulb, thus effectively revolutionizing the lighting industry at the time of its introduction in the 1950s.

In the past ten to twenty years, sources of solid-state lighting have emerged as a possibility for more efficient white lighting, with three main approaches under consideration for development. The first consists of the use of the standard RGB (red-green-blue) combination of light emitting diodes, or LEDs, in appropriate power proportions, to produce white lighting with the desired color rendering. A second approach involves using an LED emitting in the ultraviolet region of the spectrum to pump a coating of RGB phosphors, mixed in the appropriate proportions, to achieve white lighting with the desired color rendering. The third approach, deemed potentially to be the most efficient, is the use of an ultraviolet vertical cavity surface emitting laser (VCSEL) to pump the RGB phosphors. The latter two approaches share a commonality with the fluorescent tube in that each uses a source of ultraviolet radiation to excite a coating of phosphors, which emit visible light upon relaxation.

Figure 1-3 displays the conversion efficiency vs. the wavelength of emitted light for LEDs emitting from the violet region (450 nm) to the red region of the visible spectrum (650 nm). Each LED source is graphed to show the production average for that wavelength and the best laboratory result reported. The red, orange and yellow LEDs (590-650nm) are fabricated from III-V compound semiconductors containing phosphorous as the group V element. The shorter wavelength LEDs (450-530nm) are produced from wide bandgap III-V compound semiconductors using nitrogen as the group V element. The gap in between the two materials results from the inherent inefficiency of light production from either set of materials in that region of the spectrum. Therefore, one may conclude that the RGB LED approach to efficient white lighting may encounter severe difficulty, limited by physical restrictions due to the materials properties of the compound semiconductors themselves. For this reason, we will hereby restrict our discussion to the development of the ultraviolet (UV) solid-state sources of radiation (UV LEDs and VCSELs) that are based on the III-nitrides.

Plotted at the far right of Figure 1-3, at 850 nm, is the vertical cavity surface emitting laser developed at Sandia National Laboratories with a wall-plug efficiency of over 50%. VCSELs with such efficiencies are desired in the ultraviolet region of the spectrum in order to pump phosphors for efficient white lighting. The accomplishment of this goal could affect a two- to four-fold improvement in white lighting, thus achieving the "Revolutionary" projection shown in Figure 1-1. With aggressive development of the

III-nitrides, it is predicted that this could be accomplished within the next one to two decades.

There is a significant economic and environmental motivation for the aggressive development of more efficient sources of white lighting. Figure 1-4(a) plots the world's energy consumption versus time, with the data shown as of 1998. Figure 1-4(b) shows the analogous plot for the United States alone. As expected, the world's energy consumption is increasing each year. Note the logarithmic scale. The energy consumption in the United States alone shows a similar trend. Of all the energy consumed in the world and in the United States, approximately 1/3 is consumed in the form of electricity. Of all the electricity consumed, approximately 20% is consumed for the sole purpose of illumination. The projected rise in electricity consumption is well correlated to the projected rise in illumination over the next twenty years. This is reasonable when one considers the number of new houses, office buildings, schools, shopping malls, etc. that will be built during the course of next twenty years. A two- to tenfold improvement in lighting efficiency would generate a savings of over 300TWh, or $20 billion per year in the United States alone, assuming complete market penetration. Worldwide, that amounts to over 1,000TWh, or $100 billion savings per year.

The remainder of this chapter is presented as follows. First, the properties of the III-Nitrides relative to other solid-state light emitters are explored, and it is found that structures based on AlGaN/GaN are the strong candidates for short wavelength light emission. Second, the interface between AlGaN and GaN films is examined and the problem that this research addresses is presented. Next, the growth of GaN is described and some alternatives to the approach chosen in this research are surveyed. The same is done for growth of AlGaN films, and the interlayer scheme that is central to this work is introduced. Finally, the goals of this research and the outline of the remainder of this dissertation are presented.

Suitability of Nitrides for Light Emitters

Figure 1-5 is a bandgap engineering diagram that plots the energy gap (or equivalently, wavelength) of commonly used III-V compound semiconductors versus the in-plane lattice constant (a). Some "conventional" compound semiconductors, such as the antimonides, arsenides, and phosphides reside in the lower right-hand corner of the diagram and encompass the far- to near-infrared and the longer wavelength portion of the visible spectrum. The nitrides reside in the upper left of the diagram, and span the higher energy and the smaller in-plane lattice constant region of the diagram.

The III-nitrides (consisting of alloys of gallium nitride, indium nitride, and aluminum nitride) possess a rich palette of properties that enable a broad range of important applications.[1] They are a family of wide, direct bandgap materials with high breakdown voltages. They are chemically stable, exhibit high hardnesses and high melting temperatures. Nitride device performance is often observed to be extremely tolerant of lattice defects in the material. In contrast to the conventional zincblende III-Vs, the nitrides display the wurtzite lattice structures, which results in piezoelectricity. Negative electron affinity has also been observed in the nitrides.[2,3] The sum of these attractive properties makes the nitrides ideal candidates for applications ranging from high temperature electronics, to chemical and shock sensors, to circuits requiring multi-functional materials integration, to our present interest--high efficiency lighting.

Figure 1-6 is a close-up of the bandgap engineering diagram, focusing in on just the III-nitrides. The present goal centers on developing efficient ultraviolet lighting sources; the near-UV region can be accessed through the use of low-indium containing alloys of GaN and InN. Indium gallium nitride alloys will emit from 385nm to 355nm for InN fractions of $0 \geq x \geq 0.045$. The present focus is on developing UV emitters with $\lambda \geq 380$ nm ($x_{\mathrm{InN}} \sim 0.04$).

Statement of Problem

While low indium fraction InGaN is satisfactory for constructing the active region of the emitter, problems arise when the ancillary structures of the LED or laser are considered. Good optical and electrical confinement are required for efficient light emitting devices, and the development of a VCSEL requires the use of thick structures of transparent material for mirror stacks on either side of the emitter and Fabry-Perot cavity. Based on these considerations, the fabrication of high crystalline quality alloys of aluminum nitride and gallium nitride become central to the development of efficient ultraviolet emitters. A film of hexagonal aluminum nitride grown heteroepitaxially on gallium nitride will experience 2.4% in-plane biaxial tension due to the mismatch in the lattice constants (***a***) between AlN and GaN (Figure 6). The nitrides are grown ***c***-axis oriented (0001) wurtzite on sapphire substrates. A III-nitride film undergoing in-plane biaxial tension will have zero resolved shear stress on any first-order slip planes.[4] Consequently, the film will be unable to nucleate and glide dislocations to relieve the tensile stress. Thus, according to Griffith's crack theory,[5] tensile stress energy accumulates during growth until the stress energy exceeds the energy required to form two new surfaces. The result is that bond rupture, or cracking, occurs.

The inset of Figure 1-7 is a plan view optical micrograph of a few thousand angstroms of $Al_{0.17}Ga_{0.83}N$ grown heteroepitaxially on GaN.[4] The film is densely cracked. The whole of Figure 1-7 shows an obliquely viewed cross-sectional scanning electron micrograph (SEM) close-up of one of those cracks. Cracks are observed to propagate along the $[1\underline{1}00]$ and $[11\underline{2}0]$ directions and extend down to the AlGaN/GaN interface. The cracks appear to have initiated during growth at high temperature (as opposed to during cool-down), as portions of the cracks have been overgrown. Thus, the cracks do not form as a result of the difference in thermal expansion coefficients, but rather as a result of the lattice mismatch between AlN and GaN. It should be noted that this is a very non-aggressive structure in terms of both thickness and mole fractional composition of aluminum nitride. The structure of interest is a VCSEL, a cartoon schematic of which is shown in Figure 1-8.

As their name suggests, Vertical Cavity Surface Emitting Lasers are constructed of an optical (Fabry-Perot) cavity formed in the vertical direction relative to epitaxy by spacer layers and mirrors. Epitaxial mirrors may be constructed by depositing quarter wavelength-thick pairs of materials with alternating indices of refraction. The reflectivity of the ideal mirror is determined by the contrast in index of refraction and the number of pairs[6]. For the AlGaN/GaN heterosystem, the contrast in index of refraction is low ($\Delta n \sim 0.08$ between $Al_{0.20}Ga_{0.80}N$ and GaN).[7] Thus, a high number of pairs is required to achieve the necessary reflectivity required for an ultraviolet VCSEL. The higher the AlN mole fraction of the AlGaN alloy, the higher the contrast, and thus the higher the reflectivity for identical numbers of pairs. The bulk of this work will focus on the development of the bottom epitaxial mirror stack, which can be over five microns thick.

Figure 1-9(a) shows an SEM of an LED structure consisting of 6,000 Å of $Al_{0.20}Ga_{0.80}N$ cladding layers on GaN.[8] This structure is much more densely cracked than that of Figure 1-8. Figure 1-9(b) displays the I-V characteristics of a number of identical devices grown on the same wafer. The results indicate a wide variety of I-V profiles, which limits the use of the heterostructure for high-quality devices or for manufacturable processes. Thus, the successful development of UV optoelectronics depends on the control and elimination of cracking in AlGaN/GaN heterostructures.

Since cracking occurs during growth at high temperature, the problem clearly lies with the inability of coherent AlGaN to relax the elastic strain energy via misfit dislocation formation. The objective of this work is to understand and modify the interface between the GaN and AlGaN layers to alter the strain state of the overlayer of AlGaN. The ultimate goal is to produce crack-free AlGaN layers of useful thicknesses and aluminum compositions for use in UV optoelectronics.

Gallium Nitride Growth

A major challenge in producing AlGaN/GaN heterostructures involves the availability and cost of substrates. The strong candidate substrate material will be similar to the III-nitrides in lattice constant, thermal expansion coefficient, chemical composition, be stable at the temperatures required for efficient decomposition of ammonia (i.e., around 1050°C), be commercially available and economically practical. The most notable potential substrates for III-nitrides are III-nitrides themselves, silicon carbide (SiC), silicon (Si), and sapphire (Al_2O_3). From a growth perspective, the ideal substrate would be the III-nitrides, which would allow homoepitaxial growth, thereby minimizing strain-induced defects and impurities in the films. Unfortunately, bulk growth of III-nitrides for substrate production is in the infant stages of research and thus these substrates are not commercially available at this time. Silicon carbide is another compatible substrate for III-nitrides, but the cost associated with SiC limits the experimentation that can be performed with this material. Silicon is the least expensive of these possibilities, but because it has a different lattice structure than III-nitrides, there are many crystallographic defects in the films, which adversely affect device performance. Sapphire is generally the substrate of choice despite the 16% lattice mismatch and 25% difference in thermal expansion coefficient[9] because it is commercially available in two- to four-inch wafers, is relatively inexpensive, is transparent to UV light, and is thermally stable. The large lattice mismatch between the film and the substrate induces a high number of threading dislocations (10^9-10^{10}/cm^2);[10] however, gallium nitride-based devices have been successfully fabricated on sapphire using low temperature buffer layers. A major focus in the growth of gallium nitride on sapphire is to minimize the number of these threading dislocations to improve the quality of these devices.

Although the first reports of GaN-based diodes were issued as early as 1971, significant breakthroughs in the field did not begin to occur until 1989 when Amano and Akasaki developed the two-step nucleation and growth procedure for depositing high quality GaN on sapphire.[11] Until then, gallium nitride was generally grown in a single temperature sequence on sapphire, with threading dislocations numbering $>10^{10}$ cm^{-2}. In the two-step nucleation and growth, which is now common practice, a low temperature (~550°C), thin (~25nm) buffer layer of either AlN[12,13,14] or GaN[15,16] is deposited on sapphire before ramping to the standard, high growth temperature (1050°C). This reduced the number of threading dislocations to the general present value of ~10^8 to 10^{10} cm^{-2}. Researchers have exploited the anisotropic growth rates of various crystal faces in GaN through epitaxial lateral overgrowth (commonly referred to as ELO or LEO) of a deposited mask or patterned substrate. In this configuration, GaN grows parallel to the substrate at a faster rate than its perpendicular growth direction. Thus, reasonably large regions of the substrate may be overgrown that do not contain the threading dislocations that propagate up from the nucleation layer/substrate interface. Average dislocation densities for GaN ELO films[1] are typically ~$10^6 cm^{-2}$.

Growth of Aluminum Gallium Nitride

Several groups have attempted to grow AlGaN on sapphire using a LT AlN or GaN buffer layer on (0001) sapphire with limited success. Ito et al.[17] reported that at AlN fractions $x > 0.10$, the quality of the AlGaN layer as measured by high resolution x-ray diffraction rocking curve FWHM deteriorates quickly with increasing x. For $x = 0.43$, plan view transmission electron micrographs revealed a polycrystalline microstructure. Kato et al.[18] attempted to apply the epitaxial lateral overgrowth (ELO) technique that has been successful with GaN to grow AlGaN. They reported difficulty with the non-selectivity of the AlGaN on the SiO_2 mask, thereby making lateral overgrowth problematic.

Amano et al. first investigated the use of LT-GaN interlayers as a method of threading dislocation reduction in GaN overlayers.[19] They found that the number of threading dislocations could be reduced; however, a concomitant increase in growth stress was observed. In later work, Iwaya et al. expanded their investigation to include the study of the effect of using both LT-GaN and LT-AlN interlayers to control stress and dislocations in AlGaN overlayers.[20,21] They found $Al_xGa_{1-x}N$ layers deposited over the entire composition range ($0 \leq x \leq 1$) to be crack-free and of comparable quality to the underlying GaN layers. They claimed that the LT-AlN interlayers "transfer crystalline information of the underlying GaN layer while still suppressing the generation of cracks." They also observed that while the screw- and mixed-dislocation content was reduced in the AlGaN overlayers as compared with the underlying GaN, the number of edge dislocations increased by a factor of 10.

The goals of this work are as follows. First, it endeavors to understand the ultra-rapid catastrophic stress relaxation processes of $Al_{0.20}Ga_{0.80}N$ on GaN. Second, it develops a method of controlling and eliminating cracking in thick $Al_{0.20}Ga_{0.80}N$ layers grown on GaN through the use of low-temperature deposited $Al_yGa_{1-y}N$ interlayers. Third, it aims to use the results of that method to develop thick DBRs based on AlGaN/GaN for the development of the world's first (at the time of announcement) room temperature, quasi-continuous wave optically pumped VCSEL. Finally, it attempts to understand the microstructure of the interlayer and how the interlayer affects the stress in the overgrown AlGaN layer. Key growth parameters of the interlayer such as thickness, temperature, and V/III are varied and the effects on the defect structure of a standard 0.9-μm thick $Al_{0.20}Ga_{0.80}N$ layer are examined by a variety of characterization techniques, including transmission electron microscopy, high resolution x-ray diffraction, and atomic force microscopy.

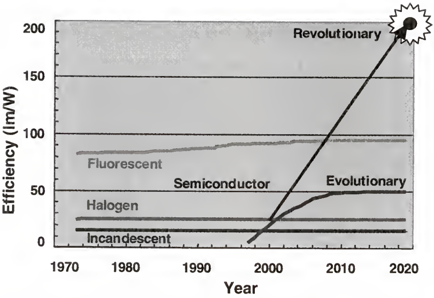

Figure 1 - 1 The evolution of the efficiency of white lighting.

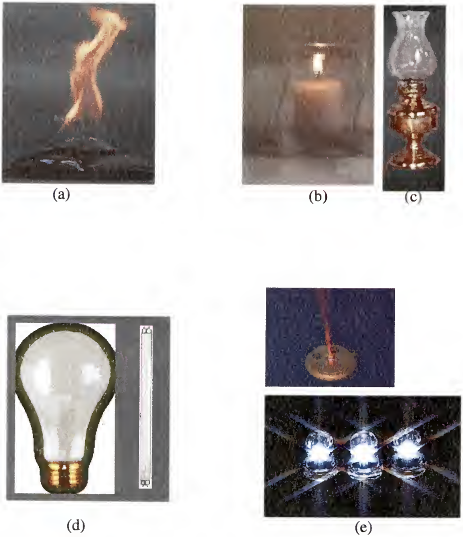
(a) (b) (c)

(d) (e)

Figure 1 - 2 Evolution of white lighting technology: (a) white lighting began with fire; (b) then evolved to candles and (c) oil-burning lamps; (d) finally to electrical sources such as incandescent lightbulbs and fluorescent tubes; (e) and on to the present frontier of solid-state emitters such as LEDs and VCSELs.

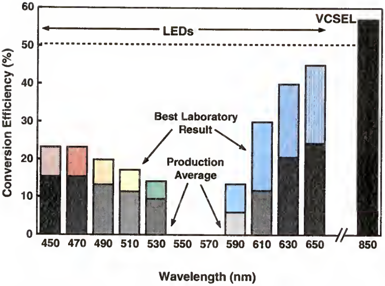

Figure 1 - 3 Conversion efficiency of solid-state light sources vs. wavelength. The solid part of the bar represents the commercially-available efficiency, while the translucent part of the data represents the best laboratory-achieved result.

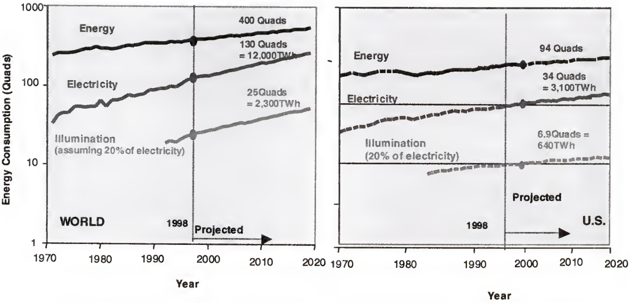

Figure 1 - 44 Economic impact of white lighting globally and in the U.S.

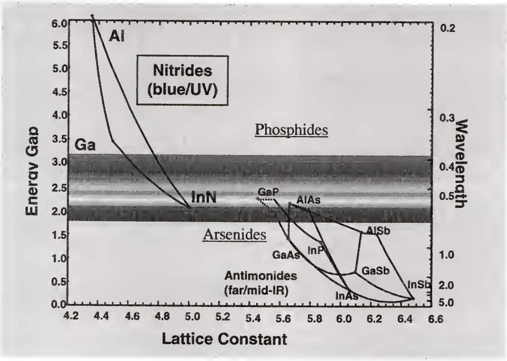

Figure 1 - 5 Bandgap engineering diagram for III-V compound semiconductors. The infrared, visible, and ultraviolet regions of the electromagnetic spectrum are shown.

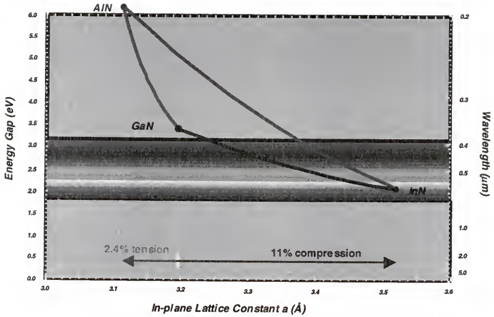

Figure 1 - 6 Bandgap engineering diagram for the III-Nitrides.

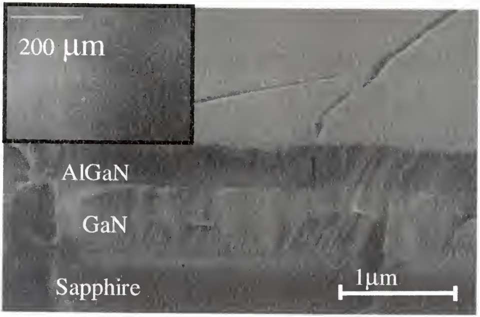

Figure 1 - 7 Obliquely-viewed cross-section scanning electron micrograph of $Al_{0.17}Ga_{0.80}N$ on GaN. The inset is an optical plan-view micrograph showing the crack network density of the film.

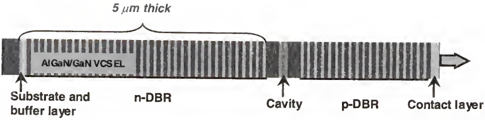

Figure 1 - 8 Schematic structure of a VCSEL.

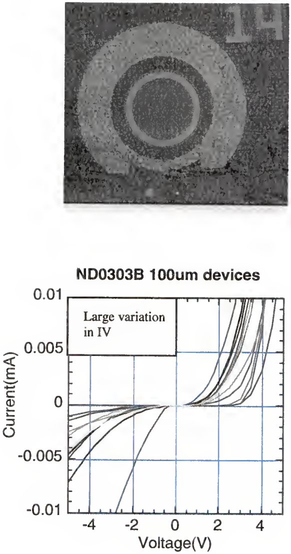

Figure 1 - 9 (a) Cracking network observed in an LED structure consisting of 6000 Å $Al_{0.2}Ga_{0.8}N$ barriers; (b) Current vs. voltage curves for several LEDs manufactured on the same wafer shown in (a).

CHAPTER 2
EXPERIMENTAL PROCEDURE

Chapter 1 described the motivation for studying the III-nitrides for applications in high efficiency solid-state lighting and chemical and biological sensing. The present chapter describes the experimental procedures used to grow and characterize the thin films discussed in the remaining chapters. A brief description of the growth technique, metalorganic chemical vapor deposition (or MOCVD) is given and its merits relative to the other competitive growth technique for epitaxy of semiconductor thin films, molecular beam epitaxy (MBE) are discussed. The *in situ* and *ex situ* characterization techniques that will be employed in this work are described in detail.

Growth Technique: Metalorganic Chemical Vapor Deposition

Metalorganic chemical vapor deposition (MOCVD) is an attractive technique for growth of nitride thin films based on three major considerations. First is the time-wise efficiency of the growth technique relative to molecular beam epitaxy or atomic layer epitaxy and the potential for scale up of the process for technology transfer to high volume, large throughput manufacturing. The second consideration is the production of a good source of nitrogen for reaction. Molecular beam epitaxy of GaN occurs at lower temperatures (~850oC) than for MOCVD, which typically takes place at temperatures >1000oC. The lower temperatures inherent to MBE make the efficient production of a nitrogen radical difficult. Electron cyclotron resonance (ECR) sources have been developed to overcome this and in the past few years this has been less of an issue. The third issue relates to the superior properties of GaN films grown by MOCVD vs. MBE due to the larger grain sizes that are achievable at the higher growth temperatures[22].

All samples discussed in this work have been grown by MOCVD unless otherwise noted. The reactor (Figure 2-1) is a custom-built vertical rotating disk reactor (RDR) developed by Sandia National Laboratories. It consists of a water-cooled quartz tube operating at pressures of ~100 Torr (13.3 kPa). Two-inch c-plane sapphire substrates rest inside a cutout on a silicon carbide-coated graphite susceptor that is inductively heated to approximately 1050°C and rotated at approximately 1200 rpm. The top of the susceptor consists of a Mo plate. The reactants used in the following experiments are ammonia, trimethylgallium (TMG), trimethylaluminum (TMA), trimethylindium (TMI), and disilane (Si2H6). The basic premise of MOCVD is that the reactants are delivered separately in flowing H2 to the surface of the heated substrate where they react and deposit the film according to the following reaction:

$$(CH_3)_3Ga_{(g)} + NH_{3(g)} \rightarrow GaN_{(s)} + CH_{4(g)} \qquad (1)$$

The gaseous by-products are then removed from the surface and exhausted out the bottom of the reactor. A molybdenum plate shields the precursors from excessive heat radiation from the susceptor to prevent prereactions, and a perforated stainless steel screen helps maintain a forced-flow condition in the reactor for laminar flow dynamics. A window at the top of the reactor allows optical access to the substrate.

Valve sequencing of the reactants and carrier gases was controlled through a Dell desktop computer running custom software developed on a Labview platform. Temperature measurement was performed through optical pyrometry at 550 nm of the surface of the susceptor. Feedback to the RF generator was used to ramp and maintain temperature settings. The emissivity of the Mo susceptor is adjusted manually to achieve the proper temperature settings for high quality growth of GaN, which is monitored using an interference reflectometer.

Low temperature GaN buffer layers (~25nm) were deposited on the sapphire substrate at 550oC at 50 Torr. The flow rates of the TMG precursor and the V/III ratio were 54 mmole/min and 5000, respectively. The temperature was then elevated to 1050oC in flowing NH3, while the pressure was raised to 140 Torr. One- to 1.5-mm GaN templates were grown atop the buffer layer using 177 mmol/min of TMG, 2.5 l/min NH3, and 5 l/min H2. The V/III ratio during HT GaN growth was 1500. The growth conditions of interlayers, if used, depended upon the specific experiment being conducted; however, all interlayers presented in this work were grown at 40 Torr with an Al molar flow of 15 mmol/min unless otherwise noted. Growth of AlGaN overlayers was also performed at 1050oC and 40 Torr using 82mmol/min of TMG, 29 mmol/min of TMA, and a V/III of 1100.

In situ Stress Monitor: MOSS

The MOCVD reactor is equipped with an in situ stress monitor ("MOSS") modified for use on the RDR (Figure 2-2). "MOSS" stands for multiple-beam optical stress sensor,[23] and measures wafer curvature via a laser deflectometry technique. A solid-state laser operating at 630 nm is passed through an optic to produce multiple initially parallel laser beams which specularly reflect off of the surface of the wafer and are detected on a CCD camera installed at an angle α from normal incidence above the reactor. If the wafer is flat, then the reflected beams remain parallel. If the wafer exhibits convex curvature (i.e., when the growing film is under biaxial in-plane compression), the reflected beams splay out, and a deviation in spot spacing is detected at the CCD camera. Similarly, if the wafer exhibits a concave curvature, the reflected beams will tend toward convergence at the CCD camera, and a deviation in spot spacing that is opposite in sign will be detected at the camera. MOSS uses the change in reflected beam position to determine wafer curvature (Figure 2-3).[24] Wafer curvature is related to film stress through Stoney's equation[25]

$$K = \frac{6\, h_f\, \sigma}{M_s h_s^2} \tag{2}$$

where hf = film thickness

s = film stress (GPa)

Ms = substrate biaxial modulus (sapphire = 602 GPa)

hs = substrate thickness (330 mm unless otherwise noted)

Thus, the wafer curvature detected by MOSS is proportional to the product of the film stress and the film thickness, or "stress-thickness," to which it will be referred herein. Figure 2-3 depicts the geometrical relationship between the stress-thickness and the change in reflected beam spacing via

$$\sigma \bullet h_f = \frac{\Delta d}{d} \frac{M_s h_s^2 \cos \alpha}{12 L} \qquad (3)$$

where Δd = deviation of spot spacing from original parallel separation d

L = distance between substrate and CCD camera

α = laser beam angle of incidence (taken from normal)

Raw MOSS data are collected through a software package available from k-Space Associates, Inc. and are FFT transformed to filter out high-frequency noise. The software allows the collection of a number of parameters associated with the measurement technique, an important one among them being the power intensity of the reflected beams. Plotting reflected power vs. growth time reveals oscillations in reflected power intensity that arise from the quarter-wavelength thickness interference fringes during growth. The period of these oscillations provides the growth rate of the film to within the accuracy of the known index of refraction at the growth temperature. Once the growth rate of the film is known, the stress-thickness may be plotted against thickness. The use of consistent thickness units (e.g., mm or Å) on both axes allows the direct conversion of slope to stress.

The average slope of the stress-thickness vs. thickness curve represents the average stress in the film, while the derivative of the data provides the instantaneous stress. Figure 2-4 illustrates this distinction more clearly. The derivative of the stress-thickness is just the sum of the partial derivatives. Therefore, changes in stress-thickness during epitaxy may be brought about in two ways. The first (Figure 2-4(a)) is the additional stress resulting from the addition of an incremental amount of thickness of the material, as during growth. The second (Figure 2-4(b)) is due to any kind of bulk relaxation processes that may occur--e.g, cracking and/or nucleation and glide of strain-relieving dislocations. In practice, both of these processes may occur separately or simultaneously. For perfectly coherent epitaxy, only the first process is operative, and the average stress of the film is the same as the slope ($\Delta\sigma \bullet hf = 0$). But for films that roughen, or have exceeded either the Matthews-Blakeslee critical thickness[26] and/or the Griffith's criterion for critical thickness for fracture,[5] one or both of these relaxation processes may be occurring, and the average stress will, in general, differ from the instantaneous stress.

High Resolution X-ray Diffraction Measurements

High-resolution x-ray diffraction was used to determine the microstructural quality, room-temperature strain state, and composition of GaN and AlGaN layers. The microstructural quality was assessed by the full width at half maximum (FWHM) of the (0004) peaks, which is sensitive to the amount of tilting between the subgrains. The amount of twisting was determined using the quasi-symmetric $(10\underline{1}3)$ reflections. In each case, a 1/4° slit was placed before the open detector to better resolve the peaks. The strain state of the GaN is generally constant from run-to-run (Chapter 3), with the (room temperature) in-plane strain state generally falling in the neighborhood of –0.15%. AlGaN will in general be strongly strained; the amount of variation in the in-plane strain state depends upon the growth conditions of the layer and the underlying template. For

(0001)-oriented wurtzite AlGaN, the out-of-plane strain (or "perpendicular" strain) ε_{zz} is related to the in-plane (or "parallel") strain ε_{xx} by the following formula:

$$\varepsilon_{zz} = -2\frac{c_{13}}{c_{33}}\varepsilon_{xx}$$

where c_{13} and c_{33} are the elastic constants.[27] The strains are given by the following equations:

$$\varepsilon_{zz} = \frac{c'-c_o}{c_o}$$

and

$$\varepsilon_{xx} = \frac{a'-a_o}{a_o}$$

where a' (c') are the measured a (c) lattice parameters, respectively, and $\mathbf{a}_o$ and $\mathbf{c}_o$ are the free-standing lattice parameters. The free-standing in-plane lattice constants in the $Al_xGa_{1-x}N$ system range between 3.1892 Å to 3.111 Å for GaN ($x = 0$) to AlN ($x = 1$). Free-standing lattice parameters for the alloy are determined using Vegard's law.

The perpendicular (c') lattice constant of a film may be determined by measuring the $2\theta/\omega$ scan of the symmetrical (0002) reflection using an analyzer crystal before the detector, while the parallel (a') lattice constant may be extracted by performing diffraction analysis on an asymmetric $(20\underline{2}4)$ plane (for example), also using the analyzer crystal before the detector. This is the so-called "triple-axis" mode, referring to the three sets of crystals in the x-ray path: the collimator Ge (220) crystals, the sample crystal to be analyzed, and the analyzer crystal before the detector.

X-ray diffraction was performed using a Philips X'Pert equipped with a hybrid optics set. Ten- and 2-mm vertical and horizontal slits, respectively, were inserted between the incoming beam and the sample. The x-ray beam was monochromated and collimated using a 4-bounce Ge (220) set of crystals. Samples were mounted on a 4-axis goniometer, and the z-position was adjusted using a micrometer calibrated to place the sample within ½ of the beam intensity. The accuracy of the detector position was ensured by calibrating the detector at $2\theta = 0$ before each x-ray run.

Atomic Force Microscopy

The morphology of the interlayers was studied using atomic force microscopy on a Digital Instruments Nanoscope III. The instrument was operated in tapping mode. A silicon cantilever was employed.

Transmission Electron Microscopy

Cross section and plan view transmission electron microscopy (TEM) was performed using a JEOL 200 microscope operating at 200kV. This instrument uses a LaB_6 filament and operates at a typical background pressure of 1×10^{-7} Torr.

Rutherford Backscattering Spectroscopy

Rutherford Backscattering Spectroscopy (RBS) was used to determine the aluminum compositions of the low-temperature deposited AlGaN interlayers described in Chapter 3 and the gallium into AlN diffusion study described in Chapter 5. Backscattering measurements were performed using 2 MeV $^4He^+$ ions and spectra were analyzed by fitting the experimental data with theoretical curves. The parameters of the theoretical curves were adjusted to fit the experimental data.

Photoluminescence

The quality and strain of $Al_{0.20}Ga_{0.80}N$ films were analyzed using photoluminescence spectroscopy (PL) at room temperature. The excitation wavelength of 265 nm was obtained from a frequency-tripled YAG laser. The input power was 0.1 mW, and the detection system was a liquid nitrogen-cooled CCD camera. Band edge emission from the AlGaN was characterized by the FWHM of the peak collected using a grating blazed at 1200 lines per inch and centered at 330 nm. Band edge-to-yellow band ratios were obtained by scanning the photoluminescence emission spectrum with a diffraction grating centered at 410 nm and using 300 lines per inch.

Secondary Ion Mass Spectroscopy

Secondary Ion Mass Spectroscopy (SIMS) measurements of oxygen, aluminum, and gallium were outsourced to Charles Evans & Associates located in Massachusetts. Spectra were collected using MC^+ secondary ions from a Cs primary beam on a Cameca IMS 4F in order to minimize the dependence of ionization and sputter yields on matrix materials. The primary ion impact energy was reduced to 2.5 keV to improve the depth resolution. The gallium concentration in AlN was converted from the secondary ions of $GaCs^+$ by assuming the yield of $GaCs^+$ ions was independent from matrix materials. The primary beam was rastered over 200 x 200 μm^2 and the secondary ions were collected from the crater approximately 30 μm in diameter.

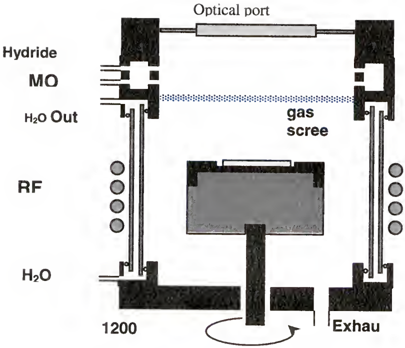

Figure 2 - 1 Custom-built vertical rotating disc reactor.

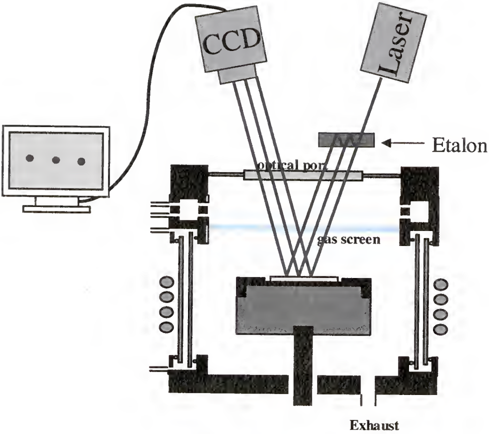

Figure 2 - 2 MOSS system hardware setup.

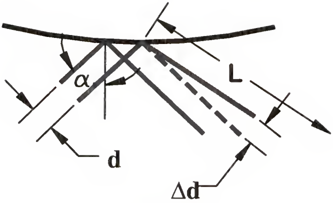

$$\sigma \bullet h_f = \frac{\Delta d}{d}\frac{M_s h_s^2 \cos(\alpha)}{12L}$$

Figure 2 - 3 Geometry of MOSS measurement.

$$\Delta\sigma \bullet h_f = (\Delta\sigma)h_f + \sigma(\Delta h_f)$$

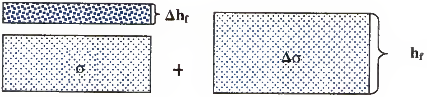

Figure 2 - 4 Physics of MOSS measurement. (a) stress energy increases due to incremental increase in film thickness. (b) stress energy increases at constant thickness due to internal stress creation or relaxation processes.

CHAPTER 3

ULTRA-RAPID CATASTROPHIC RELAXATION PROCESSES IN AlGaN/GaN HETEROSTRUCTURES

Introduction

Ultra-rapid catastrophic relaxation was first observed *in situ* in the AlGaN/GaN system by Han[28] in which ~90% of the accumulated stress in the AlGaN was relieved over a course of approximately 3 seconds. This was initially attributed to cracking; however, subsequent initial studies revealed that the crack density in films that had undergone catastrophic relaxation events did not differ substantially from films of similar composition and thickness that had not. Furthermore, it was determined by Hearne et al. that the crack density in the AlGaN films could account for only ~30% of the observed relaxation. This chapter examines the mechanism(s) of catastrophic relaxation in the AlGaN/GaN system by investigating the misfit dislocation content in three AlGaN/GaN films grown under similar conditions in consecutive growth runs. One film was allowed to catastrophically relax, relieving ~52% of its stress in 3 seconds, while the other two growth runs were terminated prior to catastrophic relaxation. Of those two, one is approximately 300Å thinner than the sample that underwent the ultra-rapid relaxation process; the other is less than half the thickness to provide a comparison of the defect structure at an earlier stage of relaxation.

Mechanics of the AlGaN/GaN Heterosystem

Gallium nitride grown by MOCVD on a LT-GaN or LT-AlN buffer layer deposited at ~550°C on c-plane sapphire exhibits the wurtzite crystal structure and grows on the (0001) face. The lattice constants at room and growth temperature for GaN and AlN are given in Table 3-1,[9] along with the thermal expansion coefficients. There are three first-order slip systems in these materials. The slip plane is the (0001) plane, while slip directions are along the <11$\underline{2}$0> directions.[29] The present interest is in the strain state of AlGaN films epitaxially grown on GaN. There is a 2.54% tensile mismatch between the binary compounds of AlN and GaN at 1050°C. Thus, thin films of AlGaN grown epitaxially on GaN experience in-plane biaxial tension, and there is zero resolved shear stress on the primary slip systems. Therefore it is difficult to nucleate and glide strain-relieving misfit dislocations to the interface. While conventional zincblende III-V compound semiconductors tend to dislocate at or near the Matthews-Blakeslee critical thickness, the Griffith critical thickness for fracture in these materials is predicted to be lower than the Matthews-Blakeslee critical thickness.

Other Investigations

Cracking has been observed in AlGaN films grown on GaN[30,31,32] at thicknesses of 1 µm at $x = 0.11$, and the thickness has been found to decrease rapidly with increasing x. At $x = 0.20$, cracking is expected to occur at approximately 1000Å.[33] Delamination has been observed in AlGaN films with compositions greater than 20%. Hearne et al.[4] confirmed that AlGaN films crack during growth at high temperature as opposed to during cool-down to room temperature. They point out that the difference in coefficient of thermal expansion between AlGaN and GaN places the AlGaN films in compression during cooling, in accordance with Table 3-1.

The work of Hearne et al. found that relaxation occurred in $Al_{0.17}Ga_{0.83}N$ on GaN at a thickness of approximately 1200Å. They found that the crack density in the AlGaN could account for only ~30% of the stress relaxation in the film, while the remaining ~70% was attributed to misfit dislocations at the interface. They also hypothesized in their study that misfit dislocations were unlikely to form in planar AlGaN/GaN films because there is zero resolved shear stress on the strain-relieving slip systems, and there may be large kinetic barriers to glide on higher order slip systems. However, they observed a dense array of misfit dislocations at the interface between AlGaN and GaN in samples that had cracked first, and had found that the misfits had an edge component in the basal plane, which could account for the observed stress relief in the film. They put forth a theory of brittle-ductile relaxation kinetics in AlGaN/GaN in which slip could occur in cracked films, as the strain fields at crack tips relaxed the in-plane biaxial strain conditions and thus produced a resolved shear component on the active slip systems.

Einfeldt et al.[34] studied the strain relaxation of AlGaN on GaN grown by MBE and found that cracks preferentially form along the <2$\underline{1}$10> directions, but occasionally were found to jog along the <1$\underline{1}$00> directions. This was attributed to the smaller surface energy and fewer number of bonds that needed to be broken along the {10$\underline{1}$0} surfaces compared with the {11$\underline{2}$0}. They also found that the appearance of cracks in AlGaN films coincided with the start of stress relaxation as measured by XRD. The average strain energy per unit area was found to saturate at a value of about 4 J/m^2. No microscopy was performed in their work to determine the density or role of dislocation formation; all of the stress relief was assumed to be due to cracking. The crack density was correlated to the strain relief in the AlGaN, and was found to be a suitable lower bound for strain relaxation. Their data suggest that the cracks relieve stress either alone or by initiating some other mechanism of relaxation.

Christiansen et al.[35] investigated low misfitting AlGaN/GaN heterostructures grown by MBE on single crystal GaN substrates with low threading dislocation densities available from Unipress.[36] Three multilayer stacks of AlGaN/GaN were grown using constant composition in each sample ($x = 0.1$, 0.2, and 0.3), and varying the thickness of the layers of AlGaN. Five, ten, twenty, forty, and eighty nm grown layers of AlGaN were grown in succession on 10 nm thick GaN interlayers. In this regime, cracking was not observed; however, stress relief through roughening was observed in $Al_{0.1}Ga_{0.9}N$ at thicknesses beyond 20 nm. This mechanism of relaxation will be discussed further in Chapter 5. The authors claim that from their work, the standard rules of misfit dislocation formation and stress relaxation derived from the zincblende III-V compound semiconductors are applicable to the wurtzite nitrides. Finite element calculations on the structures resulted in a highly non-uniform strain distribution along the slopes of the islands. The authors submitted that misfits could form because of the non-planar strain fields imposed by this surface roughening, and indeed observed a-type dislocations gliding on the basal plane. Thus, perturbations from two-dimensional planar growth are necessary in order to form stress-relieving misfits at the AlGaN/GaN interface.

Experimental Details

AlGaN films containing nominally 20% AlN mole fraction were grown epitaxially on 1 μm GaN on a LT-GaN buffer layer on sapphire by MOCVD using the standard two-step growth procedure (Akasaki). The stress evolution in the films was monitored in situ using MOSS as described in Chapter 2. A set of three structures was grown in back-to-back growth runs. The first AlGaN film was allowed to grow until "catastrophic" relaxation had occurred; that is, until a step-wise reduction in the stress*thickness product had been observed using MOSS. Growth of AlGaN was then terminated and the sample was cooled to room temperature under flowing NH_3. The growth was repeated for the subsequent structure, but the growth was terminated immediately before the first sample had catastrophically relaxed *vis a vis* time. A third AlGaN film was grown, and this time the growth was terminated at an earlier stage of relaxation. The analysis of the samples will be in increasing order of their thickness; in other words, sample "A" is the thinnest, sample "B" is the thicker sample that did not catastrophically relax, and sample "C" is the film that demonstrated catastrophic relaxation.

The crack density in the films was characterized using optical plan view microscopy (Nomarski). AlGaN compositions and average strain values were characterized using high-resolution x-ray diffraction.

Results

Figure 3-1 plots the in situ stress*thickness vs. thickness traces obtained from MOSS for the three samples. The early stages of data collection for Sample C are removed from the plot as the wafer jumped during the transition between 140 Torr for GaN growth and 40 Torr for AlGaN growth and the MOSS data are noisy. The growth rates for each of the samples A, B, and C are given in Table 3-2 and are constant from run to run. The initial stresses in the AlGaN as measured by MOSS for each of the samples are also listed in Table 3-2 and are between 2.1 to 2.35 GPa, taking into account the stress in the GaN, in good agreement with the expected coherency stress values of 2.2 GPa. Exact values for the slopes are difficult to ascertain accurately from these data due to experimental difficulties with the feedback control on the laser power in the software. Growth of AlGaN on GaN has been previously monitored in situ using MOSS without the observation of the changes in slope that are present in the current data. These anomalous changes in slope are reproducible between Samples B and C, but are not readily apparent in Sample A. Changes in film reflectivity that are normal during growth cause differences in the amount of laser intensity that is reflected into the CCD camera detector. When the equipment is functioning properly, the software will control the laser power in order to maintain a constant reflected intensity of the primary laser spot on the CCD camera (usually 90% of the saturation value for the camera). At constant intensity, the areal size of the spots on the camera will remain constant. If, however, the intensity of the reflected beams changes (for example, if the reflectivity of the growing film changes), then the size of the beams on the camera generally will change. The algorithm that the MOSS software uses to determine curvature employs a Gaussian fit to the intensity of the spots in the x and y directions to determine the centroid position of the spots. Changing the size of the spots may alter the calculated centroid position, and thus MOSS will measure an artificial change in relative position of the spots even if the curvature of the wafer has not changed. For this reason, discussions of stresses obtained by slopes of MOSS data in this chapter will be restricted to average or approximate values only.

Certain instructive comparisons may be made in the data, however. For example, by measuring the stress at growth temperature and comparing it to the stress measured by x-ray diffraction at room temperature, the thermal stress for each of the layers may be inferred. Table 3-2 reveals a thermal stress of approximately 1 GPa in each of the AlGaN layers, while a value of 0.8 GPa is obtained for the GaN layers. Although this value for the GaN is somewhat higher than that previously reported,[37] the reproducibility of this result lends confidence to the data, despite the current experimental difficulties.

The step-wise reduction in stress*thickness is observed in Sample C at 3578Å represents a 52% reduction in stress over the course of 3 seconds. However, Nomarski micrographs reveal (Figures 3-2a through 3-2c) that the crack density in the film has not changed significantly during the catastrophic relaxation process, in accordance with the observations of Hearne and Floro. Even at the highest crack densities measured in any of the films (22 micron spacing), cracking is still only expected to relieve less than 5% of the strain. The crack density does not increase substantially after ultra-rapid relaxation takes place.

Preliminary plan view TEM analysis has been performed on Samples A-C. For Sample A (Figure 3-3), a very low misfit dislocation density is present that is consistent with non-catastrophic stress relief observed in other samples grown and monitored using MOSS when it was working better. A low crack density provides the pathway for the introduction of misfits at the interface. Good specimen preparation and analysis was difficult for Samples B and C as the AlGaN on top was so thick. The very thick AlGaN layer made it difficult to find material that was transparent to electron beam that included the interface. Alternative approaches to sample prep, including etching of some of the top surface of the film prior to grinding, polishing, dimpling, and ion milling, are in progress, but results are not available at the time of writing. Despite these problems, preliminary analysis was performed on Samples B and C in the limited areas in which the interface was visible (or what was thought to be the interface). Sample B (Figure 3-4) displays an extremely dense array of misfit dislocations, many of which do not lie along crystallographic directions. This sample is clearly in a very advanced state of misfit dislocation nucleation and multiplication, with dislocations radiating out from both the corners of 60-degree misfit dislocations and other nodes, the source of which is uncertain.

Upon examination of Sample C under bright field TEM on the zone axis (Figure 3-5), very little area of the interface was found to be transparent to the electron beam. The little area that was available for analysis showed an array of very long misfits that formed 60-degree angles. None of the fine structure observed in Sample B was present. This result seems puzzling. There are a couple of possibilities. One popular speculation among the researchers involved in this project is that the analysis was not performed at the interface as originally thought; it is anticipated that alternative specimen preparation methods will provide more confidence in the location of the analysis area. Another speculation is that the catastrophic relief is actually an artifact produced by MOSS. Although no systematic study has yet been performed to determine the reproducibility of this phenomenon, the set of experiments was designed and conducted because this observation had been made before on more than one occasion. Although this may turn out to be the case, it is anticipated that there is some real underlying physics behind this observation; otherwise, MOSS would be expected to show this feature at random times during any deposition. Additionally, if it were an artifact, Samples B and C would be expected to contain similar densities and network structures of misfit dislocations. For the reasons discussed above, it is difficult to confidently state at this point that they do not, but it seems likely that there is a significant difference in the misfit dislocation arrays in Samples B and C. A third possibility that involves the invocation of some physical principles is that the catastrophic stress relief occurs when some kinetic process has been turned on, such as the propagation of strain-relieving misfit dislocations across the interface. This would result in kinks on the <11$\underline{2}$0> faces of cracks, which would be very difficult to observe experimentally. But it would also account for the change in dislocation array observed between Samples B and C.

In summary, the progression of relaxation of AlGaN on GaN appears to progress in the following manner (the initial stages have been worked out by Hearne et al.). AlGaN initially grows coherently strained to the GaN substrate until the critical thickness for fracture has been exceeded, whereupon it grows in a metastable state until cracking is kinetically favored, which depends upon the number of crack nucleation sites (such pits and asperities) that exist in the film. Non-planar strain fields present at crack tips relax the biaxial strain conditions and allow the glide of misfit dislocations down to the AlGaN/GaN interface. Misfits are found far away from crack tips. Dislocation multiplication occurs as the strain energy increases with increasing thickness until catastrophic stress relaxation occurs. It is speculated here that the dislocation density is too high to favor the introduction of more misfits, and so this extra energy is used to activate a kinetic dislocation propagation process by which strain is relieved suddenly. The dislocations are thought to propagate to crack faces and manifest in kinks on the edges of the islands formed by the cracks. This mechanism would imply that catastrophic stress relief is not detrimental to the AlGaN structural quality, which is consistent with the lack of change in (0002) rocking curve widths measured in pre-catastrophic and post-catastrophic samples.

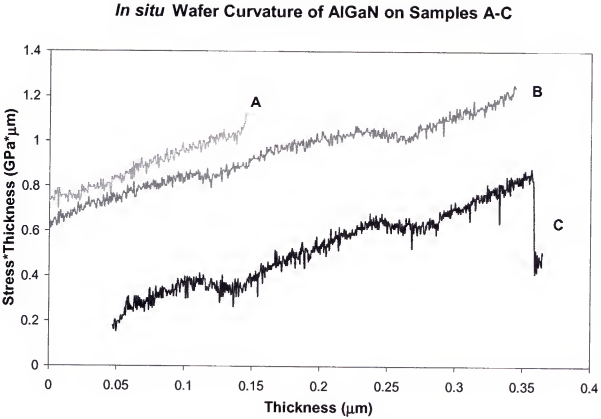

Figure 3 - 1 ***In situ*** **wafer curvature measurements of AlGaN for samples A-C.**

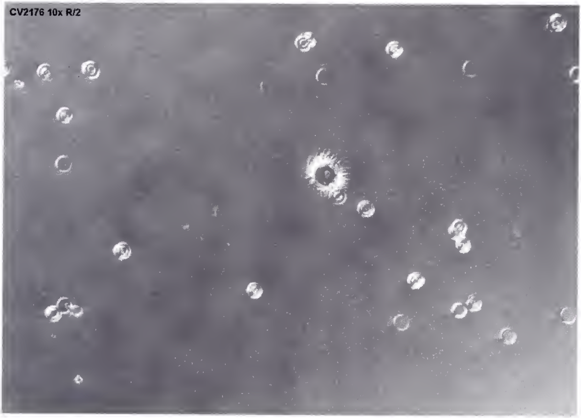

Figure 3 - 2 (a) 100X magnification of Sample A. Cracks were present in the film at very low density. The features on the surface are typically due to too high a growth temperature. The length of the picture is 1430 microns.

I

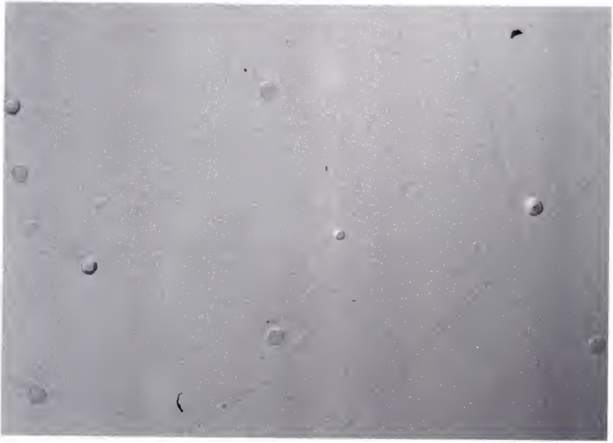

Figure 3 – 2(b) 100X Nomarski micrograph showing the crack density of Sample B at the center of the wafer. The length of the picture is 1430 microns.

Figure 3 – 2(c) 100X Nomarski micrograph showing the crack density on the surface of the center of Sample C. The length of the picture is 1430 microns.

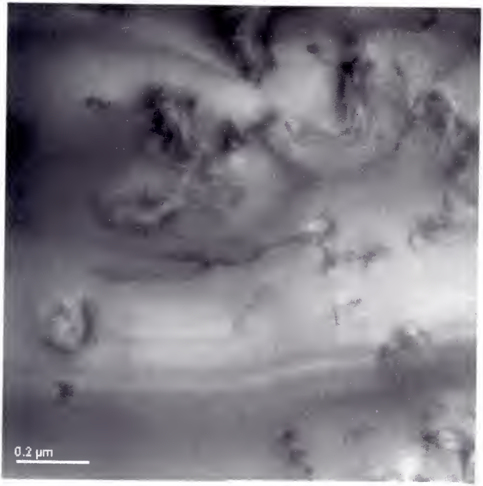

Figure 3 - 3 Plan view transmission electron micrograph taken near the zone axis of sample A. Threading dislocations are present in the AlGaN, along with a misfit dislocation.

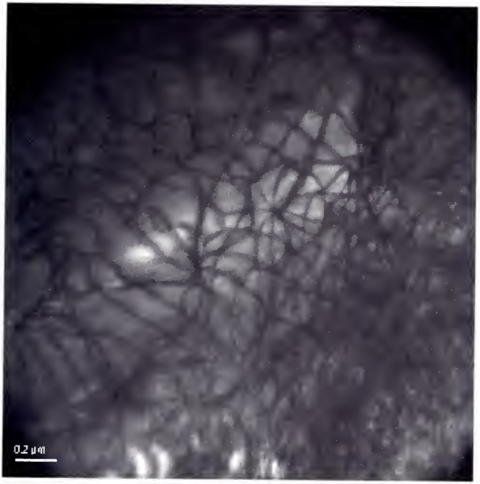

Figure 3 - 4 Plan view TEM micrograph of sample B. The misfit dislocation network is in an advanced state.

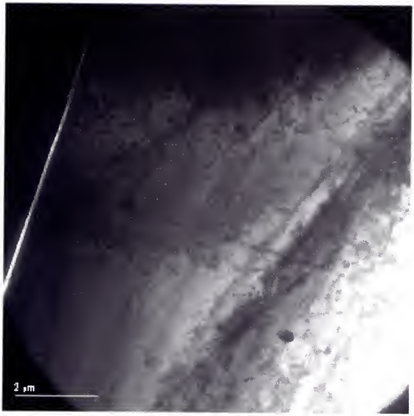

Figure 3 - 5 Plan view TEM of sample C. The intricate network of dislocations is not present at this interface, while a sparse network of longer dislocations lying along crystallographic directions is observed.

Table 3 - 1 Structural parameters of interest for GaN and AlN.

	a(T=25°C) (A)	a(T=1050°C) (A)	M (0001) GPa (GPa)	In-plane TCE $x10^{-6}$/°C
GaN	3.1878	3.2045	450	5.59
AlN	3.1129	3.1318	470	5.3

Table 3 - 2 ***In situ*** **and** ***ex situ*** **analysis of catastrophic stress relief samples.**

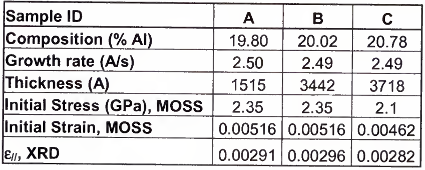

Sample ID	A	B	C
Composition (% Al)	19.80	20.02	20.78
Growth rate (A/s)	2.50	2.49	2.49
Thickness (A)	1515	3442	3718
Initial Stress (GPa), MOSS	2.35	2.35	2.1
Initial Strain, MOSS	0.00516	0.00516	0.00462
$\varepsilon_{//}$, XRD	0.00291	0.00296	0.00282

CHAPTER 4

CONTROL AND ELIMINATION OF CRACKING IN $Al_{0.20}Ga_{0.80}N$ USING $Al_xGa_{1-x}N$ INTERLAYERS

Introduction

As seen in Chapter 3, the source of the tensile stress in AlGaN films grown on GaN templates is the in-plane lattice mismatch between AlGaN and GaN. Due to the nature of the crystal structure and growth direction, and the lack of available low-energy slip systems, the AlGaN is incapable of the nucleation and glide of strain-relieving dislocations. The build-up of tensile stress energy causes fracture of modest aluminum-fraction alloys at thicknesses on the order of 1,000Å, rendering them essentially useless for optoelectronic device fabrication. One approach to solving this problem is to modify the interface between the AlGaN and the GaN by inserting a thin layer between the two thicker layers. Ideally, this "interlayer" will relax and redefine the in-plane lattice parameter for subsequent growth. Thus, the AlGaN overlayers grow in a reduced strain-state.

Amano et al. in collaboration with Sandia National Laboratories first used interlayers.[38] In that work, thin (25 nm) layers of GaN deposited at low-temperature (LT) (550°C) were inserted between 1-mm thick layers of regular, high-temperature (HT) deposited GaN (Figure 4-1(a)). The initial layers consisted of the standard two-step growth procedure on sapphire with one micron of GaN, and the "number of repeats" refers to the number of times this procedure was repeated. Amano was interested in using the LT-GaN as a dislocation filter, mimicking the use of the LT-GaN buffer layer that is necessary for the growth of decent quality HT-GaN on sapphire.[39] As shown in Figure 4-1(b), the density of threading dislocations was observed to decrease as a function of the number of LT-interlayer repeats used. Interestingly, a concomitant increase in growth stress was observed, as shown in Figure 4-1(c).

Han et al. attempted to bypass the growth of the HT-GaN on sapphire and grow high quality AlGaN on a buffer layer on sapphire and observed that the initial stress of HT-AlGaN layers grown under identical conditions but upon different surfaces was affected by the growth template. They observed a high growth stress consistent with the stress expected due to the mismatch between the AlGaN and the GaN when AlGaN was grown on HT-GaN. If the AlGaN layer was grown on a LT-GaN buffer layer on sapphire, the tensile stress was observed to decrease significantly in magnitude, while nominally the same HT-AlGaN layer grown on a LT-AlN buffer layer on sapphire was observed to grow initially in compression. Thus, the Han group concluded that these thin layers were effective in manipulating the growth stress of AlGaN. The combination of the two results led to the present idea of inserting thin, low temperature ternary alloy AlGaN interlayers for stress control in the AlGaN/GaN heterosystem.[40]

The remainder of the chapter is dedicated to understanding how to control strain and eliminate cracking in $Al_{0.20}Ga_{0.80}N$ on GaN. In the following subsections, the use of interlayers and their effect on the strain state and defect structure of nominally 0.9-μm thick $Al_{0.20}Ga_{0.80}N$ will be explored. The first subsection will investigate the effects of changing the composition of interlayers to control and eliminate cracking in AlGaN overlayers. After determining that thin AlN interlayers deposited at low temperature are the most effective in controlling stress, other growth parameters will be explored using AlN as the standard composition. The temperature will be varied, and it will be discovered that thin (135Å) AlN interlayers deposited at high temperature (1050°C) are even more effective in controlling stress than their LT-deposited counterparts. Now using the 135Å HT-AlN interlayer as a base, the thickness of the interlayer will be varied and the effects on the overlayer will be studied. Finally, still using the 135Å HT-AlN interlayer as a base, the V/III ratio will be lowered from the standard AlN growth conditions developed historically in the rotating disk reactor, and the effects of changing this parameter will be studied.

Low-Temperature Deposited Ternary Alloy Interlayers

Five samples of 0.9-µm thick $Al_{0.20}$Ga0.80N ("HT-AlGaN") are grown on top of standard HT-GaN (1µm thick), but 135Å of LT-$Al_xGa_{1-x}N$ interlayer is inserted between the HT-GaN and HT-AlGaN for stress control. All samples are identical with the exception of the composition of the interlayer, which is varied between $0 \geq x \geq 1$ (Figure 4-2(a)). Figure 4-2(b) plots the MOCVD growth sequence (temperature vs. time). After the deposition of HT-GaN at 140 Torr and 1050°C, the temperature was lowered to 700oC and the pressure was lowered to 40 Torr. After stabilization of temperature and pressure, approximately 135Å of interlayer was deposited, and the temperature was returned to 1050°C (the pressure remained at 40 Torr). Subsequently, 0.9-µm of $Al_{0.20}Ga_{0.80}N$ was deposited. The stress evolution of the structures was monitored in situ using MOSS.

The strain relaxation of the 135-Å thick ternary LT-interlayers was investigated using a combination of *in situ* and *ex situ* characterization techniques. The *in situ* characterization quantified the growth stress, while the ex situ characterization quantified the composition of the layers. In addition to using the binary AlN interlayers as reported previously,[41] the present investigation was extended into the ternary alloys based on two considerations. First, AlN is normally insulating and may not be compatible with devices requiring vertical current transport. Second, the employment of AlGaN should render direct tunability of the in-plane lattice parameter, which is what dictates the stress in the subsequently grown layer.

The Al composition of the LT interlayers (x_{LT}) was determined by Rutherford backscattering spectrometry (RBS)[42] using a 2.5 MeV $^4He^+$ ion beam. RBS was performed on a separate set of 400-Å thick LT-AlGaN calibration samples grown in the same manner as the five test structures, but without the HT-AlGaN capping layers. The composition of the thicker HT-AlGaN layers (xHT) was directly measured using high-resolution x-ray diffraction spectrometry (XRD). Symmetric (0002) and asymmetric (20$\underline{2}$4) reflections were used to determine both in-plane (a) and out-of-plane (c) lattice parameters. Once the strained a and c lattice parameters were measured, corresponding unstrained lattice parameters, elastic strains, and Al compositions were computed from elasticity theory[43] assuming Vegard's law holds for the unstrained lattice parameters[44] and elastic constants.[27] The resulting RBS (for x_{LT}) and XRD (for x_{HT}) compositions are listed in Table 4-1.

The results from the real-time, *in situ* stress monitoring using MOSS for the five samples are shown in Figure 4-3. Due to the offsets in growth time resulting from the different compositions of the interlayers (interlayer growth rates decrease with increasing aluminum nitride mole fraction under our growth conditions), the five traces are plotted against growth time in order to present them in a single graph for comparison. Growth times may be converted to thicknesses by the appropriate growth rate derived from the quarter wavelength interference fringes from the intensity of the reflected laser beams[37] (see Chapter 2), and therefore the slopes of the curves are comparable to within the slight variation in growth rates from run-to-run. Similar to our previous observations,[37] the growth of GaN on LT-GaN buffers (Region II in Figure 4-3) exhibited a characteristic residual tensile stress (sGaN) that varies between 0.35 and 0.56 GPa (see Table 4-1). A much wider difference, however, was observed in the variation of the initial growth stress (sHT-AlGaN) of the HT AlGaN layers (Region IV in Figure 4-3) on the interlayers. Very steep positive slopes, accompanied by successive step-wise reduction in the stress-thickness (indicating relaxation), were seen in the samples grown on LT-GaN (x = 0) and on LT-$Al_{0.34}Ga_{0.66}N$. As the Al composition in the interlayers was increased from LT-GaN to LT-AlN, the magnitude of the tensile stress gradually decreased. The sample grown using the binary AlN interlayer exhibited a negative slope indicative of initial compressive stress.

Surface cracking of the five samples (A-E) was examined using a differential interference-contrast Nomarski[45] microscope. The results are shown in Figure 4-4(a-e). The critical thickness for fracture (hg) was also calculated using Griffith's criterion for crack propagation[46] and in Table 4-2 are compared with the Nomarski micrographs in Figure 4-4. Recalling that the HT-$Al_{0.2}Ga_{0.8}N$ layer is 0.9μm thick, consistent results are found. As expected, the LT-GaN interlayer, which produces no relaxation of HT-AlGaN coherency stress, has a critical thickness for fracture much smaller than the HT-layer thickness. The result is the highest degree of cracking as seen in Figure 4-4(a). Addition of intermediate amounts of Al (x_{LT} = 0.35-0.42) to the LT interlayer reduces the HT-AlGaN coherency stress and increases h_g ~ 4X. Cracking is still observed in Figures 4-4(b) and 4-4(c) since the HT-AlGaN thickness is still about twice that of the HT-AlGaN thickness. Increasing the LT-interlayer composition to x_{LT} = 0.62 raises h_g by ~30X--now far above the critical thickness for fracture for that layer. Figure 4-4(d) reveals that the HT-$Al_{0.2}Ga_{0.8}N$ growth is appropriately crack-free. Finally, as the LT-interlayer composition becomes pure AlN, the HT-AlGaN moves into compression; crack propagation can no longer be driven by composition-induced stress as seen in Figure 4-4(e).

A key parameter in employing the interlayer scheme is the degree of pseudomorphism of the LT interlayers. Information on the in-plane lattice constants of the interlayers immediately before the nucleation of HT-AlGaN layers is required to determine the degree of coherency. This lattice information is replicated during initial and presumably coherent growth of HT AlGaN layers and can be "captured" with the use of the in situ stress sensor before relaxation takes place; the HT-AlGaN test layers thus serve as "probes" to yield the lattice parameters of the underlying interlayers. The stress evolution of the interlayers themselves is not accurately available due to the limitations in resolution of the stress monitor due to the thickness of the sapphire substrate. The methodology of extracting the degree of lattice strain relaxation of the interlayers is presented in the following. In brief, the use of XRD and RBS provide the Al concentrations in the HT-AlGaN (x_{HT}) and LT-AlGaN (x_{LT}) interlayers, respectively. The slopes measured via MOSS during initial growth of HT-AlGaN layers and during HT-GaN yield instantaneous growth stresses, $\sigma_{HT\text{-}AlGaN}$ and σ_{GaN}, respectively. The measured stresses were converted to strains ($\varepsilon_{HT\text{-}AlGaN}$ and ε_{GaN}) using the biaxial bulk modulus ($\varepsilon = \sigma/M$, $M = 449.6$ GPa[27]). Assuming initial coherent growth of HT-AlGaN test layers on the LT interlayers, the in-plane lattice constant of the LT-AlGaN interlayers can be expressed as $a_{LT\text{-}AlGaN} = a_{HT\text{-}AlGaN} = (1+ \varepsilon_{HT\text{-}AlGaN})a_0(x_{HT})$, where $a_0(x_{HT})$ is the in-plane lattice constant of the free-standing AlGaN. With the knowledge of $a_{LT\text{-}AlGaN}$, $a_0(x_{LT})$, and $a_{GaN} = (1+\varepsilon_{GaN})$, the fraction of the strain relief can be approximated to be $[a_{GaN} - a_{LT\text{-}AlGaN}]/[a_{GaN}-a_0(x_{LT})]$. All of the parameters are summarized in Table 4-1.

The fact that $a_{HT\text{-}AlGaN}$ for the LT-GaN interlayer, which was derived from a combination of stress ($\sigma_{HT\text{-}AlGaN}$) during AlGaN growth and Al concentration (x_{HT}) from XRD, approaches a_{GaN} lends strong support to both the assumption of an initial coherent HT-AlGaN growth and the validity of current treatment combining *in situ* and *ex situ* characterizations. It is clear from Table 4-1 (columns $a_{LT\text{-}AlGaN}$ and a_{GaN}) that crack suppression through stress engineering is based on the ability to vary the in-plane lattice parameters of the LT interlayers. Under the growth conditions employed in this work, the deposition of LT $Al_xGa_{1-x}N$ interlayers produced templates with in-plane lattice constants equal to those of free-standing $Al_yGa_{1-y}N$ with $y \sim x/3$. The observed partial lattice relaxation in the LT interlayers was possibly accomplished through the nucleation and gliding of edge-dislocations on the basal (0001) plane[4] between LT interlayers and the HT-GaN. The geometrical constraints for nucleation and gliding of misfit dislocation during planar, coherent heteroepitaxy in wurtzite systems[47] are likely lifted due to the alteration of the microstructure. Atomic force microscopy performed on as-grown interlayers revealed the presence of non-planar discrete and/or interconnected islands. Such a change in microstructure causes a highly inhomogeneous, non-biaxial distribution of the strain field, which makes the admission of misfit dislocations energetically favorable. Alternatively, strain relaxation of the LT interlayers might occur through initial cracking and subsequent dislocating; the final, crack-free HT-AlGaN layers would then be the result of lateral growth over the cracks. Note that in the crack-free samples containing $x_{LT} = 0.62\text{-}1.00$, the structural quality of the 0.9 μm AlGaN layers was equal to the underlying GaN pseudosubstrates as indicated by the double-crystal x-ray diffraction rocking curve linewidths using (0004) diffraction (~320 arcsec for both AlGaN and GaN); see Figure 4-5.

In conclusion, it has been found that the use of LT-AlGaN interlayers is effective in "redefining" the in-plane lattice parameter through strain relaxation. The interlayers serve to mediate the elastic tensile mismatch between the adjacent layers and extend the cracking critical thickness. It is anticipated that the interlayer scheme will greatly increase the flexibility in the heteroepitaxy of AlGaN-based devices.

Investigation of the Effect of Growth Temperature of AlN Interlayers on the Defect Structure of $Al_{0.20}Ga_{0.80}N$ Overlayers

It was found in the initial study that low-temperature deposited AlN interlayers were the most effective in controlling the stress in the overgrown $Al_{0.20}Ga_{0.80}N$ layer. Further exploration of AlN interlayer growth parameter space was conducted in an effort to optimize interlayers for specific device applications. It was discovered during the growth of distributed Bragg reflectors (DBRs) for VCSELs that AlN interlayers deposited at the standard growth temperature of 1050°C were even more effective in controlling the stress in the DBRs than were the low-temperature deposited layers (see Chapter 6). Figure 4-6 illustrates the difference in the amount of compressive stress that is generated in DBRs grown on LT-AlN vs. HT-AlN. From a growth standpoint, this is a very convenient result since it is much more efficient to not change temperature during growth to deposit the interlayer. In this subsection, the stress and microstructure of $\mathrm{Al_{0.20}Ga_{0.80}N}$ layers grown on top of AlN interlayers deposited at low (700°C) and high (1050°C) temperature will be compared.

Figure 4-7 presents the MOSS data obtained from the growth of $\mathrm{Al_{0.20}Ga_{0.80}N}$ on nominally 135Å of AlN grown at 1050°C. Just as in the low temperature AlGaN interlayer experiments presented in the previous section, the initial slope is used to determine the in-plane lattice parameter, and thus the strain state of the AlN interlayer. In contrast to the low-temperature AlN interlayers, the strain state of the AlN interlayer may also be measured directly as the growth time is much longer (409 seconds under these conditions) and compared with the strain state observed from the initial slope of the AlGaN overlayer. The results from the two approaches are in good agreement. Optical inspection of the surface of 0.9-µm thick AlGaN layers grown on HT AlN interlayers confirms that the surface is crack-free.

The residual strain in the AlGaN and the GaN can be determined from analyzing the peak positions of radial scans obtained from x-ray diffraction of the (0002) and $(10\underline{1}3)$ planes. The resulting in-plane residual stresses displayed in Figure 4-8 reveal that AlGaN layers grown on the HT AlN interlayers are in a higher state of compressive strain as compared with the LT AlN interlayer, which agrees well qualitatively with the in situ MOSS data. Quantitatively, however, the difference in the stress in the AlGaN layer measured at high temperature (by measuring the stress during the last ~3000Å of AlGaN growth) and subtracting the residual stress measured by x-ray diffraction yields a higher result than expected from thermal stress alone by approximately 0.5 GPa. This may be an indication that the interlayer restrains during anneal or on cool-down.

An increase in the line width of the band edge photoluminescence (PL) emission from the 20% AlGaN layers of about 10% may indicate that the quality of the AlGaN deteriorates slightly on the HT AlN layers as compared with the LT AlN interlayers (Figure 4-9). Another diagnostic for layer quality is the ratio of the band edge to yellow band emission. Although the exact origin of the yellow band emission in GaN and AlGaN is not well understood, it is generally accepted to be related to impurities or native defects in the material. Thus the higher the band edge-to-yellow band (BE/YB) ratio, the higher is the quality of the film. Figure 4-9 also displays the BE/YB of AlGaN layers as a function of AlN interlayer growth temperature. The BE/YB decreases to below unity for AlGaN grown on HT AlN interlayers, again suggesting that AlGaN grown on LT AlN interlayers is of superior structural quality.

Cross sectional transmission electron microscopy (TEM) was performed on the LT-AlN interlayer sample using the standard grind, dimple and ion mill technique. A micrograph taken under the (0002) two-beam bright field condition is shown in Figure 4-10. Figure 4-11 is an image the same LT-AlN interlayer structure taken under a $(11\underline{2}0)$ reflection for comparison. The same analysis was performed on the HT-AlN interlayer specimen, although it was prepared by a dual focused ion beam technique using a liquid gallium ion source. The (0002) bright field two-beam image is similar to the LT-AlN interlayer sample and is not shown. The bright field image taken under the $(1\underline{1}00)$ 2-beam condition is shown in Figure 4-12. The bright field images constructed using (0002) reflection illuminate dislocations with Burgers vectors with c-components, or screw dislocations. With respect to the underlying GaN, no new screw dislocations are generated by the interlayers under either deposition condition; in fact, screw dislocations appear to be filtered out by the interlayers. However, inspection of Figures 4-11 and 4-12 reveals that many more edge dislocations are generated in the AlGaN compared with the underlying GaN. The HT-AlN interlayer generates about an order of magnitude more threading dislocations in the AlGaN than does the LT-AlN interlayer, which is consistent with the relaxation observed in the interlayers as measured by the initial strain state of the AlGaN overlayers. Although threading dislocations are undesirable for device purposes, edge dislocations are preferable to screw dislocations for electronic transport considerations. In the case of the DBRs and VCSELs described in Chapter 6, the increase in threading dislocation content does not appear to have deleterious consequences for optical device performance. Efforts to measure the Hall mobility and carrier concentration were unsuccessful on the AlGaN overlayers; it seems that the charge carrier concentration in these samples was insufficient to obtain useful information.

In summary, it has been shown that AlN interlayers deposited at high temperature (1050°C) relax more than do AlN interlayers deposited at 700°C, thereby providing a smaller lattice template for subsequent AlGaN growth. While this is a convenient result from a growth perspective, the increase in threading dislocation density introduced by the additional relaxation of the interlayer may be deleterious to the performance of some devices, though that has not been explored here but is suggested from optical measurements on the samples. However, the high temperature interlayer scheme may be useful for devices that require very thick AlGaN/GaN-based structures or for high Al-content overlayers to prevent cracking.

Investigation of AlN Interlayer Thickness on Defect Structure of $Al_{0.20}Ga_{0.80}N$ Overlayers

The thickness of the AlN interlayer was varied at a constant temperature of 1050°C. Thicknesses of 68Å, the "standard" 135Å, and 300Å were chosen. Interlayer thickness was calibrated previously by growing a thick layer of AlN on GaN and measuring the width of the thickness fringes on the (0002) planes by triple-crystal x-ray diffraction. Growth rates were assumed to be constant with thickness. X-ray diffraction of 135Å and 300Å AlN layers without AlGaN overlayers have been performed (see Chapter 5), and the thicknesses obtained from the fringes on the peaks were verified *ex situ* and found to be in good agreement with the expected thicknesses; therefore, this assumption appears to be valid. Nomarski microscopy revealed that all AlGaN layers were crack-free.

In situ wafer curvature measurements taken during AlGaN growth for the three samples are presented in Figure 4-13. The AlGaN overlayer grows in tension on the thinnest layer, is put in the most compression for the 135Å interlayer, and grows in a reduced state of compression on the 300Å interlayer. These data suggest that the 300Å AlN film appears to have restrained relative to the 135Å interlayer, while the 68Å AlN film is less relaxed. The AlGaN overlayer remains in tension throughout the growth but as noted above, remains crack-free.

The microstructural quality of AlGaN overlayers and the underlying GaN was evaluated using x-ray diffraction. AlGaN and GaN rocking curve line width data for the (0002) reflection are incorporated in Figure 4-5. Rocking curves were attempted for the

$(10\underline{1}0)$ planes, but were unsuccessful due to instrumental limitations. Figure 4-14 plots the FWHM obtained from triple-crystal (0002) x-ray diffraction radial scans of the AlGaN and GaN layers as a function of interlayer thickness, and Figure 4-15 shows the same for the $(10\underline{1}3)$ reflection. The narrowest features along the (0002) direction in k-space are observed for AlGaN layers grown on the thinner AlN interlayers. The (0002) width is about a factor of 2-3 narrower for AlGaN grown on the thinner layers than for the thicker layers. The feature sizes do not change as much for AlGaN grown on 135 vs. 300Å, although a slight narrowing is observed for the AlGaN grown on the thickest interlayer. The FWHMs of the underlying GaN are displayed for comparison. While the AlGaN data tends to follow the GaN data, it also appears to exaggerate the differences. In other words, the differences in the out-of-plane strain dispersion in the GaN from sample to sample appear to be magnified in the AlGaN after the use of the interlayer. The linewidths measured along the $(10\underline{1}3)$ direction represent a non-trivial convolution of the in-plane and out-of-plane strain dispersions, and without fully understanding that relationship, this information yields only qualitative results as to the amount of in-plane strain dispersion. Figure 4-17 shows the in-plane strain state of the AlGaN (and underlying GaN) as determined by XRD as a function of interlayer thickness, including data from AlGaN on GaN without an interlayer (sample “C” from Chapter 3). While AlGaN grown on GaN without an interlayer remains in residual tension at room temperature, Figure 4-17 demonstrates that even a 68Å interlayer can result in residual compressive strain for AlGaN overlayers. While 135Å interlayers increase the amount of residual compression in the layer, the amount of residual compressive strain appears to saturate for increasing interlayer thicknesses beyond this value. However, this conclusion is based on a single data point (at 300Å) and further experimentation is required in order to confirm or refute this statement.

Measurement of photoluminescence line widths shown in Figure 4-9 indicates that for the interlayer thicknesses investigated here, the structural quality of the AlGaN layers is the poorest for the "standard" 135Å condition. The line widths are fairly close for the thick and thin layers, although the 300Å interlayer sample is slightly narrower than the 68Å sample. Band edge-to-yellow edge ratios indicate however that AlGaN deposited on 300Å interlayer has a greater number of optically active defects in the layer. The AlGaN BE/YB photoluminescence emission results for the interlayer thickness variation experiments are incorporated in Figure 4-9.

In summary, for AlN interlayers deposited at 1050°C using a V/III of 1100, it appears that 68Å of AlN will reduce the amount of tensile stress in the $Al_{0.20}Ga_{0.80}N$ during growth to prevent cracking, at least for samples analyzed here. It is clear from x-ray diffraction data though that the AlN interlayer does reduce the in-plane tension relative to not inserting an interlayer while still maintaining good structural quality of the AlGaN overlayer. Increasing the thickness of the AlN interlayer can further increase the residual compressive stress in the AlGaN overlayers, but appears to saturate beyond 135Å. More data points are required to discern this trend more accurately. Analysis of x-ray diffraction line widths indicates that the thinnest layers are the least disruptive to the subsequent AlGaN microstructure, even possibly reducing slightly the amount of tilting observed in the subgrains relative to the underlying GaN. Thinner layers also adversely affect the optical quality of AlGaN overlayers the least. Therefore, the end application should be considered when choosing an interlayer thickness. The best approach would be to use the minimum thickness of AlN necessary to keep the AlGaN overlayer from cracking to maintain the highest quality overlayer.

Investigation of AlN V/III Ratio Variation on $Al_{0.20}Ga_{0.80}N$ Overlayers

The final interlayer growth parameter that has been explored in this work is the V/III ratio. Interlayers were grown under three different V/III conditions (1100, 660, and 265), maintaining an AlN nominal thickness of 135Å and growth temperature of 1050°C. The growth rates at each V/III were determined in a separate growth run that was performed just before the growth of the full stack structure. AlN thickness was determined in situ using interference reflectometry and verified ex situ using the thickness fringes in the (0002) reflection under triple-crystal diffraction. Growth rates were assumed to be constant with thickness, and were found to vary by less than 20% over the investigated V/III ratio range. The surfaces of all AlGaN overlayers were inspected optically by Nomarski imaging and found to be crack-free over the range of V/III ratios explored in this study.

Unfortunately, due to emergency changes in reactor hardware (specifically, the susceptor) that adversely affected wafer stability during growth, MOSS data are not available on samples discussed from this point forward in the chapter. Therefore, only ex situ analysis of the AlN interlayer and AlGaN overlayer are available at this time. As the strain state evolves substantially during the growth of the ~0.9 μm of AlGaN, it is difficult to determine the exact strain state of the AlN as a function of thickness by measuring the residual stress in the AlGaN overlayer. However, upon examination of Figures 3-2, 4-11, and 4-12, it is clear that employing the interlayer scheme allows the engineer to trade one defect in the AlGaN for another; namely, cracking for edge dislocations. From a device engineering perspective, it is instructive to examine the defect density in AlGaN overlayers generated by AlN interlayers so that the interlayer design may be tailored for the specific device application.

Analysis of x-ray diffraction (0002) line widths (Figure 4-5) reveals that no significant change in tilting is observed for any V/III ratio studied here. The amount of strain dispersion on $(10\underline{1}3)$ inclined plane reflection follows a monotonic trend with decreasing V/III ratio, and the lowest dispersion occurs at the minimum V/III investigated. The in-plane strain is plotted against V/III ratio in Figure 4-17 for the three conditions listed here; the in-plane strain observed for AlGaN on GaN with no interlayer is plotted for comparison at an ordinate value of zero. This is meant to convey that no interlayer was used, as indicated on the plot, and not that an interlayer was grown at a meaningless V/III = 0. This depiction is useful to understand the value of employing the AlN interlayer and the data shown for V/III = 0 are again for the sample that underwent catastrophic relaxation in Chapter 3 (sample "C"). The residual stress in AlGaN overlayers increases with increasing V/III.

Photoluminescence results for AlGaN overlayers as a function of V/III are plotted in Figure 4-9. The linewidth sharpness of the band edge emission of the overlayer improves by 14% at the lowest V/III compared with the standard V/III = 1100. Optically, the highest quality layer as judged from band edge-to-yellow band emission is grown atop an AlN interlayer grown with a V/III ratio of 660.

In summary, AlN interlayers grown using low V/III ratios appear to exhibit slightly less relaxation than those grown at higher V/III. Changing the V/III ratio does not appear to affect the amount of tilting in AlGaN overlayers as measured by x-ray diffraction, and the optical quality of the AlGaN layers is improved by lowering the V/III ratio of the AlN interlayer.

Discussion and Summary

It has been demonstrated that $Al_xGa_{1-x}N$ interlayers may be used to control growth stress and eliminate cracking in 0.9-μm thick $Al_{0.20}Ga_{0.80}N$ layers grown on GaN. The strain state of thin interlayers embedded in thick heterostructures has been determined during growth and found that interlayers partially relax, thereby redefining the in-plane lattice constant for subsequent AlGaN overgrowth. The growth parameter space of interlayers has been explored; namely the effect of changing the composition, growth temperature, thickness, and V/III ratio on the strain state and defect density of AlGaN overlayers has been studied. In all cases it has been found that although AlN interlayers eliminate cracking in subsequently grown AlGaN overlayers, there is a price to pay in terms of threading dislocation content. Fortunately for electronic-based device applications, the interlayers do filter screw dislocations but increase the density of edge dislocations. This defect structure is consistent with a theory that includes relaxation of the interlayer through the introduction of misfit dislocations at the interlayer/GaN interface, whereby the threading segments (with a-component Burgers vectors) then propagate up through the AlGaN overlayer. It is suggested that the rough morphology of low temperature deposited AlGaN interlayers relaxes the geometrical constraints on the biaxial strain field present along (0001), thereby making it energetically favorable to nucleate and glide misfits to the interface. Presumably the morphology, and thus the amount of relaxation that may occur in the interlayer, are affected by growth conditions such as interlayer composition, deposition temperature, thickness, and V/III ratio. The mechanisms of relaxation of the AlN interlayers will be explored further in Chapter 5.

Some insights may be gained into the use of the interlayer. High temperature AlN interlayers are the "strongest" in terms of stress control, and are appropriate for devices that require crack-free layers of high aluminum-containing alloy films or thick layers. Although electrical Hall measurements were attempted and were unsuccessful (presumably due to the low doping levels present in the AlGaN), it is speculated that the threading dislocation content may be detrimental to the transport properties of charge carriers. Therefore if excellent electrical properties are the desired device feature, the engineer may choose to carefully balance the stress with threading dislocation content by employing thinner AlN or choosing a different concentration for the interlayer. The V/III ratio results are interesting and should be explored further. Knowledge of the overlayer properties as a function of interlayer thickness variations at lower V/III ratios than the ones employed in this study would be useful.

In conclusion, cracking in AlGaN overlayers can be controlled and eliminated through the use of (Al,Ga)N interlayers. The strain state of the overlayers is controlled by the strain state of the interlayers, which is in turn controlled by the growth conditions, such as composition, deposition temperature, thickness, and V/III ratio. Further study into the defect structure of the overlayers (for example, via cross section TEM) is required in order to verify the hypothesis that the interlayer is relaxing by introducing misfit dislocations at the interlayer/GaN interface, whose threading segments then propagate up through the overlayer and may potentially deteriorate the electrical device performance.

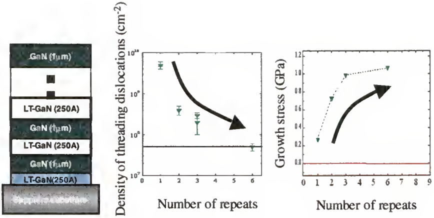

(a) (b) (c)

Figure 4 - 1 (a) Schematic stack structure of samples investigated in the Amano et al. LT-GaN interlayer experiments. (b) Threading dislocation density observed in HT-GaN overlayers vs. the number of LT-GaN interlayers employed. (c) Growth stress in HT-GaN overlayers as a function of the number of LT-GaN interlayers.

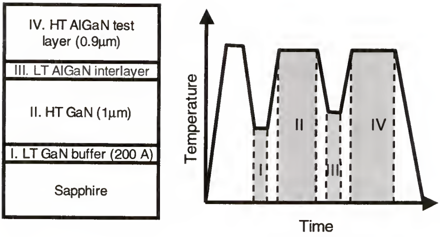

(a) (b)

Figure 4 - 2 (a) Schematic stack structure of the samples in the present work. (b) MOCVD temperature vs. time growth sequence.

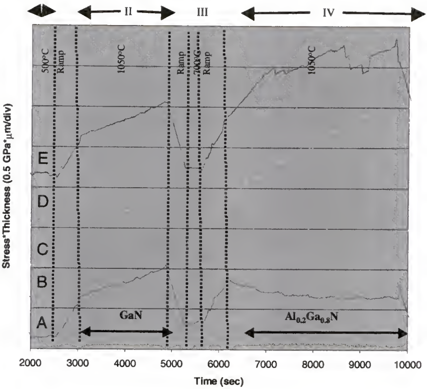

Figure 4 - 3 (stress)*(thickness) versus time during growth of Samples A-E. Dotted lines serve to demarcate the beginning and end of the HT GaN and HT AlGaN growths. (Automatic power control based on the intensity of the reflected beams as feedback was employed during this work. One should focus on the general slopes during HT GaN and HT AlGaN growth and ignore the finer oscillations, which are artifacts possibly due to the power dependence of the laser beam profile.

(a) x_{LT}=0 (b) x_{LT}=0.34 (c) x_{LT}=0.42 (d) x_{LT}=0.62 (e) x_{LT}=1

Figure 4 - 4 Nomarski surface micrograph (~200X) of Samples A-E. (a) x_{LT} = 0.00 (GaN); (b) x_{LT} = 0.34; (c) x_{LT} = 0.42; (d) x_{LT} = 0.62; (e) x_{LT} = 1.00 (AlN).

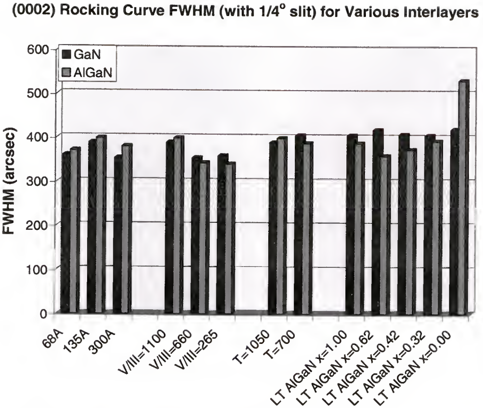

Figure 4 - 5 Effect of changing growth parameters of (Al,Ga)N interlayer on the amount of tilting observed in AlGaN overlayers. GaN layer (0002) linewidth data is also shown for run-to-run sample comparison.

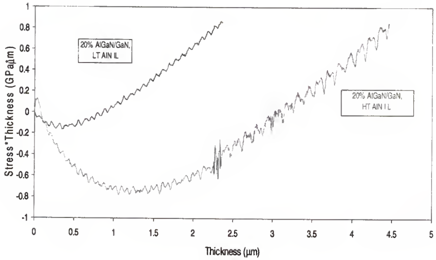

Figure 4 - 6 Dependence of Stress*Thickness vs. thickness curves on growth temperature of AlN interlayer for AlGaN/GaN DBRs.

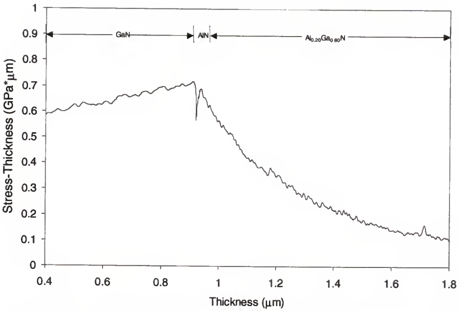

Figure 4 - 7 Stress*thickness vs. thickness for $Al_{0.20}Ga_{0.80}N$/HT-AlN/GaN.

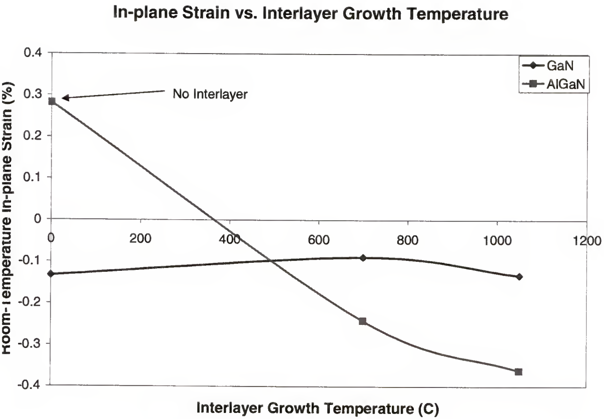

igure 4 – 8 Residual strain as a function of interlayer growth temperature. The data point at "$T_g = 0^oC$" is the residual strain measured from an AlGaN/GaN heterostructure that did not employ any interlayer (sample "C" from Chapter 3) and is shown for comparison. It is not meant to imply that the interlayer was grown at 0°C.

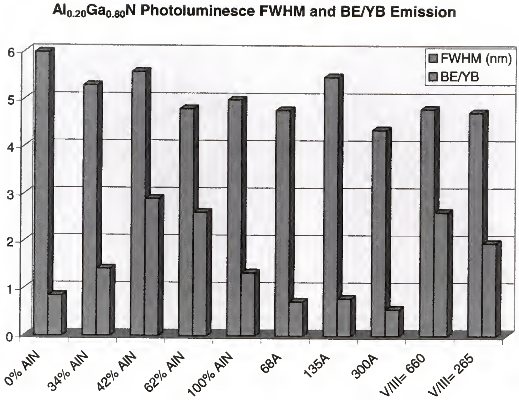

Figure 4 – 9 Effect of interlayer growth conditions on the AlGaN overlayer photoluminescence linewidth and band edge-to-yellow band emission.

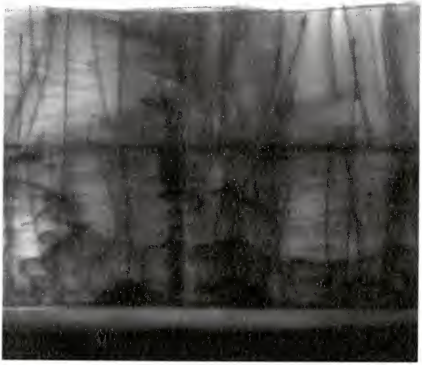

Figure 4 – 10 Cross section TEM bright field image constructed using the (0002) reflection of AlGaN/LT-AlN/GaN sample.

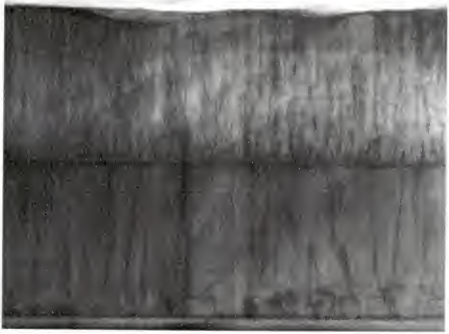

Figure 4 – 11 Cross section TEM micrograph of AlGaN/LT-AlN/GaN sample imaged using the (11$\underline{2}$0) two-beam condition in bright field.

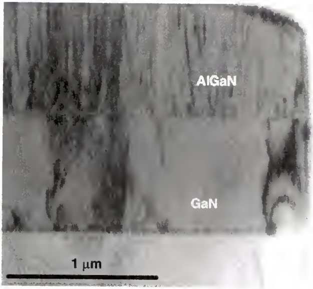

Figure 4 – 12 ($1\underline{1}00$) 2-beam bright field cross section micrograph of AlGaN/HT-AlN/GaN sample.

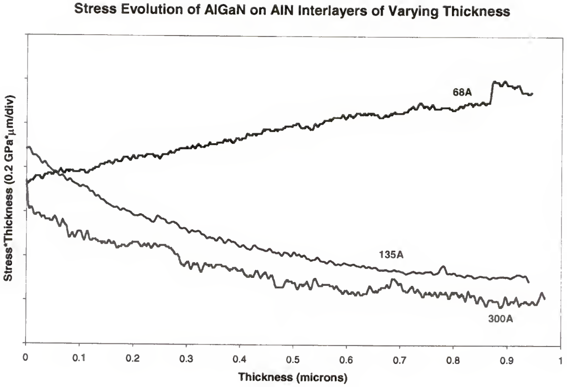

Figure 4 – 13 ***In situ*** **wafer curvature measurement of stress evolution during AlGaN deposition on HT-AlN interlayers of varying thicknesses.**

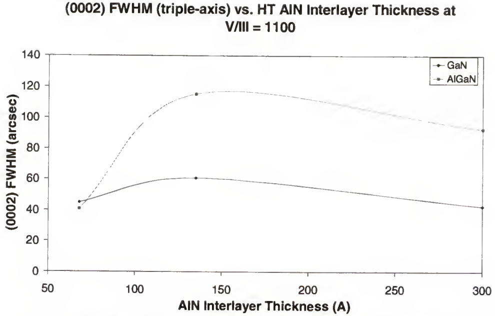

Figure 4 – 13 Radial scan FWHM (strain dispersion data along (0002) of AlGaN and GaN layers (for reference) as a function of HT-AlN interlayer thickness.

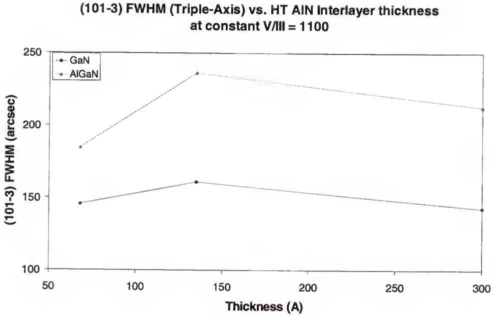

Figure 4 – 15 Radial scan linewidths of the (10$\underline{1}$3) reflection as a function of interlayer thickness.

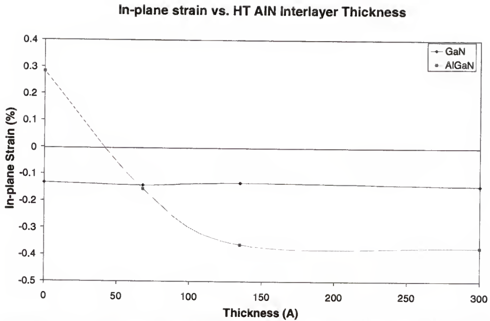

Figure 4 – 16 In-plane (parallel) residual strain as a function of HT-AlN interlayer thickness. The data point at "0C" is sample "C" from Chapter 3 (AlGaN on GaN) without any interlayer.

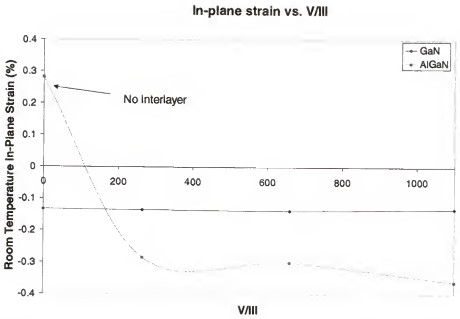

Figure 4 – 17 In-plane residual strain in AlGaN and GaN layers as a function of the V/III ratio employed during growth of the HT-AlN interlayer. All interlayers are 135Å thick.

Table 4 - 1 Results from *in situ* and *ex situ* characterization techniques for LT-AlGaN interlayer experiments.

ple	x_{HT}	$\sigma_{HT\text{-}AlGaN}$ (GPa)	$\varepsilon_{HT\text{-}AlGaN}$ (%)	$a_{HT\text{-}AlGaN}$ $a_{LT\text{-}AlGaN}$(Å)	σ_{GaN} (GPa)	ε_{GaN} (%)	a_{GaN} (Å)	x_{LT}	$a_0(x_{LT})$ (Å)	Fraction of strain relief
	0.201	2.730	0.607	3.1930	0.448	0.100	3.1922	0.00	3.1890	NA
	0.203	1.310	0.291	3.1828	0.393	0.087	3.1918	0.34	3.1631	0.314
	0.201	1.400	0.311	3.1836	0.567	0.126	3.1930	0.42	3.1570	0.262
	0.200	0.501	0.111	3.1773	0.355	0.079	3.1915	0.62	3.1418	0.286
	0.200	-0.746	-0.166	3.1685	0.459	0.102	3.1923	1.00	3.1129	0.299

Table 4 - 2 Griffith critical thickness for fracture as a function of initial stress in $Al_{0.20}Ga_{0.80}N$ on LT-$Al_xGa_{1-x}N$ on GaN.

Sample	x_{LT}	σ_o	h_g
A	0.00	2.730	0.10
B	0.34	1.310	0.43
C	0.42	1.400	0.38
D	0.62	0.501	3.0
E	1.00	-0.746	∞

z

CHAPTER 5
INTERLAYER RELAXATION MECHANISMS

Chapter 3 examined the relaxation mechanisms of thicker layers of $Al_{0.20}Ga_{0.80}N$ on GaN via fracture and subsequent misfit dislocation formation and multiplication. Chapter 4 explored the use of interlayers as a method of relieving strain in AlGaN films grown on GaN, and found that thin layers of AlN inserted between GaN and AlGaN were effective in eliminating cracking in AlGaN overlayers. In situ stress monitoring revealed that the strain state of the AlGaN overlayers was modified by the presence of the interlayer. Via a combination of *in situ* and *ex situ* characterization techniques, it was found that the interlayers partially relax, effectively redefining the in-plane lattice parameter for subsequent layer growth. The present chapter investigates the mechanism(s) by which relaxation of the interlayer takes place. It will be shown that the growth of interlayers on GaN does not proceed by Frank-van der Merwe (layer-by-layer) growth and thus a number of mechanisms for relaxation are possible. Although a brief look at low-temperature deposited interlayers will be presented, the present discussion will focus on the study of AlN interlayers deposited at high temperature, as the complications are minimized by eliminating a low-temperature deposition and subsequent annealing step. Furthermore, of the two possible interfaces to be studied, this discussion will be restricted to the AlN/GaN interface and will not address the AlN/AlGaN interface. Although the study of the growth of the overlayer on top of the interlayer is of interest, it is beyond the scope of the present work.

Morphology of LT-$Al_xGa_{1-x}N$ interlayers

In Chapter 4 it was observed that AlN interlayers deposited at 700°C and annealed at 1050°C prior to AlGaN deposition were relaxed by ~30%. The morphology of AlN layers before and after annealing was examined by repeating the growth sequence of the interlayer samples described in Chapter 4, up through the growth of the interlayer and taking an AFM image of the surface. The wafers were then returned to the growth chamber and were subjected to the temperature ramp conditions normally experienced by the wafer just prior to deposition of the AlGaN. The growth run was aborted before deposition of AlGaN took place. Care was taken to insure minimum air exposure time; however, AFM was performed in atmosphere. No *ex situ* wafer cleaning procedures were followed.

Plan view and 3-D atomic force micrographs of GaN, $Al_{0.42}Ga_{0.58}N$, and AlN interlayers are shown in Figures 5-1(a&b), 5-2(a&b), and 5-3(a&b), respectively. GaN growth at 700°C on GaN appears to grow in a spiral pattern around screw dislocations. The RMS roughness over a $1mm^2$ area is approximately 6Å. The roughness remains comparable for LT-AlGaN films of similar thickness; however, the morphology is dominated by islands with lateral dimensions of approximately 700Å. AlN deposited at 700°C exhibits small, rounded islands that are densely packed and approximately 300Å lateral dimension. The exact shape of the features is difficult to resolve due to the noise level present in the data; it is not clear from the data whether the islands are truly rounded or are faceted and hexagonal in shape.

The morphology of annealed interlayers is shown in Figures 5-4(a&b), 5-5(a&b), and 5-6(a&b), in the same sequence as used for as-deposited films. Annealed LT-GaN closely resembles HT-deposited GaN; the narrow, high "pillars" on the surface of the

GaN are attributed to contaminants on the surface of the wafer prior to annealing. Step-edge features are resolvable between the pillars. Contaminants on the surface of the AlGaN and AlN films may have also altered their appearance under AFM; however, it is less apparent than for the GaN film. Caution should be exercised before drawing any strong conclusions from these data; however, it is apparent that island coalescence has occurred in both cases. The films show similar morphologies of rounded islands and similar RMS roughnesses of 2.3 (AlGaN) and 2.9Å (AlN). The channel morphology present in the as deposited AlGaN film is not present in the annealed film.

It is proposed that the three-dimensional morphology lifts the constraints imposed by the homogeneous biaxial strain field to allow resolved shear stresses on slip systems that would allow the introduction of misfit dislocations in the basal plane at the interface. Save the cross section TEM data presented in Chapter 4, no other data, such as x-ray diffraction data, are available to discern the strain state of the LT interlayers before and after anneal.

In situ Observation of HT-AlN Strain State

In situ curvature evolution data for a GaN/HT-AlN I.L./$Al_{0.20}Ga_{0.80}N$ growth sequence are shown in Figure 4-7. The portion of the data taken during growth of the HT-AlN interlayer (409 seconds) is shown in Figure 5-7. The expected stress for fully strained AlN on GaN at 1050°C is 11.5 GPa. The observed initial slope of 27.7 GPa during the first 54 seconds is an artifact of unknown origin. It is a reproducible phenomenon that has been observed in every AlN interlayer MOSS experiment to date; the range of the slopes is between 16.8 and 27.7 GPa during the first 54-61 seconds of data. Although there is some error in determining the exact point in the data at which the

TMA valve turned on and introduced aluminum into the reactor, this error is expected to be about 10-20 seconds at most, and therefore cannot account for the entire time that this slope is observed. One possible explanation invoked in other materials systems is surface stress. In this case the observed surface stress would be due to the termination of a GaN surface with Al or AlN. However, the stresses observed by MOSS in these data convert to a surface stress of 60 J/m^2, far out of the range of possibility (~2-5 J/m^2). Therefore the observed stress may not be accounted for by surface stress. However, if one assumes that the AlN grows coherently to the GaN for the first two or so monolayers, then a possible explanation is that the growth rate of the AlN is about a factor of 2 to 3 slower than the average during the first minute of growth. The data are plotted assuming a constant growth rate. If the full coherency stress were expected for the first few monolayers, then the initial slope would then be 11.5 GPa, which is roughly a factor of ½ to 1/3 of the observed slope, which could be accounted for by a faulty assumption of the growth rate. After the initial anomaly, the average slope for the balance of the data is 6.14 GPa, which corresponds to a relaxation of 49%, taking into account the strain state of the GaN. This agrees well with the relaxation inferred from the initial slope of the AlGaN overlayer (54%).

High temperature AlN interlayers were grown and observed four other times, all during the deposition of AlGaN/GaN DBRs (see Chapter 6). Two of those four interlayers correspond to nearly identical GaN substrates, and thus the data may be compared directly to examine the reproducibility of the in situ measurement. Figure 5-8 displays the curvature evolution data for these HT AlN interlayers. Note that the absolute value of the stress-thickness has been normalized for comparison. The anomalous tensile stress is present in each set of data. Also present for each layer are oscillations in the curvature data. It is speculated that these oscillations are a result of the fine-scale inspection of the data and are more than likely associated with noise; however, further investigation is required to confirm or refute this hypothesis. It could be possible that the growth rate of AlN is very sensitive to strain in the film, which is evolving with thickness, as discussed below. Nonetheless, confidence may be gained in the measurement from the reproducibility of the data. Table 5-1 lists the measured stress from the slope of the AlN data and the stress inferred from the initial slope of the AlGaN overlayer for all AlN interlayers measured by MOSS to date. It is found that the AlN relaxes approximately 30-50% of the coherency stress in the first 135Å of growth. The run-to-run variation may be due to variations in the stress in the GaN underlayer. The table also demonstrates the reproducibility of the initial slope data for each interlayer.

Possible Relaxation Mechanisms and Experimental Approach

The premise of the AlN interlayer is that the strain in the AlN layer relaxes, thereby redefining the in-plane lattice template for subsequent AlGaN growth. Thus AlGaN overlayers initially grow in a reduced tensile or even compressive strain state whereby cracking may be controlled or eliminated. The remainder of this chapter is dedicated to exploring the mechanisms of relaxation of HT AlN on GaN by directly measuring the strain state *in situ* and comparing it against data acquired *ex situ*.

This section will describe four possible mechanisms for relaxation. The first method is cracking, which is a reasonable possibility since Griffith's formula predicts a fracture critical thickness of 58Å, and the layers used in experiments described here are more than twice that thickness at 135Å. A second method is by the nucleation and glide of misfit dislocations in the basal plane. As discussed in Chapter 3, this is difficult to do unless the homogeneous strain field conditions are lifted. This could take place after cracking has occurred. A third possibility for relaxation is through morphology. The growth of AlN on GaN might proceed via Stranski-Krastanov or Volmer-Weber modes rather than by Frank-van der Merwe growth. The high strain state of AlN tends to favor such behavior. Finally, AlN could expand its lattice and thus relieve tensile strain by incorporating gallium into the lattice. If this mechanism were operative, it would only be expected to occur at regions very close to the interface, as bulk diffusion of Ga in AlN is not expected to be significant.

AlN layers were grown at 40 Torr and 1050°C on 1.0 microns of GaN. Growth conditions were identical to those used in the interlayer experiments. All AlN layers discussed here were bare; no AlGaN was grown on top. The thicknesses of the thin AlN layers were estimated from the growth time by assuming a constant growth rate (0.336Å/s), which was determined by growing a thick layer of AlN and monitoring the thickness using the quarter wavelength interference fringes from 550nm light. The thickness of the growth rate calibration layer was then crosschecked using HRXRD. The morphology of the AlN layers was characterized using AFM. Films were inspected for cracking via optical differential interference contrast (DIC) microscopy. The thickness and strain state of thicker AlN layers were characterized using HRXRD. Initial investigations into the composition of the (nominally pure) AlN layers were performed using SIMS and RBS. The results presented herein will show that a combination of the latter three mechanisms are responsible for the relaxation of the interlayer, while cracking only occurs at thicknesses beyond the range of interest here for interlayers (i.e., greater than 800Å).

HRXRD Investigation of AlN Strain State and Incorporation of Gallium

High resolution x-ray diffraction measurement of the out of plane (0002) and inclined plane (10$\underline{1}$3) lattice parameters yield independent determination of both the strain state and the film composition, assuming accurate knowledge of the elastic constants. Such XRD measurements were performed on AlN film thicknesses of 135, 270, 800, and ~840Å. Results suggest that gallium has incorporated into the AlN film. The parallel and perpendicular strain states could not be resolved without invoking a tetragonal distortion to the lattice consistent with low gallium containing alloys of AlGaN. The gallium concentration vs. AlN film thickness is plotted in Figure 5-9. If gallium were indeed present in the AlN film, this would have major implications for heterostructure device design. One possibility that might account for such a result is the fundamental assumptions of the XRD analysis technique, which require that the strain be in plane, biaxial, and homogeneous, all of which may not be the case in these films, as shown below. Analytical determination of the magnitude of the perturbations necessary to produce such errors is beyond the scope of this work; therefore, a set of experiments was designed to determine whether or not gallium is present in the films, and if so, whether the source of the gallium was from the underlying GaN film or if the source is due to recirculation in the reactor during growth.

Three AlN films of nominally 500Å thick were grown on top of 2 mm GaN under three different conditions. The first (Sample "A") was grown at 1050°C for 1488 seconds, assuming the usual AlN growth rate of 0.336Å/s. The second (Sample "B") was grown at 480°C for 262 seconds, using growth rate data for AlN nucleation layers on sapphire that had been extensively studied previously about two years prior to the present study. This growth was subsequently repeated in the following run (Sample "C"), with the exception that subsequent to AlN deposition, the film was subjected to an *in situ* anneal at 1050°C for 1500 seconds, in order to compare the Ga diffusion profile. If bulk diffusion were the operative mechanism for Ga incorporation in AlN films, samples A and C would be expected to have similar Ga diffusion profiles that would follow Fick's second law. If reactor recirculation or contamination were responsible, all three samples would be expected to have a constant and similar Ga composition throughout the film. The Ga compositions for samples A-C were measured by x-ray diffraction, RBS and SIMS, the results of which are described below.

A major pitfall in the experimental design is the sensitivity of ion-yield techniques such as RBS and SIMS to surface roughness. The morphology of each of the samples A-C is shown in Figures 5-10 through 5-12 (a&b). The samples grew in a 3D mode and contain either open channels or an array of grains. The RMS roughness is between 7 and 20Å. The SIMS profiles are shown in Figure 5-13 (a-c). One striking feature of the data is the thickness of the films, which was determined by using a sputter rate that was calculated by measuring the crater left from sputtering Sample A down to the interface. This sputter rate was applied to samples B and C as well. While SIMS results suggest that Sample A is a factor of two too thick, the results also suggest that Samples B and C are a factor of 5 too thin, or about 200Å. This could be explained simply by the growth rates not being accurate for each temperature. The growth rate of AlN at 1050°C was calibrated on three separate occasions several months apart, and was found to differ only in the third decimal place. However, the growth of AlN is known to be sensitive to temperature; therefore, it is speculated that the temperature of the wafer may have been cooler than expected, perhaps due to poor thermal coupling between the wafer and the susceptor due to particulates on the susceptor surface. Since the temperature is measured by a pyrometer that looks at the susceptor surface, this probably would not have been detected during growth unless it manifested in a slower growth rate of the GaN, which was not observed. During MOSS experiments, wafers have been observed to shift its position in the susceptor pocket during the pressure transition from 140 to 40 Torr. This often posed difficulties in obtaining reliable curvature data on films that had undergone this pressure transition, and data collection became impossible for wafers that did not return to the proper position in time for the experiment to start. Shifted wafers likely experience a greater degree of imperfection in the thermal contact to the susceptor and are thus expected to be at a lower temperature. Data collected by J. R. Creighton of Sandia National Laboratories on a sister reactor to the RDR used in this work indicate that a wafer temperature drop of 70 to 100°C would be required to produce the growth rate changes of factors of 1.5 - 2 observed for Sample A. Although this temperature difference is high, it does not seem to be out of the range of possibility. The thickness discrepancy of Samples B and C is speculated to result from the invalidity of the growth rate data used either due to changing reactor behavior over two years, or due to substrate differences (sapphire vs. GaN).

SIMS results for Sample A data are likely reliable as the sample is thick enough to resolve depth scales reasonably accurately. These results show that the Ga concentration drops to 2% of its value in the GaN over approximately 460Å, indicating that there is a Ga diffusion profile that extends into the AlN film. Sample B grown at 480°C also shows a Ga diffusion profile in the AlN film, but the slope of the Ga concentration near the interface is much steeper than either Sample A or C. The Ga concentration appears to be somewhat higher in the annealed sample.

RBS measurements were performed on samples A-C and a GaN standard with the ion beam at 5, 45, and 60 degrees from normal incidence. Many of the spectra were affected by channeling. Simulations of the spectra indicate that the samples were again measured to be 900, 200, and 200Å thick, in agreement with SIMS measurements. The depth resolution of RBS is expected to be on the order of 100Å. Samples B and C were too thin to make useful determination of Ga composition, while Sample A was determined to have between 5 and 10% Ga uniformly distributed throughout the layer. Although the source of the Ga has not been resolved due to the thinness of the other two layers, all measurement techniques agree that gallium is present in the AlN, and thus lends credibility to the x-ray diffraction data analysis technique employed throughout this work.

X-ray diffraction measurements were only useful for Samples A and C. The average Ga composition was measured to be 4% in both cases. Inclined plane data on Sample B was not accessible with the available instrumentation. The thickness of the sample was determined by measuring the width of the satellite peaks of the (0002) reflection in coupled mode, and was found to be 840Å, in good agreement with RBS measurements.

Morphological Evolution of HT-AlN with Thickness

Figure 5-14 shows the surface morphology of 1 micron of GaN on sapphire with no AlN on top. The surface is characterized by atomic steps bound at the edges by dark spots which are pits attributed to the termination of screw dislocations on the surface of the film. Smaller dots in the micrograph are ascribed to the termination of mixed-character dislocations. Edge dislocations are not visible with AFM. However, AFM is a good method for determining screw and mixed dislocation concentrations in films. The RMS roughness of GaN films grown under these (standard) conditions over a square micron is 1.8 nm.

Figure 5-15 is the surface of GaN after subjection to 30 seconds (~10Å) of AlN. As discussed above, the initial slope of MOSS data for AlN interlayers casts doubt upon the absolute thickness of the layer. However, if a non-uniform growth rate is responsible, there is at least a monolayer of AlN on the surface of the GaN. The surface morphology of this film is markedly different from that of bare gallium nitride. Although atomic step edges are observed (particularly in the upper right hand corner of the micrograph) indicating initial layer-by-layer growth, the film appears to be roughening, as pits and other small, hole-like features are visible. A fine-scale texture not present in plain GaN films is observable after just two monolayers (or less) of AlN.

Figure 5-16 shows the topology of AlN after 90 seconds of growth, which corresponds to a thickness of approximately 35Å. Faceted islands with aspect ratios of 0.04 are clearly visible. The angles between the facets of the islands are all 60 and 120 degrees on average. One possible explanation for this morphology is that the AlN is cracking to relieve excess strain energy. However, the critical thickness for fracture of AlN on GaN, according to Griffith's crack theory, is approximately 62Å. Additionally, crack densities observed in much thicker films are on optical scales, further suggesting that the features are not cracks. Therefore, it is speculated that this morphology arises due to surface transport of chemical species to form three-dimensional islands in a Stranski-Krastanov growth mode. If the thickness is nearly doubled to 68Å (Figure 5-17), the film continues to roughen as the island dimensions refine. The aspect ratio increases to 0.11. The lateral dimensions of islands present in the standard 135Å interlayer (Figure 5-18) have increased in size; furthermore, the aspect ratio has increased to 0.142. Doubling the thickness of AlN again (270Å, Figure 5-19) produces islands that have begun to coalesce; the lateral dimension of the features is about 1250Å. For 800Å of AlN, the film is fully percolated (Figure 5-20). The aspect ratio of these features was estimated in the following manner. The total area of the "holes," or channels, was divided by the total area of the micrograph (1 μm^2) and defined as the width of a sinuous structure. Dividing that value into the film thickness yields the estimated aspect ratio. The aspect ratio for AlN films of 35-800Å is plotted in Figure 5-21. As expected, the aspect ratio increases with film thickness.

The relaxation of the AlGaN from crude morphological considerations is estimated in the following manner. Islands are assumed to be one-dimensional and are allowed to relax in on the sides. Islands are allowed to relax 1.5 film thicknesses (h) from the sides; the remaining area is assumed to be fully strained. The amount of relaxation in non-percolated films due to morphology is estimated by summing the total area of relaxed material and dividing by the total area. For percolated structures, a unilateral relaxation approximation approach was used that involved the weighted average of an array of relaxed and strained wires. Figure 5-22 plots the relaxation estimated from morphology against the AlN film thickness. As expected, the morphological relaxation goes through a maximum near percolation, whereupon adding more material to the film must cause the film to restrain. The relaxation has also been converted to a relative parallel strain state by multiplying by the total strain between the AlGaN composition determined by x-rays and GaN in order to compare the morphological relaxation of samples independently of film composition. The normalized parallel strain state as determined by AFM and by HRXRD is plotted against the aspect ratio as in the manner just described for samples of 270Å or thicker in Figure 5-23. Misfit dislocation content is expected to balance out the difference in strain state as determined by morphology and that measured by x-ray diffraction. This strain difference is plotted in Figure 5-24. Verification of this result by plan view TEM is in progress for select samples but no data are available at the time of writing.

King et al.[48] investigated the growth mode of (0001) AlN on GaN and GaN on AlN by MBE in situ using x-ray photoelectron spectroscopy. They found that growth of GaN on AlN transitions from 2-D to 3-D (Stranski-Krastanov) at about 3 monolayers of GaN at low temperatures (650-750°C), while AlN growth on GaN was layer-by-layer for growth temperatures from 750-900°C out to 40Å.

Effect of V/III Ratio on the Growth of AlN

Keller et al. have observed a pronounced effect of V/III ratio on the growth mode of AlGaN on GaN for use in HEMTs.[49,50] Their work was aimed at optimizing the growth of high composition AlGaN (x>0.25) to promote better performance of electronic devices that rely heavily upon the quality of the AlGaN/GaN interface. They were able to grow $Al_{0.38}Ga_{0.62}N$ pseudomorphically up to 650Å. Thus it is clear that strain is not the sole factor in controlling morphology of AlGaN films and that growth kinetics play a role. Figure 5-25(a, b, &c) shows the surface morphology of 135Å of AlN on GaN at three different V/III ratios. The alkyl flow was kept constant. The growth rates were determined by calibration of a thicker layer in the prior run and assuming constant growth rate with time.

The morphology does not change monotonically with V/III ratio, but rather achieves a minimum in three-dimensionality at the midrange of the conditions explored in this study. The aspect ratio vs. V/III ratio is plotted in Figure 5-26. X-ray diffraction was not performed on the two lower V/III ratio films. Plan view TEM analysis is a subject of future work.

Discussion

The morphology and growth mode of (Al,Ga)N on GaN appear to play a major role in the amount of relaxation of the film. The morphology is affected by the growth temperature, composition, thickness, and V/III ratio. The energetics of the morphological evolution of AlN films is dominated by at least five competing mechanisms. First is the strain energy, which drives the film to relax by either geometrically relieving strain by increasing the aspect ratio of the features. Once three dimensional features have formed, inhomogeneous, non-biaxial strain fields are present which produce non-zero resolved shear stresses on active slip systems in the AlN and thus allow the introduction of misfit dislocations at the AlN/GaN interface. Stacking faults produced during growth may also act to relieve strain energy.[27] Strain-relieving defects at the interface reduce the driving force for increasing the aspect ratio of the features. Competing directly against the aspect ratio is the cost in surface energy, the reduction of which favors larger island sizes—or at the extreme, planar growth. Further complicating the picture is the growth kinetics, which depends on the V/III ratio regime present during growth. Lower V/III ratios appear to favor increased metallic adatom mobility; however, there is an optimum regime beyond which the growth of AlN may be disrupted due to excessive point defects. Further study is required to confirm or refute this speculation, however. Finally, gallium incorporation has been observed in thin AlN films grown on GaN. As noted above, the source of the Ga has not yet conclusively been determined. Gallium incorporating on an Al site would effectively expand the lattice, thereby reducing the tensile strain. Gallium may also incorporate via diffusion along threading or screw dislocations, which would also tend to expand the lattice to reduce strain. Yet a third possibility is that Ga segregates due to a mismatch in surface energy between GaN and AlN. This has been observed in the case of germanium in SiGe. Finally, the presence of gallium in AlN in this study may eventually be traced back to contaminants or recirculation in the reactor. Clearly, there are many interwoven mechanisms that are operative in this system.

Under the standard HT-AlN interlayer conditions employed in producing the DBRs and VCSELs discussed in the following chapter (Tg = 1050°C, V/III = 1100), AlN growth appears to occur via a Stranski-Krastanov growth mode. Interrupted growth studies reveal that layer-by-layer growth is operative for the first 2-3 monolayers, after which an islanded growth mode is favored. At thicknesses less than half of the critical thickness for fracture as predicted by Griffith's theory, faceted grains with very low aspect ratio are visible. It is speculated that the facets are low energy surfaces with low Miller indices (e.g., $10\underline{1}0$, $11\underline{2}0$). The morphological evolution during subsequent growth is carried out on a playing field on which strain energy due to lattice mismatch, surface energy, misfit dislocations, chemical diffusion, adatom mobilities, and reaction kinetics all compete to produce a morphology with the lowest energy. Intermediate values of V/III ratios appear to allow higher surface mobility of the metallic species, which in turn allows higher planarity of the growth; however, at very low V/III ratios islanding is again more favorable. Further study is required to understand the interplay between growth kinetics and strain in producing a favored morphology.

Summary

Initial studies suggest that MOVPE growth of AlN on GaN proceeds via a Stranski-Krastanov growth mode, with the transition occurring between 1 and 7 monolayers. The aspect ratio of the island sizes is found to increase with increasing film thickness, which allows relaxation of strain through geometrical arguments. Inhomogeneous, non-planar strains resulting from the three dimensional morphology would allow misfit dislocation nucleation and glide to the AlN/GaN interface, which are believed to be the source of threading dislocations observed in AlGaN overlayers on AlN interlayers; however, study of the AlN/AlGaN interface is required to be certain. Gallium is found to incorporate in AlN layers grown on GaN; however its source remains unclear. The morphology is also affected by the V/III ratio during growth. Although planar growth of AlN was not achieved in the studied range, fully percolated AlN was produced at an intermediate value of V/III. Lower values tended to favor more discrete islands. Although data on this portion of the study are limited, it is speculated that increased aluminum mobility is responsible for the percolation, but this effect tends to saturate near the midrange value explored in this study.

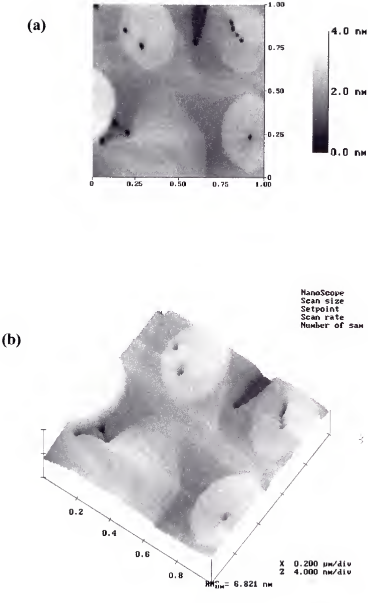

Figure 5- 1. (a) Plan view AFM of 125Å GaN on GaN deposited at 700°C; (b) 3-D view.

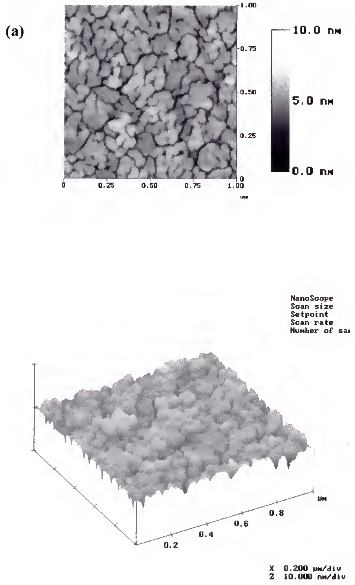

Figure 5- 2 (a) Plan view and (b) 3-D view of AFM image of surface of LT-AlGaN interlayer.

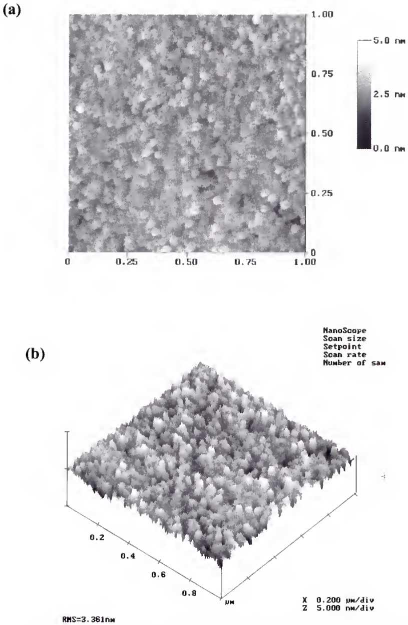

Figure 5- 3 Plan view (a) and 3-D (b) images of the surface of LT-AlN interlayer.

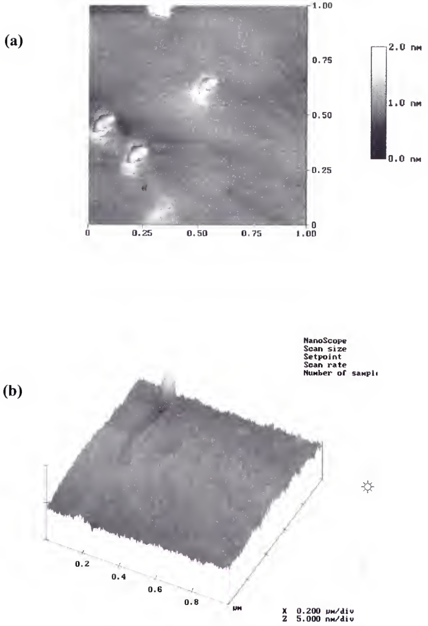

Figure 5- 4 Plan view (a) and 3-D (b) images of annealed LT-GaN interlayer.

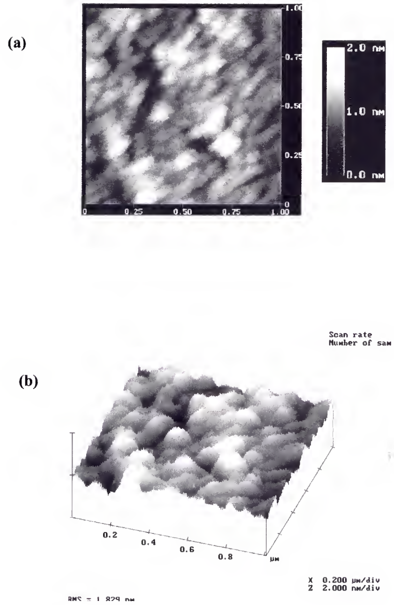

Figure 5- 5 Plan view (a) and 3-D (b) views of AFM images of surface of annealed LT-AlGaN interlayers.

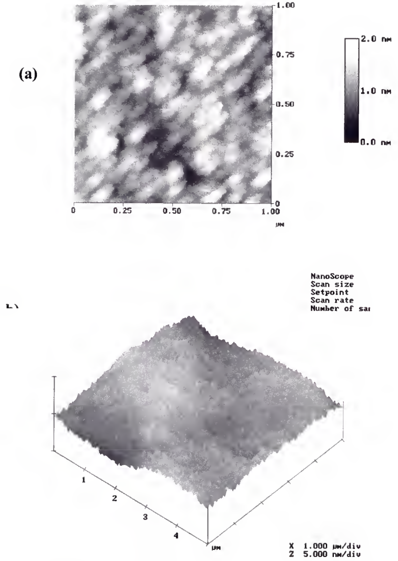

Figure 5- 6 Plan view (a) and 3-D (b) AFM images of surface of annealed LT-AlN interlayer.

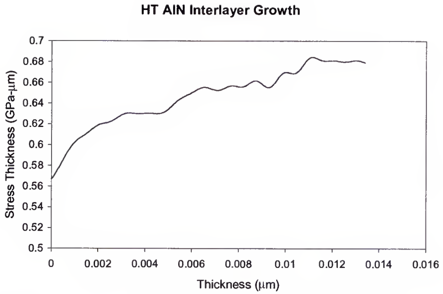

Figure 5- 7 *In situ* wafer curvature data for 135Å HT-AlN interlayer.

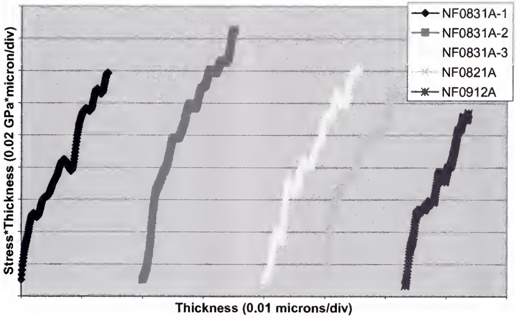

Figure 5- 8 MOSS data for several interlayers.

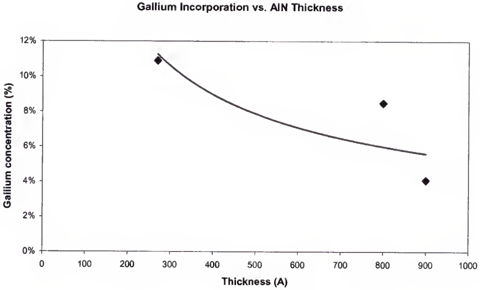

Figure 5- 9 X-ray diffraction data showing gallium incorporation in AlN as a function of layer thickness.

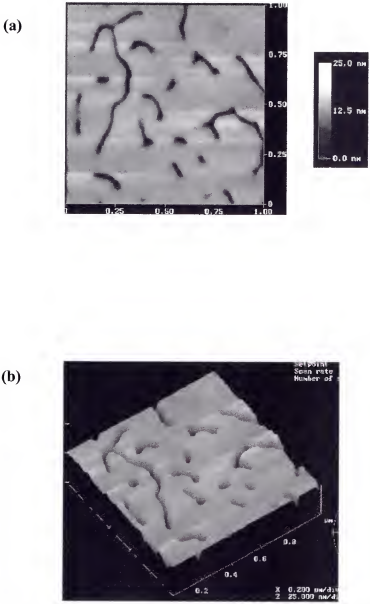

Figure 5- 10 Plan view (a) and 3-D (b) AFM images of the surface of Sample A (AlN grown at 1050°C) in the Ga diffusion experiment.

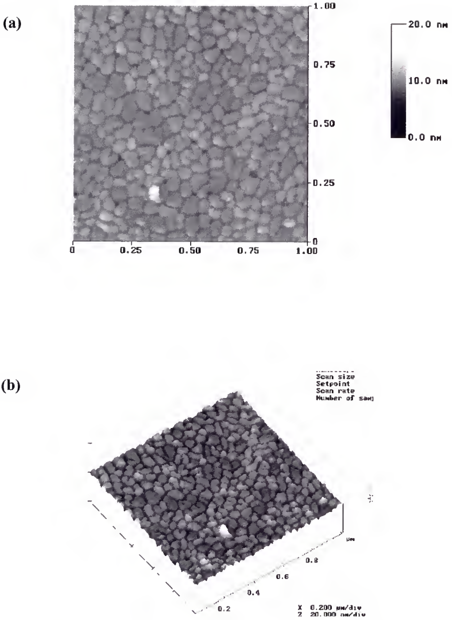

Figure 5- 11 Plan view (a) and 3-D (b) AFM images of surface of AlN deposited at 480C.

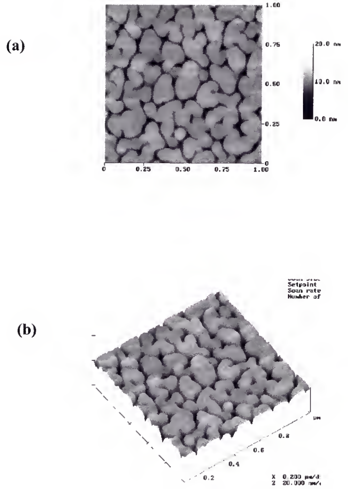

Figure 5- 12 Plan view (a) and 3-D (b) AFM images of surface of AlN deposited at 480°C and annealed at 1050°C for 1500 seconds.

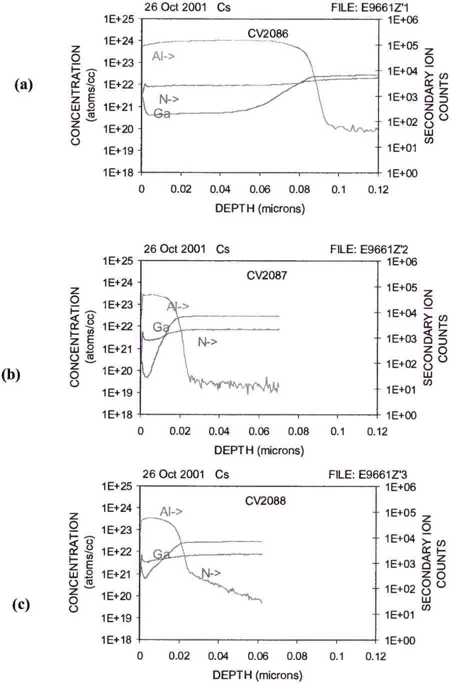

Figure 5- 13 SIMS depth profiles of (a) Sample A, (b) Sample B, and (c) Sample C.

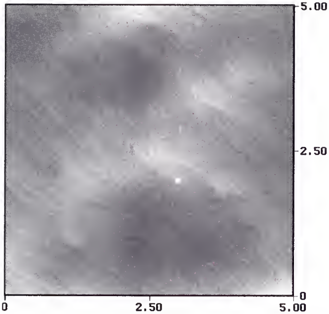

Figure 5- 14 Plan view AFM image (5μm x 5 μm) of the surface of GaN.

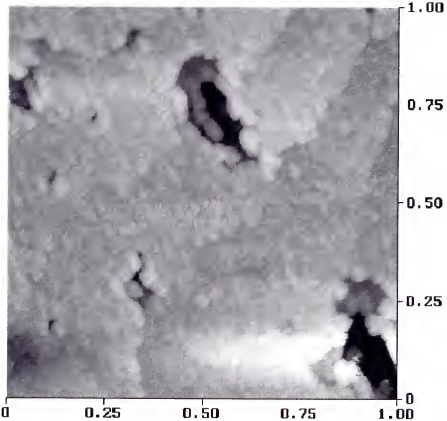

Figure 5- 15 Plan view AFM image of the surface of AlN/GaN after 30 seconds (nominally 10Å) of AlN deposition at 1050°C.

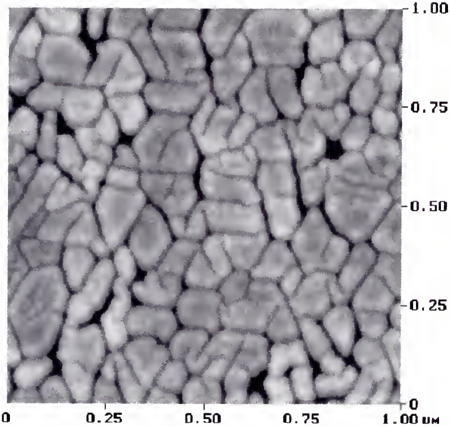

Figure 5- 16 Plan view AFM image of surface of AlN/GaN after nominally 35Å AlN deposition at 1050°C.

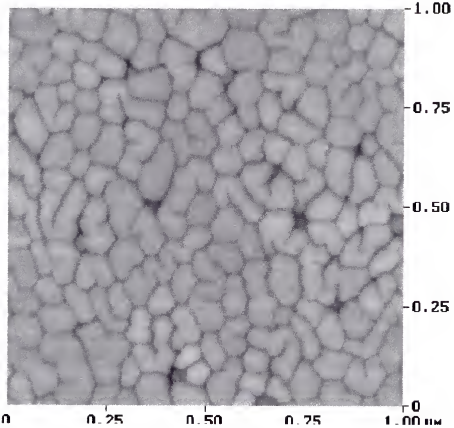

Figure 5- 17 Plan view AFM image of surface of AlN/GaN after nominally 68Å AlN deposition.

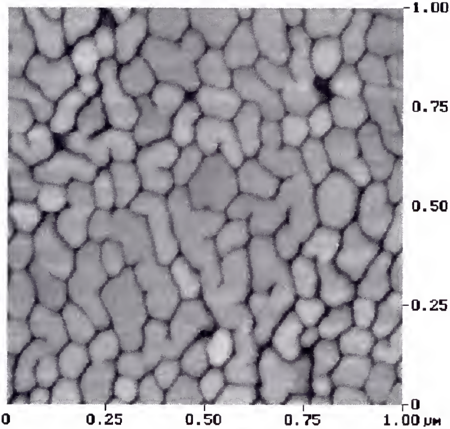

Figure 5- 18 Plan view AFM image of 135Å AlN on GaN deposited at 1050°C. This is the morphology of the standard AlN interlayer employed throughout this work.

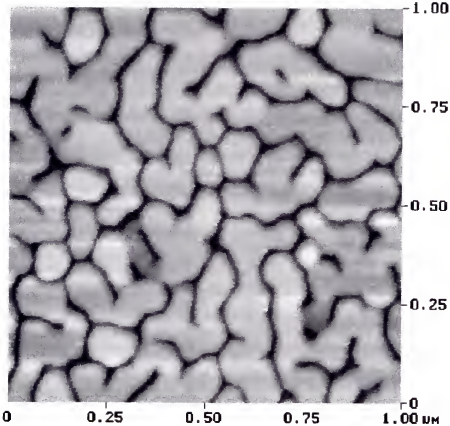

Figure 5- 19 Plan view AFM image of ~300Å AlN on GaN.

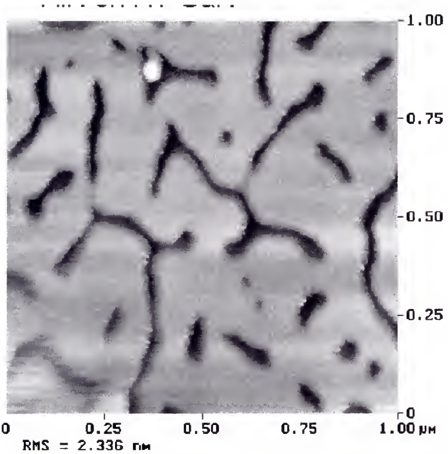

Figure 5- 20 Plan view AFM image of surface of 800Å AlN on GaN. Even at this thickness, the film is not fully continuous; however, it is fully percolated.

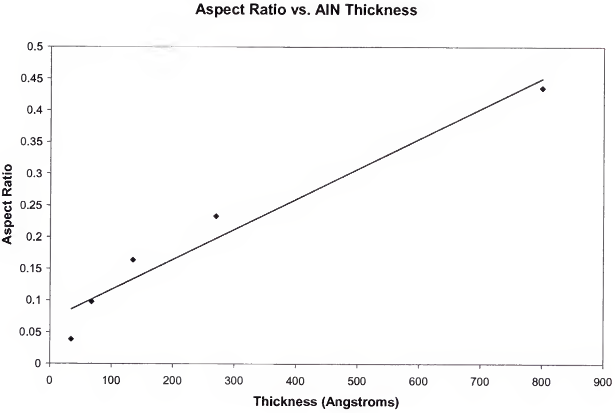

Figure 5- 21 Aspect ratio vs. AlN film thickness.

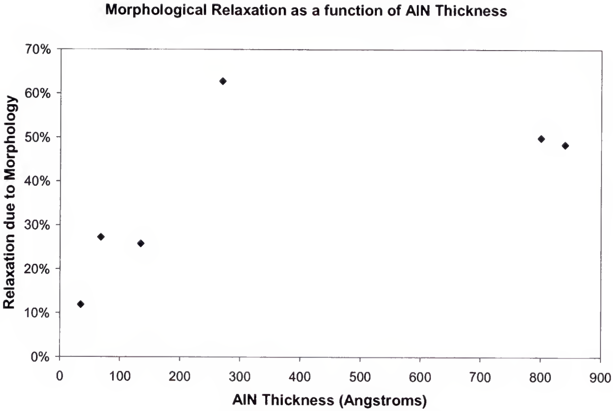

Figure 5- 22 Relaxation expected due to morphology (aspect ratio) vs. AlN film thickness.

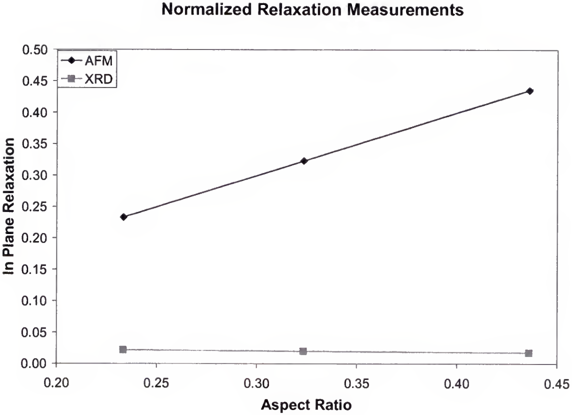

Figure 5- 23 Parallel strain state of AlN on GaN as measured by AFM HRXRD as a function of island aspect ratio.

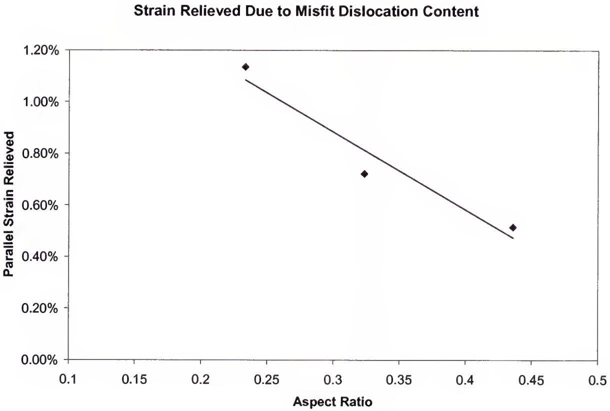

Figure 5- 24 Parallel strain state expected to be relieved by misfit dislocations as a function of aspect ratio.

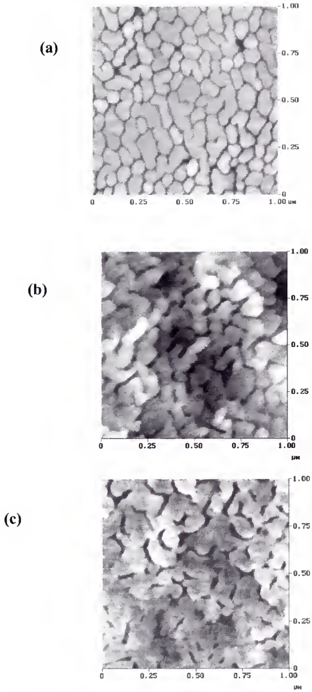

Figure 5- 25 Plan view AFM images of the surface of 135Å AlN grown on GaN at V/III = (a) 1100; (b) 660; and (c) 265.

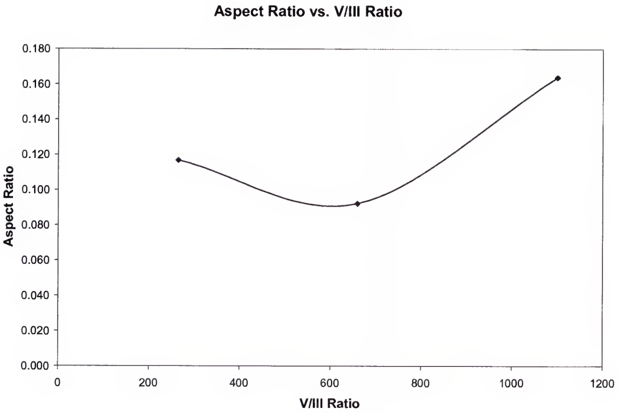

Figure 5- 26 Aspect ratio of island size of 135Å AlN as a function of V/III ratio.

Table 5- 1 ***In situ*** **curvature measurement results from various HT AlN interlayers.**

Sample Description	Initial Slope (GPa)	Seconds of data for initial slope	Directly Measured Stress of AlN (GPa)	Relaxa-tion of AlN	Initial stress in AlGaN overlayer (GPa)	Relaxation of AlN inferred from AlGaN
Monolithic AlGaN overlayer on AlN interlayer on GaN	27.7	54	6.14	49%	-5.00	54%
AlGaN/GaN DBR on GaN with HT AlN interlayer	22.9	58	7.91	31%	-3.33	36%
First of three HT AlN interlayers in AlGaN/GaN DBR on GaN	21.5	55	7.73	33%	-3.31	36%
Second of three HT AlN interlayers in AlGaN/GaN DBR on GaN	27.7	66	7.00	39%	-2.54	28%
Third of three HT AlN interlayers in AlGaN/GaN DBR on GaN	16.8	61	7.5	35%	-2.53	28%

CHAPTER 6
DEVICES USING AlN INTERLAYERS

Introduction

Optical, optoelectronic, and electronic devices based on AlGaN/GaN heterostructures are desired due to their accessibility of the ultraviolet region of the electromagnetic spectrum and their potential for use in high frequency, high temperature electronic components. Due to the large tensile mismatch between AlN and GaN, cracking occurs in ternary alloy layers grown epitaxially on GaN, which has severe deleterious consequences for device performance. In this chapter, the growth and processing of three devices based on AlGaN/GaN heterostructures by incorporating stress-relieving AlN interlayers is described: a highly reflective, crack-free AlGaN/GaN DBR with a reflectivity stopband centered around 384 nm; a room-temperature, optically-pumped near ultraviolet vertical cavity surface emitting laser (VCSEL), which, to the best of our knowledge is the first time this has been accomplished using an epitaxial bottom mirror; and an electrically pumped resonant cavity light emitting diode with a dominant emission mode at ~413nm using an intracavity lateral current spreading layer based on a p++/n++ InGaN/GaN tunnel junction.

A schematic of a VCSEL is shown in Figure 6-1. The critical parameters that must be controlled in order to achieve successful VCSEL operation are as follows. First, the optical (gain) spectrum must be tailored for the specific laser design, which entails controlling both the composition and the thickness of the multiple quantum wells and barriers. Second, the reflectivity stopband of the top and bottom distributed Bragg mirrors must be controlled to provide >99% reflectance at the optical wavelength in the medium of the gain spectrum. This is generally the most difficult task in building a VCSEL, as the thickness and composition (i.e., the growth temperature) of the quarter-wavelength layers must be accurately controlled over a long growth period, as many layers are required. Third, the length of the Fabry-Perot microcavity must be accurately controlled to provide resonance and thus gain for the operation of the laser.

The author acknowledges that the work in this chapter was performed collaboratively with Professor Arto Nurmikko's group at Brown University in Providence, Rhode Island. The work at Brown University was supported by the National Science Foundation, the Defense Research Projects Agency, and by a grant from Lumileds Lighting LLC.

MOVPE Growth of Highly Reflective Near UV Distributed Bragg Reflectors

The growth of epitaxial distributed Bragg reflectors (DBRs) with high crystalline quality is one of the key factors underpinning the success of infrared and red vertical-cavity surface-emitting lasers (VCSELs).[51] The development of III-Nitride-based VCSEL for short-wavelength (visible and ultraviolet) applications has been met with numerous challenges, among which the preparation of crack-free, highly reflective (Al,Ga)N/GaN DBRs appears to be the most difficult owing to the large lattice mismatch between GaN and AlN (2.5%). Since multiple passes of optical waves are required in VCSELs due to a short cavity (gain) length, highly reflective mirrors (typically R>99%) are required for low threshold operation. The low contrast in index of refraction between

AlN and GaN (and thus the ternary alloys) necessitates the use of a large number of pairs of mirrors to achieve such reflectivities. Someya and Arakawa reported the crack-free growth of a 35-pair Al0.34Ga0.66N/GaN DBR with reflectivity up to 96% at 390nm.[52] It was emphasized in that work that the thickness of the (high temperature-grown) GaN layer must be restricted to 0.4 μm or less to avoid sample cracking. Langer et al.[53] reported a maximum reflectivity of 93% at 473nm with 30 pairs of $Al_{0.41}Ga_{0.59}N$/GaN DBRs. Krestnikov et al.[54] employed a 1.1 μm $Al_{0.08}Ga_{0.92}N$ template on sapphire for stress compensation and showed a reflectivity of 96% at 401nm with 37 pairs of $Al_{0.15}Ga_{0.85}N$/GaN DBR mirrors. Very recently, Ng et al.[55] explored DBR mirrors consisting of binary AlN and GaN for increased contrast in the index of refraction. They reported 99% reflectivity at 467nm with one specific structure that employed approximately 20 to 25 pairs of DBR mirrors. A network of cracks was observed which was attributed to the large tensile stress between the two binary compounds.

As discussed in Chapter 4, the use of AlGaN interlayers is effective in controlling mismatch-induced stress and suppressing the formation of cracks otherwise occurred during growth of AlGaN directly upon GaN epilayers. This section describes the *in situ* monitoring and control of stress evolution during OMVPE growth of AlGaN/GaN DBR mirrors. It is demonstrated that the employment of an AlN interlayer at the beginning of a thick (~5 μm) DBR growth leads to a substantial modification of the initial stress evolution. Tensile growth stress can be brought under control and nearly eliminated, as confirmed by an *in situ* stress sensor, through multiple insertions of AlN interlayers. Using this technique, crack-free growth of 60 pairs of $Al_{0.20}Ga_{0.80}N$/GaN DBR mirrors has been achieved over the entire two-inch wafer with a maximum reflectivity of at least 99%.

Metal-organic vapor phase epitaxy was conducted in the custom vertical rotating-disc reactor described in Chapter 2. Standard 1 µm-thick GaN templates were prepared using the standard two-step nucleation procedure on sapphire, also described in Chapter 2. The AlGaN/GaN quarter-wavelength DBRs and the interlayers were grown at 40 Torr and 1050°C. Ammonia and H_2 flows were set at 2.5 and 5 *l*/min, respectively. Trimethylgallium (TMG) and trimethylaluminum (TMA) were employed as metal-organic precursors. Growth rates of the AlGaN and GaN layers were calibrated in situ using optical reflectometry (from the period of the Fabry-Perot interference fringes) immediately prior to the growth of DBRs.

High-resolution x-ray diffractometry (HRXRD) was performed using a Philips X'Pert System[56] with Cu Ka radiation (1.54056 Å). Real time *in situ* stress monitoring based on wafer curvature measurements was performed with a multi-beam optical stress sensor (MOSS)[57] modified for use on our reactor and described in Chapter 2.

Figure 6-2 shows the *in situ* stress-thickness curve recorded by MOSS of a DBR structure consisting of 30 pairs of $Al_{0.20}Ga_{0.80}N$/GaN layers, approximately 400 Å thick each. The DBR structure is grown directly atop the 1-µm thick GaN layer with no interlayers. Only the AlGaN/GaN DBR sections of the MOSS data are displayed in the following MOSS figures shown in this chapter. The quarter-wavelength AlGaN/GaN DBR as a whole acts as a pseudo-alloy in terms of inducing an accumulation of tensile stress energy. A growth tensile stress of 1.24 GPa is derived during the DBR growth, which corresponds to the elastic mismatch between GaN and $Al_{0.11}Ga_{0.89}N$, in good agreement with the average composition of the DBR layers. One also notices a fine, saw-tooth pattern that fluctuates around the rising, background straight line. The stress fluctuation corresponds to the alternation of instantaneous growth stress during growth of the quarter-wavelength GaN layers that are in compression (indicated by negative slopes) and AlGaN layers that are in tension (indicated by positive slopes). The average value of the saw-tooth slope changes is 2.49 ± 0.4 GPa, which agrees reasonably well with the expected value of 2.33 GPa based on the elastic mismatch between GaN and $Al_{0.20}Ga_{0.80}N$.[27] Step-like reductions in the stress-thickness trace observed at 1.35 μm and at 2.33 μm indicate the relief of tensile stress through crack propagation and admission of dislocations, similar to those described in Chapter 3. Inspection of the surface of this DBR under Nomarski microscope (Figure 6-2 inset) confirmed the presence of cracking networks, with an average spacing below 100 μm.

In order to mitigate the mismatch-induced tensile growth stress and avoid cracking, an AlN interlayer (nominally 150-Å thick) was inserted between the HT GaN layer and the 30-pair DBR structure. Figure 6-3 shows the in situ MOSS data. Similar to the findings described in Chapter 4, the use of an AlN interlayer reduces the in-plane lattice constant and consequently exerts a compressive stress during the initial growth of AlGaN/GaN DBR structures. The observed compressive stress gradually decreases and passes through a stress-free region at around 0.5 mm; a constant tensile stress (~0.62 GPa) is developed and sustained throughout the rest of the DBR growth. The exact origin of the observed stress evolution from compression to tension remains unclear; mechanisms such as grain growth and thin film densification have been invoked in other material systems to explain such a spontaneous occurrence of the tensile stress. In this particular case, the employment of an AlN interlayer delays the occurrence of a tensile stress, reduces the steady-state growth tension, and effectively doubles the critical thickness for cracking. The surface morphology was found to be crack-free over the entire 2" wafer (Figure 6-3 inset). The peak reflectivity, however, only reaches about 78% with a bandwidth of around 12 nm, as shown in Figure 6-4.

In applying these results to the design and fabrication of an AlGaN/GaN multilayer DBR structure suitable for use in vertical microcavities, modeling based on wave propagation across multiple mediums using the transmission matrix method was performed. The results shown in Figure 6-5 suggest that 50 to 70 pairs of mirrors are required for a reflectivity exceeding 99% with the use of $Al_{0.20}Ga_{0.80}N$/GaN, due to the small difference in refractive index (Δn~0.08). Another DBR growth was subsequently performed in which the number of pairs was increased to 60 and the same structure was grown on a 150-Å AlN interlayer. It was found during this work that AlN interlayers grown at high temperature (i.e., 1050°C) were even more effective in controlling stress in the DBRs than those deposited at low temperature (700°C). It is for this reason that the rest of the work in this dissertation will focus on AlN deposited at 1050°C unless otherwise noted. *In situ* MOSS data during the DBR growth are shown in Figure 6-6. Again, the saw-tooth-like fluctuations in (stress)*(thickness) resulting from the growth of the alternating DBR layers are superimposed upon the "background evolution" from compression to tension. The observed growth tension (0.58 GPa) implies a cracking critical thickness of 2 μm from general fracture mechanics, which is less than half of the total thickness. We note that the surface of this sample, which has a total thickness of 5.7 μm (4.7 μm from the DBR and 1.0 μm from the GaN underlying layer), exhibited a low density of cracks with an average spacing varying from 0.5 mm (near the center) to 50 μm (near the edge) of the 2" wafer, as shown in the inset of Figure 6-6. *In situ* stress measurement indicates that it is the accumulation of the background, "dc" tensile stress energy, not the alternating stress fluctuation between the AlGaN and GaN layers, which caused the occurrence of cracking. The corresponding reflectivity spectrum is shown in Figure 6-7 with a peak reflectivity (λ~378 nm) measured at around 99.1% by a precision reflectometer against a calibrated standard. By varying the individual DBR layer thickness, similar mirrors have been obtained (R~0.99) with a peak wavelength ranging from 375 to 420 nm. High-resolution x-ray diffraction (2θ-ω) scan along the (0002) diffraction shows the presence of satellite diffraction peaks up to the 13th order (Figure 6-8). The cross-section transmission electron micrographs shown in Figure 6-9 of the structure taken near the GaN pseudosubstrate and near the Fabry-Perot microcavity demonstrate a dislocation density at or near $\sim 1\text{x}10^{8}\text{cm}^{-3}$. Dr. S.N.G. Chu at Lucent Technologies performed the XTEM analysis.

It was speculated that the persistent, tensile growth stress observed during the DBR growth, presently of unknown origin, could be partially reset by the introduction of additional AlN interlayers at various stages. One should note that LT-GaN and AlN multiple-interlayer schemes have been proposed by Amano et al.[21] for the purpose of dislocation filtering. However, Benamara et al. found[58] that the use of AlN multiple interlayers tended to increase the density of edge-type dislocations through dislocation multiplication. To test our hypothesis, a 60-pair $Al_{0.20}Ga_{0.80}N$/GaN DBR structure was grown in which an AlN interlayer was inserted after every growth of 20 pairs. (A total of three AlN interlayers was employed.) The *in situ* stress-thickness vs. thickness of the multiple-interlayer DBR is presented in Figure 6-10. Once again, the saw-tooth-like features of alternating stress are observed due to the elastic strain between GaN and AlGaN layers. Nevertheless, a distinct "drape-like" stress evolution is observed in which the instantaneous growth stress was substantially modified after each introduction of the AlN interlayer. For this particular sample, a compressive stress of 2.3 GPa is introduced after every AlN interlayer (shown in arrows). Tensile stress was not observed during any of the 5-μm DBR region, in contrast to the samples with no or only one AlN interlayer. HRXRD was employed to assess the structural quality of the 60-pair DBR with multiple interlayers, and is shown in the lower trace of Figure 6-8. When compared with the upper trace of Figure 6-8, it appears that the introduction of the AlN interlayers does not significantly change the microstructural quality. No cracks were observed under Nomarski microscope (50 to 500 times magnification) over the entire two-inch wafer (approximately 5.7 mm-thick film), and the peak of reflectivity remains above 99%, with a bandwidth of 13 nm. Substrate considerations prevented reflectivity measurement to a higher degree of precision above 99%.

In conclusion, the feasibility of stress engineering has been demonstrated and confirmed through a combination of *in situ* stress monitoring and the employment of AlN interlayers during growth of AlGaN/GaN DBRs.

MOVPE Growth and Processing of a Room-Temperature, Optically Pumped Ultraviolet VCSEL

One current challenge for III-nitride based lasers is the extension to the near ultraviolet (NUV) regime below 400 nm. Application areas, including chemical and biological sensing, would benefit from compact NUV coherent light sources. In parallel, there are early precursors for nitride lasers in vertical cavity, surface-emitting geometry in the blue. Stimulated surface emission,[54,59] including VCSEL operation with well-defined far field patterns,[60] has been observed in optically pumped structures that feature specific fabrication paths to low-loss vertical microresonators.

In this section, this experience is drawn upon to demonstrate quasi-continuous wave (cw) operation, at room temperature, of an optically pumped $In_xGa_{1-x}N$ ($x\sim0.03$) MQW VCSEL at λ=383 nm. The vertical cavity scheme employed combines a high reflectivity *in situ* grown multilayer $GaN/Al_{0.20}Ga_{0.80}N$ and post-growth dielectric SiO_2/HfO_2 distributed Bragg reflector (DBR). The *in situ* grown nitride DBR used is the one described in the previous section that includes a single AlN strain compensating interlayer within the multilayer stack, which serves to eliminate tension-induced cracking usually encountered during growth of AlGaN/GaN heterostructures on GaN. The presence of cracks, which propagate along well-defined crystallographic planes is a major impediment in a nitride VCSEL since they form 'accidental' resonators which greatly enhance the onset of lateral stimulated emission along the heterostructure layer plane, disabling true VCSEL operation. In this work, R»0.99 has been reached, an adequate value compensated by the top dielectric DBRs (R=0.995) in these 'hybrid' microresonators. This is a result of the very low crack density observed in the DBR using a HT AlN interlayer.

The active region was grown directly atop the GaN/(Al,GaN) DBR with three AlN interlayers described in the preceding section and was composed of 20 $In_{0.03}Ga_{0.97}N$ quantum wells (L_w=40 Å) with GaN barriers (L_B=60 Å). The as-grown DBR and the QW indium concentration were designed for spectral overlap between the high reflectivity region of the former with the photoluminescence emission of the latter. The structure was capped by a 1000 Å thick $Al_{0.1}Ga_{0.9}N$ carrier confinement layer. The room temperature photoluminescence of the active region is displayed in Figure 6-12 and demonstrates the existence of cavity modes provided by the high reflectivity bottom mirror (R>99%) and the poor reflectivity top interface (i.e., air; R~17%). Finally, a multilayer l/4 stack of SiO_2/HfO_2 was deposited by reactive ion beam sputtering. HfO_2 is a high index, low absorption material in the NUV (to below 300nm), with high quality crystal microstructure. The broad reflection bandwidth (~80nm) of the dielectric DBR was tailored to overlap the near band edge InGaN emission. The growth of the nitride heterostructure was optimized for high optical flatness as good morphology is crucial to the realization of true VCSEL operation. The optical interferogram of the DBR surface shown in Figure 6-11 demonstrates a RMS surface roughness of approximately 4.5nm over a 1mm x 1mm area. AFM studies of the surface of the as-grown wafer and the complete microcavity indicated a mean roughness of approximately 2 nm over areas on the order of several hundred square microns.

The vertical cavity structures were optically pumped by a frequency tripled, continuous-wave (cw) modelocked Nd:YAG laser at 355 nm, operating at a repetition rate of 76 MHz. The stack structure and the geometry of the optical characterization of the completed devices are shown in Figure 6-13. The individual pulse duration was approximately 0.1 nsec and the radiation was focused at near normal incidence to a ~20 mm diameter spot. The high repetition rate pumping is referred to as quasi-cw, as used in the literature. The wavelength of excitation laid outside the reflectance band of the top dielectric DBRs and slightly below the bandgap of the top AlGaN confinement layer, ensuring a creation of electron-hole pairs directly into the InGaN QWs. Given the thickness of the InGaN MQW (800 Å), only a fraction of the pump photons (estimated less than 25%) were usefully absorbed. Figure 6-14 shows the room temperature spontaneous emission spectrum at an average incident power of approximately 14 mW. Two well defined cavity modes are seen, while a third lies at the rapidly falling edge of reflectivity band of the GaN/(Al,Ga)N bottom DBR, and is thus strongly broadened. Within the high-Q region the modal linewidth is approximately 0.8 nm, limited by a combination of the reflectivity of the nitride DBR and scattering from residual morphological roughness presently under investigation. Figure 6-15 shows the emission spectrum from a device under photopumping at an incident average pump power of approximately 40 mW, exceeding the lasing threshold. The spectral width of the emission at 383.2 nm (<0.1 nm) was unresolved by our equipment. Above threshold, an intense low divergence beam of circular cross section was observed visually in the laboratory with fluorescent screens. A portion of the beam is shown in the photo as inset of Figure 6-16, where a screen was placed along the beam of circular cross section, to scatter light into a blue enhanced digital camera. An angular divergence (full)width of 7.4 degrees was measured, in very good agreement with the expected divergence dictated by the device aperture, as defined by the pump spot size.

Figure 6-16 shows input/output power characteristics of a particular device where the above-referred spectral coincidences are nearly optimal. The lasing threshold occurs at a rather low average pump power of 30 mW, while average output powers up to 3 mW were measured. However, finite thickness variation across the wafer led to spectral shifts of the cavity modes (relative to InGaN MQW gain spectrum) so that significant increases in threshold were encountered for devices fabricated from near the edge of the wafer (up to 100 mW beyond). It was possible to 'lose' the lasing altogether. When accounting for the optical excitation volume, the fractional absorption of the pump, and using an electron-hole recombination time of approximately 0.5 nsec, the threshold in Figure 6-16 corresponds roughly to a carrier density of approximately $10^{19}cm^{-3}$. Such a density is within the range of typical injection conditions employed in the best edge emitting blue and violet (In,Ga)N MQW diode lasers. It is encouraging, given the relatively shallow QWs (ΔE_G~160 meV) employed in these structures (low indium concentration). Still, absolute efficiency of the VCSELs was difficult to establish at this point, given the uncertainty in the relevant parameters (fractional pump absorption and possible carrier overflow in the QWs), factors that also make the estimate of the threshold carrier density only a rough guide.

A Vertical Cavity Violet Light Emitting Diode Incorporating an AlGaN Distributed Bragg Mirror and a Tunnel Junction

This section describes how a useful vertical cavity LED can be fabricated by incorporating an *in situ* grown AlGaN/GaN DBR below the active pn-junction InGaN MQW medium, with the cavity completed by a dielectric DBR. Another important problem of lateral hole current spreading, which is a major challenge in nitride vertical cavity structures, has been resolved by the use of an (Esaki) tunnel junction, composed of a thin, heavily doped p^{++}/n^{++} bilayer. Such a tunnel junction has been recently realized and demonstrated in an InGaN QW LED.[61]

Figure 6-17 shows the schematic diagram of the overall vertical cavity emitter. The nitride heterostructure was grown by organometallic vapor phase epitaxy (OMVPE) on (0001) sapphire substrate. The DBR grown using multiple AlN interlayers was employed in the fabrication of the resonant cavity LED. The wafers were *ex situ* tested at this point for their surface morphology and flatness by using optical interferometric profilometry and AFM techniques. Those growths that yielded a root-mean-square average roughness no worse than 4 nm over an area of 1x1mm^2 were deemed suitable for continuation of the epitaxy.

The active pn-junction region was grown directly atop the GaN/(Al,GaN) DBR, composed typically of 7 $In_{0.08}Ga_{0.92}N$ quantum wells (L_w=40 Å) with GaN barriers (L_B=60 Å), and surrounded by approximately 1000A thick $Al_{0.07}Ga_{0.93}N$ current blocking/carrier confinement layers. As a prerequisite for the vertical cavity device, we attempted to maximize the spectral overlap between the (narrow) high reflectivity region of the AlGaN DBR with that of the photoluminescence emission of the InGaN QWs, by conducting systematic separate growth studies of the both the DBR and the QWs. Finite layer thickness and compositional variations across the wafer (of In and Al in the active region and the DBR, respectively) reduced somewhat the total available area of the 2” wafers in terms of this requirement for spectral overlap. Such an overlap is, of course, critical for the possible vertical cavity lasers.

An intracavity lateral current spreading layer was incorporated atop the p-GaN layer by using recently developed tunnel junctions in the GaN system. For a vertical cavity device, such a current spreading layer is mandatory, given the low p-conductivity of GaN. In case of a tunnel junction, one takes advantage of the nearly 100 times higher n-type conductivity of GaN. (Note that indium-tin-oxide has been used previously in resonant cavity LED structures which feature all-dielectric DBRs; during the present study, ITO layers were also incorporated as hole current spreading structures to fabricate useful and functional devices). The tunnel junction was grown atop the 1000Å thick p-

GaN layer as a p^{++}/n^{++} InGaN/GaN bilayer with the thicknesses of the layers approximately 150Å and 300Å, respectively. The doping levels were approximately $1x10^{20}$ cm^{-3} Mg and $6x10^{19}$ cm^{-3} Si for the junction. (InGaN was employed as the p^{++} layer to obtain the required high acceptor and hole concentration). A 2000Å thick n-GaN cap layer completed the structure. These studies showed that lateral current spreading was more than adequate for the lateral device sizes employed here.

At this stage of the growth, the wafers were again tested by an optical interferometric profilometer for their surface quality and morphology, especially in terms of acceptable roughness. The vertical cavity was completed by capping the structure with a multilayer l/4 stack of SiO_2/HfO_2 (R>0.995), deposited by reactive ion beam sputtering. The broad reflection bandwidth (~80nm) of the dielectric DBR was tailored to overlap the near bandedge (In,Ga)N emission. The top dielectric DBR was patterned so that the device had an effective optical aperture varying from 10 to 30 μm. Standard lithographic and dry etching techniques were used to provide the electrical contacts, in form of a Ti/Al/Ti/Au annular ring to the top n-GaN cap layer and a deep etched contact area for the bottom n-GaN. The deep etch step defined the diameter of the mesa in Figure 6-17 in the range of 20 to 50 μm.

Figure 6-18 shows the current density vs. voltage of a typical device, at two levels of continuous injection at room temperature. In the low injection regime, characteristic of a LED (~100 A/cm^2), the presence of the tunnel junction typically added up to 1 V to the forward "turn-on" characteristics of the device, when compared with simpler LED devices without the TJ. At higher injection levels, (~1 kA/cm^2), evidence of additional series resistance was seen, assigned in part to the presence of the tunnel junction.

Nonetheless, the lateral current spreading was clearly accomplished so that the far field light emission from the devices was uniform in its average intensity across the emitting aperture, as illustrated in the photograph in the inset of Figure 6-19. However, when examining the emission under high spatial resolution (~1 μm) some evidence points to a tendency towards "filamental" vertical conduction, reflective perhaps of the influence of local compositional or doping inhomogeneities within the TJ. Specifically, the emission from the devices has been frequently observed to consist of a random distribution of micrometer sized 'bright spots' whose origin is appears to be due to locally enhanced injection current density. While these issues are under further investigation, many microscopic details of these new tunnel junctions remain undeciphered at this point, including the impact of the M-dopant "turn-off delay" in OMVPE growth.

Figure 6-19 shows the output spectrum of a typical device at operating current density of approximately 0.2 kA/cm^2. The emission was observed in the direction normal to the planar device, with apertures and imaging optics restricting the angular view to approximately 10 degrees. While the optical resonator is rather thick (>10 λ), only two vertical cavity modes are seen, demonstrating the restrictive spectral bandwidth of the AlGaN DBR. The dominant mode at λ=413 nm, which coincides with the high reflectivity region of the DBR and the peak of the QW PL emission, has a spectral linewidth of approximately 0.6 nm. This value is comparable to the linewidths previously measured in the best structures that were designed for optically pumped VCSEL operation. However, fabrication related challenges did result in frequent appearance of additional "ghost modes" due to secondary vertical cavities within the finished devices, especially in the smaller size regime (10 μm optical aperture, 20 μm mesa diameter).

Although the devices are not optimized at this writing for best vertical cavity performance, clear evidence of forward beam collimation in the output was seen. Likewise, the overall emission efficiency was excellent so that the directional forward emission typically exceeded that obtained from a conventional violet LED device without the vertical cavity.

In conclusion, a new type of vertical cavity violet emitter, designed and fabricated from a nitride heterostructure which features an as-grown, "stress-engineered" GaN/AlGaN DBR mirror as well as a p^{++}/n^{++} GaN-based tunnel junction has been demonstrated. These developments add to the building blocks that, together with advanced process techniques, can lead to a number of novel short wavelength light emitters, including an internally-pumped vertical cavity laser diode.

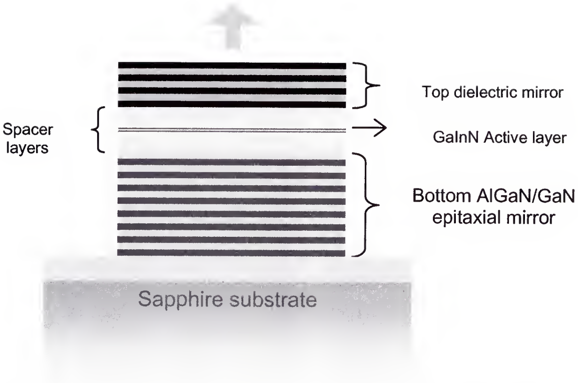

Figure 6 - 1 Schematic of VCSEL, illustrating the three main components of the device.

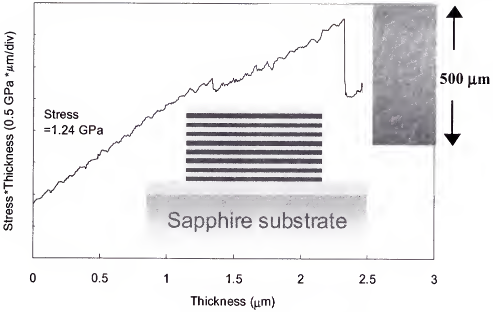

Figure 6 - 2 ***In situ*** **stress*thickness vs. thickness of a 30-pair $Al_{0.20}Ga_{0.80}N$/GaN DBR grown directly atop a 1-μm thick GaN template. The inset is a Nomarski micrograph showing the density of cracks on the surface of the multilayer structure.**

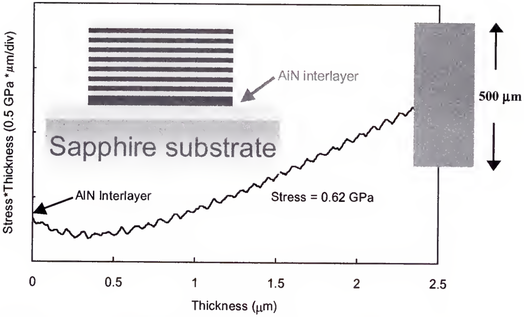

Figure 6 - 3 *In situ* stress*thickness vs. thickness of a 30-pair AlGaN/GaN DBR with an AlN interlayer inserted between the multilayer structure and the 1-µm GaN template. The inset is a Nomarski micrograph demonstrating that the surface of the wafer is crack-free.

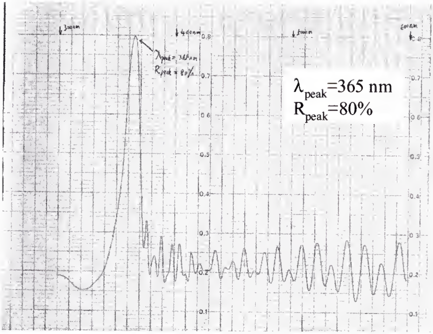

Figure 6 - 4 Reflectivity spectrum measured from the 30-pair $Al_{0.20}Ga_{0.80}N$/GaN DBR described in Figure 6-3.

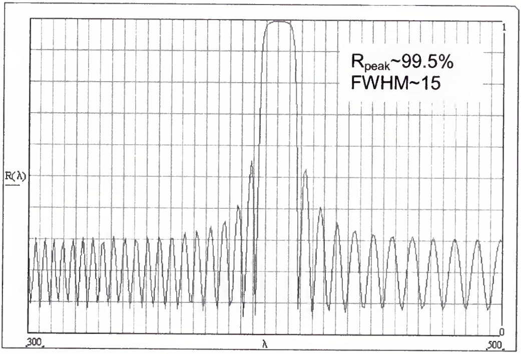

Figure 6 - 5 Computer simulation of reflectivity spectrum from 60 pairs of $Al_{0.20}Ga_{0.80}N/GaN$.

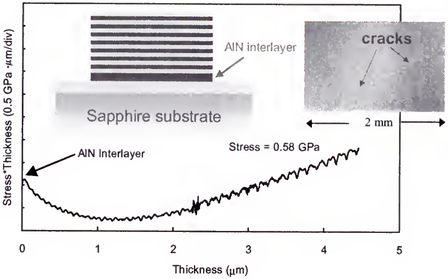

Figure 6 - 6 ***In situ*** **stress*thickness vs. thickness of a 60-pair AlGaN/GaN DBR using an AlN interlayer deposited at 1050°C.**

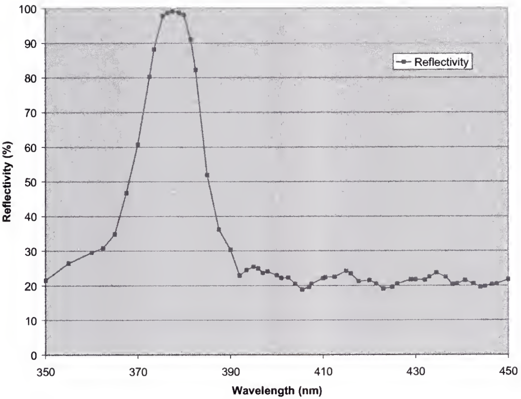

Figure 6 - 7 Reflectivity spectrum from the single interlayer DBR demonstrated in Figure 6-6.

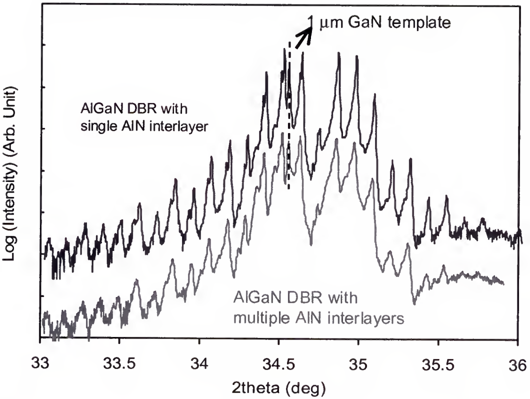

Figure 6 - 8 (0002) 2θ–ω high-resolution x-ray diffraction scan of the 60-pair AlGaN/GaN DBR using a single AlN interlayer (top trace) and the 60-pair AlGaN/GaN DBR using multiple interlayers (bottom trace). Satellite peaks are observed out to the 13th order, demonstrating high periodicity in the structure.

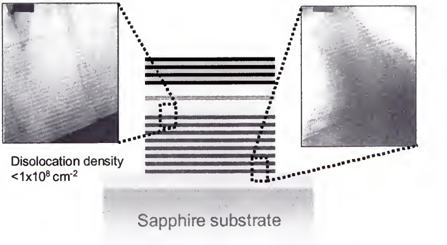

TEM prepared by G. Chu (Lucent Tech.)

Figure 6 - 9 Cross-section TEM micrographs taken using the (0002) reflection near the bottom and near the top of the single interlayer DBR structure. Microscopy was performed by Dr. S.N.G. Chu of Lucent Technologies, Inc.

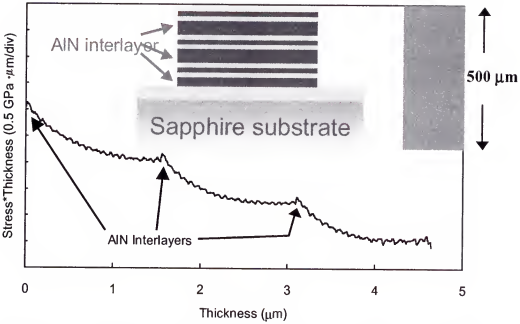

Figure 6 - 10 *In situ* stress*thickness of 60-pair AlGaN/GaN DBR using multiple HT-AlN interlayers for stress control. The entire 5-μm structure remains in compression. The inset is a Nomarski micrograph of the surface of the wafer demonstrating a crack-free device component.

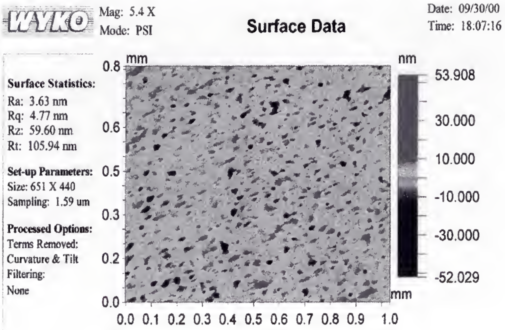

Mag: 5.4 X
Mode: PSI

Date: 09/30/00
Time: 18:07:16

Surface Statistics:
Ra: 3.63 nm
Rq: 4.77 nm
Rz: 59.60 nm
Rt: 105.94 nm

Set-up Parameters:
Size: 651 X 440
Sampling: 1.59 um

Processed Options:
Terms Removed:
Curvature & Tilt
Filtering:
None

Figure 6 - 11 Optical interferogram profilometry of the surface of the as-grown 60-pair AlGaN/GaN DBR employing multiple AlN interlayers. The surface roughness over the 1mm^2 area is approximately 4.5 nm.

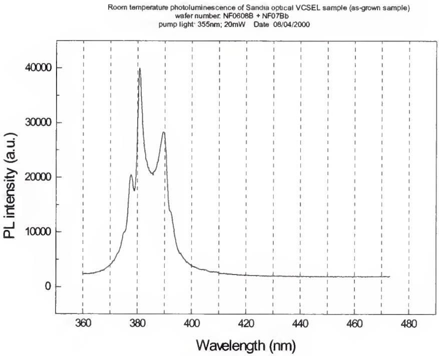

Figure 6 - 12 Photoluminescence spectrum from the as-grown InGaN/GaN MQW and passive region of the microcavity.

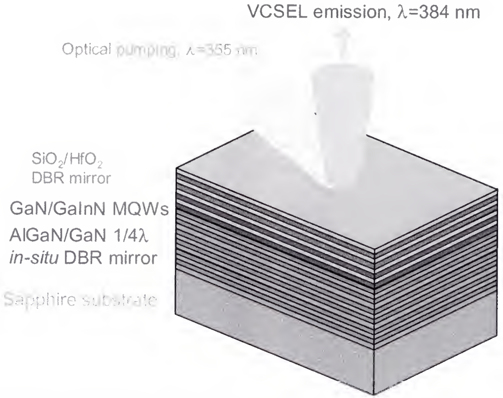
VCSEL emission, λ=384 nm
Optical pumping, λ=355 nm
SiO_2/HfO_2 DBR mirror
GaN/GaInN MQWs
AlGaN/GaN 1/4λ *in-situ* DBR mirror
Sapphire substrate

Figure 6 - 13 Stack structure of the completed device, including the top dielectric mirrors, and geometry of the optical characterization of the VCSEL.

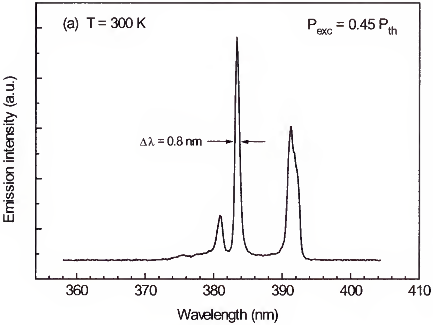

Figure 6 - 14 Spontaneous emission spectrum at excitation level of 45% relative to the threshold of the completed device.

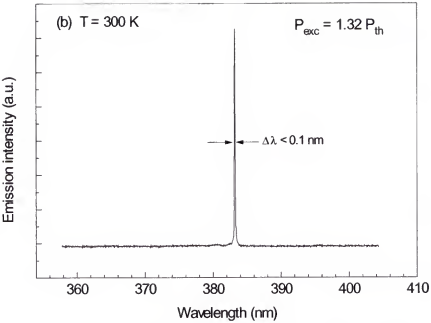

Figure 6 - 15 Optical spectrum of the VCSEL emission when photopumped at 132% relative to threshold. The linewidth of emission is below the resolution of the equipment.

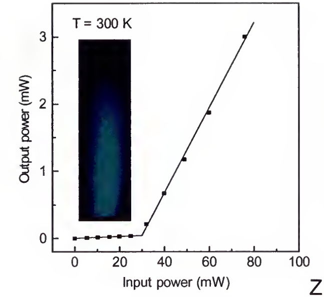

Rep. Rate=76 MHz
Pulse Duration=0.1 nsec
Duty cycle ~0.1%
Spot diameter=20μm
Angular divergence=7.4°

Zhou et al., Electron. Lett.

Figure 6 - 16 Average input vs. output power of a VCSEL device. The inset shows the beam (far field) profile captured on a screen.

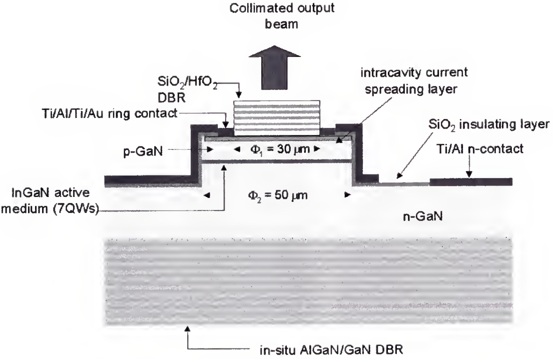

Figure 6 - 17 Schematic of the vertical cavity violet emitter, featuring a combination of *in situ* grown AlGaN/GaN and *ex situ*-grown dielectric DBR reflectors. A p^{++}/n^{++} InGaN/GaN tunnel junction-based intracavity current spreading layer is also indicated.

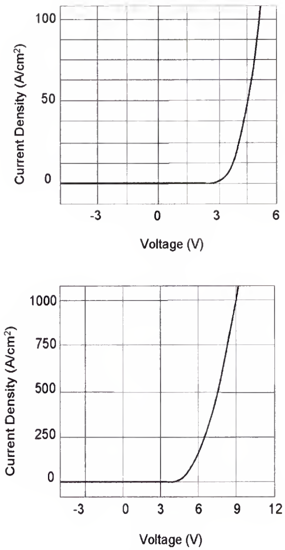

Figure 6 - 18 Current density vs. voltage characteristics of a device with a 20 μm diameter mesa defining the vertical current path. Low and high injection under room temperature continuous conditions are shown in the upper and lower panels, respectively.

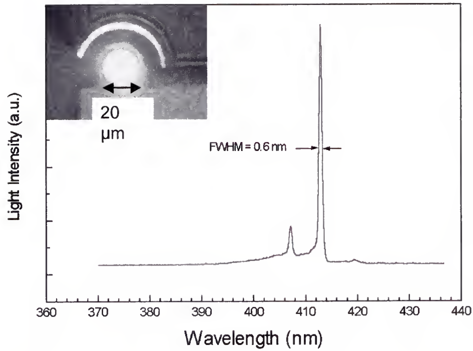

Figure 6 - 19 Emission spectrum of a device at J=0.2 kA/cm^2. The presence of only two modes is due to the narrow spectral bandwidth of the AlGaN DBR reflector. The inset shows the plan view photograph of the device, with emission filling an effective aperture of approximately 20 μm.

CHAPTER 7
SUMMARY AND FUTURE WORK

High quality AlGaN/GaN heterostructures are desired for the advancement of optoelectronic and electronic devices that will pave the way for important technological applications such as high efficiency lighting, chemical sensing, and high power, high frequency electronics. The tensile mismatch between AlN and GaN causes mechanical failure of the structure due to fracture. This work has explored the modification of AlGaN/GaN interface through the use of thin interlayers of (Al,Ga)N deposited under different growth conditions to learn how to control the strain and eliminate cracking in thick, high aluminum nitride mole fraction films. The major finding is that one defect, namely cracking, is in effect traded for another defect—edge dislocations. The edge dislocations are speculated to originate as threading segments from misfit dislocations generated at the interlayer/GaN substrate interface. The device engineer desiring to use (Al,Ga)N interlayers may be forced to choose between these tradeoffs. The structural and optical data suggest that it is best to choose interlayer conditions that keep the AlGaN overlayer in a state of tensile stress during growth that is below the critical stress-thickness (energy) for fracture. These conditions are often either mid-range composition low-temperature ternary alloy interlayers or thin, high temperature AlN interlayers.

Some future directions of this aspect of the project include further exploration of the V/III ratio of the AlN interlayer. Favorable results were obtained for V/III = 660, which involved an interlayer with close to planar morphology. Further exploration and optimization of the interlayer thickness, V/III ratio, temperature, and composition with an eye toward developing a quantitative model that would predict which interlayer growth conditions would be best suited for a particular application. For instance, the HT AlN interlayers employed in the DBRs described in Chapter 6 were a satisfactory choice for this application, as the photonic properties were more adversely affected by cracking than by edge dislocations. (Furthermore, the interlayers were kept well away from the active region of the device.) Additional experiments need to be run to determine the effects of the interlayers (i.e., high edge dislocation concentrations) on the electrical properties of the AlGaN overlayers. This may be of concern for electronic devices. Certainly devices that require vertical transport of electrical carriers require consideration of the composition of the interlayer as AlN is normally insulating.

The growth mode and relaxation of thin layers of MOCVD deposited AlN on GaN has been studied. In contrast to AlGaN alloys of lower Al fractions (~<25%) that grow epitaxially via Frank-van der Merwe growth (layer by layer), the high strain state of AlN causes it to grow via a 2D à 3D transition (Stranski-Krastanov) that takes place during the first 1-7 monolayers. This relaxes the homogeneous, planar strain field conditions and allows resolved shear stresses on slip planes. Thus strain-relieving misfit dislocations may nucleate and glide to the interface. Strain in the AlN/GaN system may be relieved due to misfit dislocation formation, geometrical relaxation of islands, and by expanding the lattice via gallium incorporation. All of these strain-reducing effects compete against surface energy and adatom mobility, which is presumably affected by such growth parameters as substrate temperature, V/III ratio, and composition, to determine the morphological evolution. If the hypothesis that the threading dislocations found to be present in AlGaN overlayers originate from misfit segments located at the interlayer/GaN interface is correct, then the degree of strain relief of the interlayer accounted for through misfits is important. Based on what has been learned in this work, it would be better from a technological standpoint to tailor the strain evolution of the interlayer so that most of it is relieved via geometrical relaxation of islands, if possible, rather than by misfit formation. This statement is highly speculative, since at this point nothing is known about the physical processes that occur at the overlayer/interlayer interface.

From a materials physics perspective, to gain a much fuller picture of the strain state of the AlN, plan view TEM is required to confirm the misfit dislocation content predicted in Chapter 5. The calculations of strain relaxation due to geometrical considerations (aspect ratio) could be refined by taking a more rigorous approach and conducting finite element calculations of the island shape. The island shapes were approximated rather severely for the work presented herein. Further experiments to conclusively determine the cause of the change in morphology with V/III ratio are in order. This was speculated to arise due to aluminum adatom mobility—a hypothesis put forth by researchers at UCSB. The results presented herein suggest that strain is not the dominating factor controlling the morphological evolution at high V/III, but that it does dominate at lower V/IIIs. The successful model will take into account the competition between all of the factors described above.

Further understanding of the catastrophic relaxation process that occurs in AlGaN/GaN heterostructures is desirable. This is an interesting materials system from a fundamental science perspective in that few tensile-strained wurtzite systems are available for study. The appropriate model will take into account the misfit dislocation formation, multiplication, and kinetic propagation mechanisms.

LIST OF REFERENCES

---

[1] S. Nakamura and G. Fasol: *The Blue Laser Diode: GaN Based Light Emitters and Lasers* (Springer-Verlag, New York, 1997).

[2] M. C. Benjamin, C. Wang, R. F. Davis, and R. J. Nemanich, Appl. Phys. Lett., **64**, 1687 (1994).

[3] H. Angerer, O. Ambacher, M. Stutzman, T. Metzger, R. Hopler, E. Born, A. Bergmaier, and G. Dollinger, Mat. Res. Soc. Symp. Proc. **468**, 305 (1997).

[4] S. J. Hearne, J. Han, S. R. Lee, J. A. Floro, D. M. Follstaedt, E. Chason, and I. S. T. Tsong, Appl. Phys. Lett. **76**, 1534 (2000).

[5] J. W. Hutchinson and Z. Sou, *Advances in Applied Mechanics* (Academic, San Diego, 1992), Vol. 29, pp. 63-191.

[6] C. W. Wilmsen, H. Temkin, and L. A. Coldren, *Vertical Cavity Surface Emitting Lasers* (Cambridge University Press, Cambridge, 1999).

[7] D. Brunner, H. Angerer, E. Bustarret, F. Freudenberg, R. Hopler, R. Dimitrov, O. Ambacher, and M. Stutzman, J. Appl. Phys., **82** 5090 (1997).

[8] J. Han and M. H. Crawford, R. J. Shul, S. J. Hearne, E. Chason, J. J. Figiel, and M. Banas, MRS Internet J. Nitride Semicond. Res. **4S1, G7.7** (1999).

[9] I. Akasaki, K. Hiramatsu, and H. Amano, Memoirs of the Faculty of Engineering, Nagoya University, **43**, 147 (1991).

[10] H. Amano, N. Sawaki, I. Akasaki, and Y. Toyoda, Appl. Phys. Lett. **48**, 353 (1986).

[11] I. Akasaki, H. Amano, Y. Koide, K. Hiramatsu, and N. Sawaki, J. Cryst. Growth **98**, 209 (1989).

[12] H. Amano, I. Akasaki, K. Hiramatsu, and N. Koide, Thin Solid Films **163**, 415 (1988).

[13] H. Amano, M. Kito, K. Hiramatsu, and I. Akasaki, Jpn. J. Appl. Phys. **28**, L2112 (1989).

[14] H. Amano, T. Asahi, and I. Akasaki, Jpn. J. Appl. Phys. **29**, L205 (1990).

[15] S. Nakamura, Jpn. J. Appl. Phys. **30**, L1705 (1991).

[16] S. Nakamura, M. Senoh, and T. Mukai, Jpn. J. Appl. Phys. **30**, L1708 (1991).

---

[17] K. Ito, K. Hiramatsu, H. Amano, and I. Akasaki, J. Cryst. Growth **104**, 533 (1990).

[18] Y. Kato, S. Kitamura, K. Hiramatsu, and N. Sawaki, J. Cryst. Growth **144**, 133 (1994).

[19] H. Amano, M. Iwaya, T. Kashima, M. Katsuragawa, I. Akasaki, J. Han, S. Hearne, J. A. Floro, E. Chason, and J. Figiel, Jpn. J. Appl. Phys. **37**, L1540 (1998).

[20] M. Iwaya, S. Terao, N. Hayashi, T. Kashima, H. Amano, and I. Akasaki, Appl. Surf. Sci., **159-160**, 405 (2000).

[21] H. Amano, M. Iwaya, N. Hayashi, T. Kashima, M. Katsuragawa, T. Takeuchi, C. Wetzel and I. Akasaki, MRS Internet J. Nitride Semicond. Res. **4S1,** G10.1 (1999).

[22] C. Kisielowski in *Semiconductors and Semimetals, Vol. 37: Gallium Nitride II.* ed. by J. I. Pankove and T. D. Moustakas (Academic Press: San Diego) 1999.

[23] C. Taylor, D. Barlett, E. Chason, J. A. Floro, *Ind. Physicist* **4**, 25 (1998).

[24] J. Floro, E. Chason, S. Lee, R. Twesten, R. Hwang, L. Freund, *J. Elec. Mat.* **26**, 969 (1997).

[25] M. Doerner and W. Nix, *CRC Critical Reviews in Sol. State and Mat. Sci.* **14**, 224 (1988).

[26] J. W. Matthews and A. E. Blakeslee, *J. Cryst. Growth* **27**, 118 (1974).

[27] A. F. Wright, *J. Appl. Phys.* **82**, 2833 (1997).

[28] J. Han, *Materials Research Society Fall Meeting*, Boston, Massachusetts, December 1, 1999.

[29] J. E. Shackleford, *Introduction to Materials Science and Engineering,* 2nd edition, Macmillan Publishing Company, NewYork: 1988.

[30] K. Itoh, K. Hiramatsu, H. Amano, and I. Akasaki, J. Cryst. Growth **104**, 533 (1990).

[31] W. G. Perry, M. B. Bremser, T. Zheleva, K. J. Linthicum, and R. F. Davis, Thin Solid Films **324**, 107 (1998).

[32] O. Gfrörer, T. Schlüsener, V. Härle, F. Scholz, and A. Hangleiter, Mater. Res. Soc. Symp. Proc. **449**, 429 (1997).

[33] H. Amano, T. Takeuchi, S. Sota, H. Sakai, and I. Akasaki, Mater. Res. Soc. Symp. Proc. **449**, 1143 (1997).

---

[34] S. Einfeldt, V. Kirchner, H. Heinke, M. Dieβelberg, S. Figge, K. Vogeler, and D. Hommel, J. Appl. Phys., **89**, 1(2001).

[35] S. H. Christiansen, M. Albrecht, H. P. Strunk, C. T. Foxon, D. Korakakis, I. Grzegory, and S. Porowski, phys. stat. Sol. (a) **176**, 285 (1999).

[36] S. Porowski, MRS Internet J. Nitride Semicond. Res. **4S1**, G1.3 (1999).

[37] S. J. Hearne, E. Chason, J. Han, J. A. Floro, J. Figiel, J. Hunter, H. Amano, and I. S. T. Tsong, Appl. Phys. Lett. **74**, 356 (1999).

[38] H. Amano, M. Iwaya, T. Kashima, M. Katsuragawa, I. Akasaki, J. Han, S. Hearne, J. A. Floro, E. Chason, and J. Figiel, Jpn. J. Appl. Phys. **37**, L1540 (1998).

[39] S. Nakamura, Jpn. J. Appl. Phys. **30**, 1348 (1991).

[40] J. Han, K. E. Waldrip, S. R. Lee, J. J Figiel, S. J. Hearne, G. A. Petersen, and S. M. Myers, Appl. Phys. Lett. **78**, 67 (2001).

[41] H. Amano, M. Iwaya, N. Hayashi, T. Kashima, S. Nitta, C. Wetzel, and I. Akasaki, phys. stat. sol. (b), **216**, 683 (1999).

[42] W.-K. Chu, J. W. Mayer, and M. –A. Nicolet: *Backscattering Spectrometry* (Academic, New York, 1978).

[43] $\Delta c/c=2(C_{13}/C_{33})\Delta a/a$ for a wutrzite crystal under biaxial strain along (0001).

[44] A. Trampert, O. Brandt, and K. H. Ploog: *Gallium Nitride (GaN)I* (Academic, San Diego, 1998).

[45] G. Nomarski and A. R. Well, Bull. Soc. Franc. Miner. Cryst. **77**, 840 (1954).

[46] J. W. Hutchinson and Z. Sou, *Advances in Applied Mechanics* (Academic, San Diego, 1992) Vol. 29, pp. 63-191.

[47] X. J. Ning, F. R. Chien, P. Pirouz, J. W. Yang, and M. Asif Khan, J. Mat. Res. **11**, 580 (1996).

[48] S. W. King, E. P. Carlson, R. J. Therrien, J. A. Christman, R. J. Nemanich, and R. F. Davis, J. Appl. Phys **86** (1999) 5584.

[49] S. Keller, Y.-F. Wu, G. Parish, N. Ziang, J. J. Xu, B. P. Keller, S. P. DenBaars, and U. K. Mishra, "Gallium Nitride Based High Power Heterojunction Field Effect Transistors: Process Development and Present Status at UCSB." IEEE Transactions on Electron Devices, Vol. 48, No. 3, March 2001, p552-559.

---

[50] S. Keller, G. Parish, P. T. Fini, S. Heikman, C.-H. Chen, N. Zhang, S. P. DenBaars, and U. K. Mishra, "Metalorganic chemical vapor deposition of high mobility AlGaN/GaN heterostructures." J. Appl. Phys. **86** (1999) 5850.

[51] For a review, see C. W. Wilmsen, H. Temkin, and L. A. Coldren, Vertical-Cavity Surface-Emitting Lasers (Cambridge University Press, Cambridge, United Kingdom, 1999).

[52] T. Someya and Y. Arakawa, Appl. Phys. Lett. **73**, 3653 (1998).

[53] R. Langer, A. Barski, J. Simon, N. T. Pelekanos, O. Konovalov, R. Andre, and L. S. Dang, Appl. Phys. Lett. **74**, 3610 (1999).

[54] I. L. Krestnikov, W. V. Lundin, A. V. Sakharov, V. A. Semenov, A. S. Usikov, A. F. Tsatsul'nikov, Zh. I. Alferov, N. N. Ledentsov, A. Hoffmann, and D. Bimberg, Appl. Phys. Lett. **75**, 1192 (1999).

[55] H. M. Ng, T. D. Moustakas, and S. N. G. Chu, Appl. Phys. Lett. **76**, 2818 (2000).

[56] G. Bauer and W. Richter, Optical Characterization of Epitaxial Semiconductor Layers (Springer-Verlag, Berlin, 1996) p. 294.

[57] C. Taylor, D. Barlett, E. Chason, and J. A. Floro, Ind. Physicist **4**, 25 (1998).
[58] M. Benamara, Z. Liliental-Weber, J. H. Mazur, W. Swider, J. Washburn, M. Iwaya, I. Akasaki, and H. Amano, MRS Internet J. Nitride Semicond. Res. 5S1, W5.8 (2000).

[59] T. Someya, R. Werner, A. Forchel, M. Catalano, R. Cingolani, and Y. Arakawa, Science **285**, 1905-1906 (1999).

[60] Y.-K. Song, A. V. Nurmikko, and R.P. Schneider, C.P. Kuo, M.R. Krames, R.S. Kern, C. Carter-Coman, and F.A. Kish, Appl. Phys. Lett. **76**, 1662-1664 (2000).

[61] T. Takeuchi, G. Hasnain, M. Hueschen, C. Kocot, M. Blomqvist, Y-.L. Chang, D. Lefforge and R. Schneider, M.R. Krames, L.W. Cook, and S.A. Stockman, submitted for publication.

BIOGRAPHICAL SKETCH

Karen Waldrip was born on November 16, 1971, in Manassas, Virginia. She received her Bachelors of Science degrees in chemistry and physics from George Mason University in Fairfax, Virginia in 1994. She obtained her Master of Science degree from the University of Florida in May 2001. Her interests are primarily in optoelectronic semiconductor materials science and device engineering.

I certify that I have read this study and that in my opinion it conforms to acceptable standards of scholarly presentation and is fully adequate, in scope and quality, as a thesis for the degree of Doctor of Philosophy.

Cammy R Abern

Cammy R. Abernathy, Chairman
Professor of Materials Science and
Engineering

I certify that I have read this study and that in my opinion it conforms to acceptable standards of scholarly presentation and is fully adequate, in scope and quality, as a thesis for the degree of Doctor of Philosophy.

Stephen J. Pearton
Professor of Materials Science and
Engineering

I certify that I have read this study and that in my opinion it conforms to acceptable standards of scholarly presentation and is fully adequate, in scope and quality, as a thesis for the degree of Doctor of Philosophy.

David P. Norton
Professor of Materials Science and
Engineering

I certify that I have read this study and that in my opinion it conforms to acceptable standards of scholarly presentation and is fully adequate, in scope and quality, as a thesis for the degree of Doctor of Philosophy.

Rajiv Singh
Professor of Materials Science and
Engineering

I certify that I have read this study and that in my opinion it conforms to acceptable standards of scholarly presentation and is fully adequate, in scope and quality, as a thesis for the degree of Doctor of Philosophy.

Fan Ren
Professor of Electrical and Chemical
Engineering

This dissertation was submitted to the Graduate Faculty of the College of Engineering and to the Graduate School and was accepted as partial fulfillment of the requirements for the degree of Doctor of Philosophy.

December 2001

Pramod P. Khargonekar
Dean, College of Engineering

Winfred M. Phillips
Dean, Graduate School